March 2015

Structural Vulnerability Assessment of Bridge Piers in the Event of Barge Collision

David A. Ribbans
University of Massachusetts Amherst

STRUCTURAL VULNERABILITY ASSESSMENT OF BRIDGE PIERS IN THE EVENT OF BARGE COLLISION

A Thesis Presented

by

DAVID A. RIBBANS

Submitted to the Graduate School of the

University of Massachusetts Amherst in fulfillment

of the requirements for the

MASTER OF SCIENCE IN CIVIL ENGINEERING

February 2015

Civil and Environmental Engineering

STRUCTURAL VULNERABILITY ASSESSMENT OF BRIDGE PIERS IN THE EVENT OF BARGE COLLISION

A Thesis Presented

by

DAVID A. RIBBANS

Approved as to style and content by:

Behrouz Shafei, Chair

Alice Alipour, Member

Richard Palmer, Department Head
Civil and Environmental Engineering Department

ACKNOWLEDGEMENTS

I would like to thank my advisor, Dr. Behrouz Shafei, for his guidance and support in my journey through this research. His nonstop encouragement and dedication to my development and research was instrumental to accomplishing this degree. I would like to also thank the committee member for my research, Dr. Alice Alipour, for offering her comments and perspective on my work. I would also like to acknowledge the other faculty of the Civil and Environmental Engineering Department, whose mentorship and encouragement have made my experience at the University of Massachusetts a truly positive one.

I am grateful for my family that continually supports me and always encourages me to strive for my own greatness and happiness. Also, I would like to acknowledge my friends that have also supported me greatly and enriched my experience at the University.

Finally, I would like to thank Prime AE Group Inc. for allowing me the opportunity to use construction drawings for a case study in this thesis. It should be mentioned that the models or simulations were not either ordered or approved by Prime AE Group Inc.

ABSTRACT

STRUCTURAL VULNERABILITY ASSESSMENT OF BRIDGE PIERS IN THE EVENT OF BARGE COLLISION

February 2015

DAVID A. RIBBANS, B.S., UNIVERSITY OF VERMONT

M.S.C.E., UNIVERSITY OF MASSACHUSETTS AMHERST

Directed by: Behrouz Shafei

The inland waterway system in the United States is fundamental to the transportation system as a whole and the success of the nation's economy. Barge transportation in these waterways levitates congestion on the highway system and is beneficial when comparing barge transportation to other modes of freight transportation in measures of capacity, congestion, emissions, and safety. Unavoidably, the highway system intersects with the waterways, resulting in the risk of vessels collision into bridge structures. Particularly for barge impact, the literature is questioning the accuracy and oversimplification of the current design specifications.

The impact problem was investigated in this research using thee-dimensional finite-element analyses. To investigate the collision of a barge into a bridge pier, a range of material models are first investigated through simulating a drop-hammer impact onto a reinforced concrete beam. A detailed model of a jumbo hopper barge is then developed, with particular detail in the bow. The barge model is examined for its response to impact into rigid piers of different size and shape. RC piers, having different shape and

boundary conditions, are impacted by the barge model and assessed using selected metrics. The final part of the research examines the response of an existing bridge pier subject to an impact by a chemical transporter barge that frequently travels in the waterway.

TABLE OF CONTENTS

Page

LIST OF TABLES

LIST OF FIGURES

CHAPTER 1

INTRODUCTION AND MOTIVATION

Inland waterways greatly contribute to the success of the Unites States economy. There are about 12,000 miles of navigable waters used for transportation of commercial building block commodities. Figure 1.1 shows the routes of the navigable inland waterway system. Spanning through 38 states, the inland waterways act similar to highway systems for commodities such as coal, gasoline, other petroleum products, iron, steel, grain, and aggregates through the US heartland. This system of waterways in collaboration with the railroad system leads to the success of major Midwest cities such as Chicago and St. Louis. It is the hidden back bone to the US economy.

The 2013 ASCE report card documents that barge transit moves 566 million tons of freight annually, valued at more than $152 billion. The waterway system carries the equivalent of 51 million truck trips. The intricate system reduces congestion on the highway and rail systems and reduces the transportation times of bulk commodities, which in turns lowers the cost of the product for the consumer. As seen in Figure 1.2 the waterway system intersects some of the most congested highways in the Midwest.

In addition to the economic advantage of the ease of movement on waterways, there are economic, fuel, and safety benefits of utilizing such transportation means for commodities. Tow and barge offers the most cost effective means to transport goods. Modern towboats can transport a ton of freight 616 miles on one gallon of fuel, where its rail and truck counterpart can only transport a ton 478 and 150 miles on a single gallon of fuel, respectively. Barge has proved to have the lowest injury records among the three modes. For every one injury involving barge transportation there are 95.6 rail-related and

1609.6 truck-related injuries. Additionally, as should be expected there is a low barge-related fatality rate. It seems intuitive that the Department of Transportation has projected an increase in annual traffic on inland waterways over the next 25 years.

With the highly developed system of highways and roads in the United States, bridges must span over the inland waterway system and coastal waterways. Bridges must not only span the gap but also resist forces from a variety of origins, including gravity, wind, earthquake and other hazards to remain operational and safe. Typically these bridges are larger structures that act as main arteries vital for the local residents and the economy of a given area. The local and national economy and residents rely on the robustness of bridges to be operable even during/after extreme events. On navigable waterways this includes the risk of large vessel impact.

The original Sunshine Skyway Bridge in Tampa, FL, opened to public in 1954, was the longest pre-stressed concrete bridge in the world. It spanned a total of 4 miles with a steel structure at the mid-span. On May 9, 1980, pilot of the Summit Venture, John Lerro, sent out a mayday distress call to the U.S. coast guard. "Get emergency … all the emergency equipment out to the Skyway Bridge. Vessel has hit the Skyway Bridge. The Skyway Bridge is down! Get all the emergency equipment out to the Skyway Bridge. The Skyway Bridge is down. This is Mayday. Emergency situation. Stop the traffic on that Skyway Bridge!" Zero visibility, loss of radar, and high winds lead to the collision into the southbound span, dropping over 1200 ft. of the bridge into the bay (Figure 1.3). With it 35 people fell into the bay and all lost their lives. One individual in a truck landed on the ship, surviving the fall. This tragedy urged the American Association of State Highway and Transportation Officials (AASHTO) to develop the Guide Specifications

and Commentary for Vessel Collision Design of Highway Bridges as part of the AASHTO LRFD Bridge Design Specifications and Commentary in 1999.

The U.S. Coast Guard marine casualty database attributes 42% of bridge collisions with towboats and tugboats between 1992 and 2000. Second is freight barges at nearly 33%, or 828 collisions. Other commercial boats and vessels fell far below these numbers. Causes of the incidents are most commonly accidents in navigation and weather conditions. Shadowing in the days after the September 11 terrorist attacks, a towboat and barge hit and collapsed the Queen Isabella Causeway in Brownsville, TX (Figure 1.4). However, little action was taken to strengthen safety standards for barge operation. In September of 2001 another collision into a rail bridge led to 47 deaths. On May 26, 2002 on the Arkansas River in Oklahoma, the captain of a barge blacked out approaching the I-40 Bridge (Figure 1.5). The barge veered away out of the main channel and struck the unprotected bridge piers. The increase in waterway traffic is expected to increase the risk of impact occurring on bridge substructures.

At maximum a barge vessel can travel at a mere 6 to 7 mph. Such an impact is seemingly insignificant; however, a loaded barge can weigh 1500 tons. With such mass, an impact is a highly significant event with very high impact forces. Neglecting to assess the risk and design for the possibility of impact in the bridge supporting structures could lead to the ultimate failure of the structure, like the cases that have been observed in the past. Catastrophic failure of a bridge is a life safety concern as well as an economic one. Collision incidents can be significant financial and economic burdens. If such an event were to occur on an inland waterway, the transportation on both the roadway and

waterway would be halted and delayed. A delay on the waterway would quickly ripple delays to future passages as well as immediate ones.

AASHTO provisions for impact forces were based upon a reduced scale test and used a static load approach for design loads. In the recent years, questions have risen on the accuracy of formulas, impact damage, dynamic interactions, and impact forces, especially with multi-barge (flotilla) impacts. Due to the lack of knowledge in this particular topic, there have been studies conducted primarily at the University of Kentucky and the University of Florida, using dynamic analysis and modeling to estimate impact loads. The current research project carefully reviews the available findings and further the state of the knowledge on the vulnerability of bridges subject to vessel collision through detailed computational simulations.

Following, in Chapter 2, there will be a comprehensive discussion of the findings from past research impact studies. Research focused on the impacts form fluid driven debris was included as much of the same general principles in impact analysis research are present. The vessel impact research will follow based on several references that focus on dynamic analysis of an impact. Finite element analysis has also been employed with three dimensional models to analyze the problem. Herein, includes a discussion of the methods and procedures of how to calculate impact forces and risk of impact.

Chapter 3 is the first step taken in modeling the reinforced concrete pier. Here an overview of concrete constitutive models will be provided. LS-DYNA has been used as the solver for dynamic finite element analysis of a doubly reinforced concrete beam impacted by a drop hammer. The drop-hammer tests conducted by the other researchers in the past will be modeled to examine a number of material models. The beam impact

analysis has driven research to investigate the modeling of the response of RC beams. This section will also discuss various modeling assumptions needed to appropriately reflect realistic behavior of structures subject to impact. Sensitivity of results to a range of input parameters is also studied in this chapter.

Chapter 4 is an overview of the use, design, and specifications of barges used in the United States. A detailed model of the barge was developed in accordance to construction drawing available. In an impact between a barge and the concrete pier, the damage that occurs to a barge results in a loss of energy that would affect the concrete pier. This section will evaluate the barge model through several impact cases with rigid piers. Following, the barge model is taken to simulate collisions with piers of different geometries with various initial conditions. Several metrics will be used to evaluate the performance of each simulation. This chapter will also present a case-study structure. The mid-span piers of the Goldstar Memorial Bridge in Connecticut will be evaluated for an impact with a vessel that navigates in the under passing waterway.

The final chapter of this thesis, Chapter 5, concludes the work that has been completed. Remarks will discuss the main outcomes of the research that has been conducted and emphasize the importance of investigating the vessel collision in the design of highway bridges over navigable waterways.

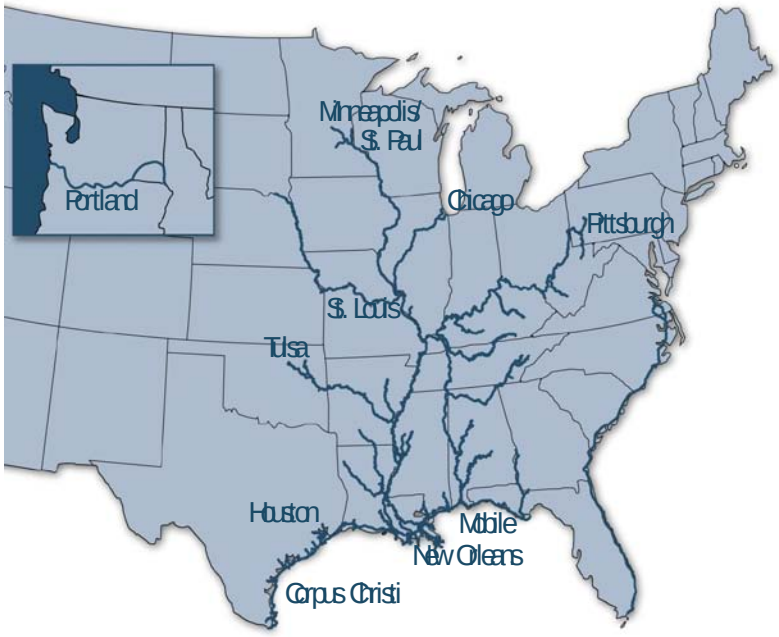

Figure 1.1 Inland waterway system in the United States

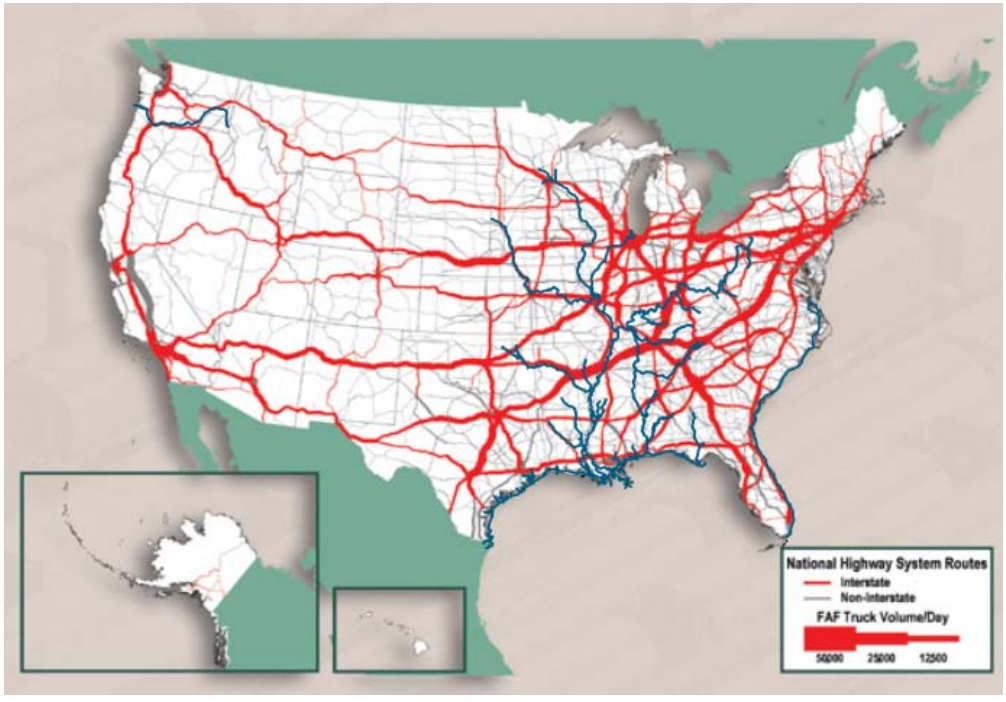

Figure 1.2 U.S. inland waterway system with truck volume on highways, showing the intersection of the waterway system with some of the most congested highways

Figure 1.3 Disaster of the collapse of the Sunrise Skyway Bridge
(http://www.panoramio.com/photo/53278080)

Figure 1.4 Queen Isabella Causeway collapse in Brownville, TX
(http://en.wikipedia.org/wiki/Queen_Isabella_Causeway)

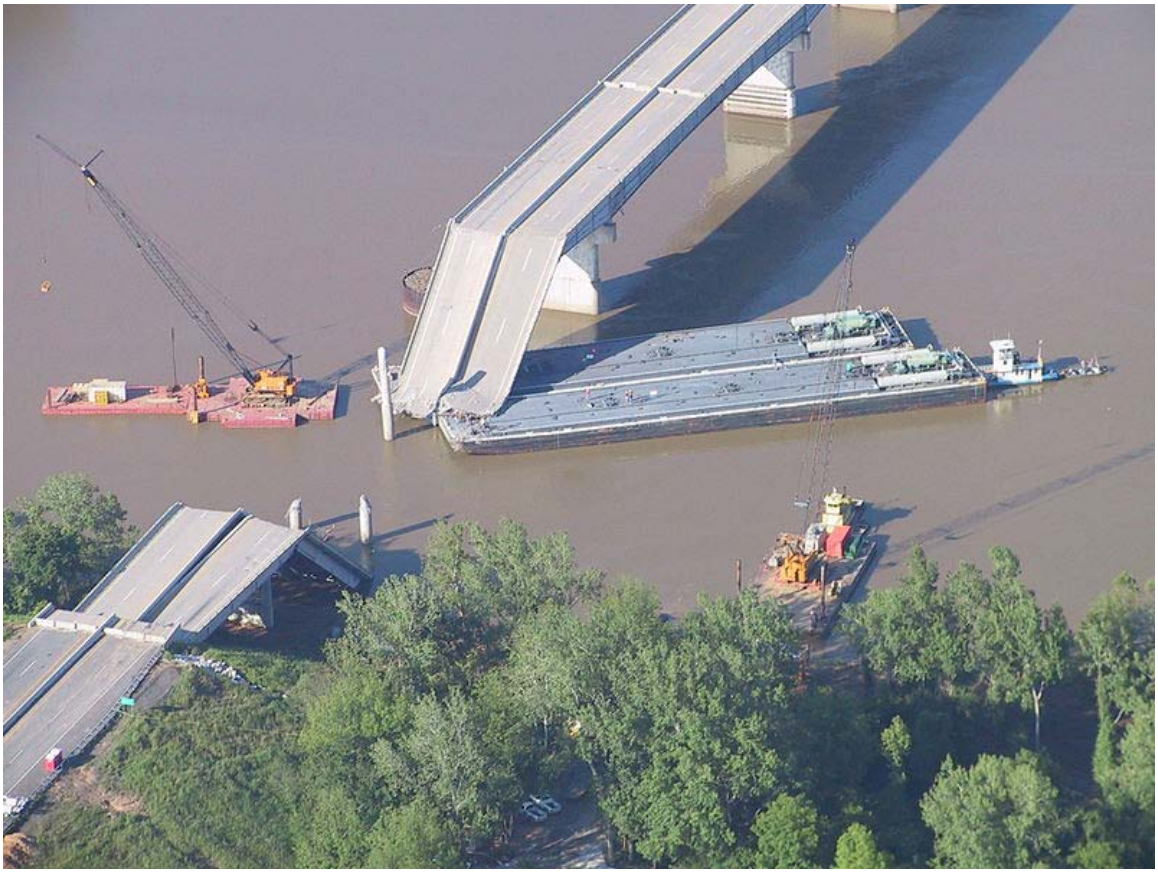

Figure 1.5 Barge collision with I-40 Bridge in Oklahoma
(http://en.wikipedia.org/wiki/I-40_bridge_disaster)

CHAPTER 2

REVIEW OF LITERATURE

Studies on structural impacts have been receiving a further amount of attention recently due to the availability of computational power in modern day computers. The complexity of the nature of materials, especially the structural behavior of concrete, during impact events has led to compelling interest in estimating the fundamental response characteristics. This chapter will examine some previous works on collision and impact and the AASHTO provisions for collision of vessels. Attention has been more focused on the impact behavior of collisions of low velocity and high mass, rather than high velocity impacts, such as projectiles and missiles.

2.1 Fluid Driven Debris Impact

There has been a significant push to understand the collision of waterborne objects, especially in tsunamis inundated areas. In the case of tsunamis, floods, hurricanes and storm surges, water is forced into areas with higher populations. Critical protective structures in these areas require special attention in design to resist loading from such events. In addition to the hydrostatic, buoyant, and hydrodynamic forces there exists the additional threat from debris. As water inundates a region, debris is picked up and can become a water borne projectile. Debris ranging from sand mixed in the water, logs, fuel storage tanks, shipping containers, vehicles, and other structures can litter the incoming water. In particular, this debris can pose a threat to tsunami safety structures. Studies on driftwood and storage containers have received particular interest.

The U.S. Army Corps of Engineers (Haehnel & Daly, 2002) prepared a technical report, which later published as an article in the Journal of Hydraulic Engineering (Haehnel & Daly, 2004), that investigates the maximum impact force of woody debris colliding into floodplain structures. The report investigates three different approaches to estimate the maximum impact loads based on debris velocity and mass. The three different approaches including contact stiffness, impulse momentum, and work energy are used as guides for design by three different organizations, the American Association of State Highway Transportation Officials (AASHTO), the Federal Emergency Management Agency (FEMA), and the National Association of Australian State Road Authorities, respectively, to estimate the peak impact load for design. Although, three separate approaches they were proven to be theoretically equivalent.

A single degree of freedom model was used to describe the impact of woody debris and a rigid structure, where the impact is a function of the velocity and mass of the debris and the effective stiffness of the collision. The three approaches can be derived from the SDOF system, thereby proving that the stopping time and stopping distance, used in the impulse momentum and work energy approaches respectively, are not independent parameters.

The greater focus of the article was conducting experimental impact data. Tests were conducted using reduced-scale logs in a flume and full-scale logs in a test basin. Data collected included maximum impact forces in both the flume tests and the basin tests, probability of orientation upon impact, compatibility between full-scale and reduced-scale impact forces, rigidity of the impacted structure, material on the face of the impacted structure, and the effects form eccentricity and obliqueness.

Following the experimental tests several conclusions were discussed. The data from the reduced-scale experiments resulted in the most scatter. When full sized logs impacted the structure at 90º the impact force was reduced due to flexure in the log. Appropriate effective contact stiffness was determined between a rigid structure and a log to be 2.4 MN/m, and was considered to be constant with rigid structures and log collisions. Stopping time and distance could only be constant for a particular range of debris mass and velocity. The material on the face of the structure had little effect on the maximum impact force. Geometry of the impact had a great influence on the maximum impact force, including eccentricity, obliqueness, and angle of impact.

A "practical method" to estimate the maximum superposed impact force due to simultaneous collisions of drift wood in tsunami inundation flow was presented by Matsutomi (2009). In addition, the probability of near simultaneous impacts was estimated. The research study utilizes inundation flow velocity, acceleration distance, collision force, duration of impact, time to peak impact force, drift wood collision probability, and results integration to develop equations for estimations. Findings present a series of equations to define a conceptual triangular pulse-like collision time history. The probability of a collision was a function of the variance, driftwood properties, and the distance from the structure.

A nonlinear impact analysis investigation of general purpose 20' and 40' standard shipping containers impacting reinforced columns was conducted using the finite element code LS-DYNA (Madurapperuma & Wijeyewickrema, 2013). Columns considered in the models were circular and square in cross-section. The results were used to compare to the two design guidelines that presently address the impact of waterborne massive

objects on structures, ASCE 7-10 and FEMA P646. Before conducting the numerical analysis of the storage container-column impacts, a validation of the concrete model was conducted by comparing the results from a drop weight impact test.

The containers models were developed in LS DYNA using accurate geometry that was given by the manufacturer specifications. Inelastic material models were used with appropriate stress strain relationships. The selected material models were accompanied with erosion models to capture the failure of steel and concrete. The reinforcing bars and concrete were not assumed to have perfect bonding rather slip between them was taken into account. Finally, the contact of the collision was prescribed to capture the dynamic behavior that occurs. An axial load was applied to the top of the column to represent the gravity load from the above structure.

Three longitudinal impacts, two transverse impacts, and a single corner impact were studied for each of the shipping containers on fixed square and circular columns. Several impact speeds, ranging from 2 m/s to 10 m/s, were tested for each column, container size, and impact configuration, and analyzed for damage. The results of the material failure were most significant when the corner of the barge is first to impact the column. Peak impact forces were compared with both guides, however the FEMA P646 guide resulted in forces that were too conservative. For any given impact speed the 40' container was found to have a higher impact force than the 20' container due to the increased mass and stiffness of the container. The square column impacts the container with a wider area, resulting in less impact force than the impact with a circular column.

The impact duration from ASCE 7-10 and the effective stiffness from FEMA P646 were calculated using the peak impact force and compared with the values given by

the guides. The results found that the duration depends on the configuration that the container impacts the column. This is not a consideration of the ASCE 7-10 guide. Alternatively, the FEMA P646 guide overestimates the effective contact stiffness determined in the study for the two sizes of container.

With the University of Hawaii, a collaborative project was conducted on debris impact forces, where full scale and reduced scale impacts were studied, theoretical models were developed, and code-type load specifications were obtained based on a mechanical-based, experimentally validated model (Riggs & et al, 2013). Full-scale in-air impacts of a wooden log and 20' shipping container were conducted at Lehigh University to create a baseline for the results. Oregon State University carried out 1:5 scale in-water testing in a large wave flume. Prototypical debris in the study consisted of the specified wooden log as in ASCE 7-10 and the standard shipping container due to the overwhelming occurrence of such containers in ports.

Analytical models of the impacts were proposed as a continuous rod and beam for the longitudinal and transvers impacts respectively, with an initial velocity impacting a spring. Impact force response was governed by the stress wave propagation through the debris. These basic models were assumed to be elastic and did not include the fluid; however one of the objectives was to study this in the experimental portion. Longitudinal impacts were modeled with the one-dimensional wave equation where the acoustic wave speed, modulus, area, length density, spring stiffness, and initial velocity define the response. Timoshenko beam theory was used to describe the behavior of the transverse impact considering shear wave speed, second moment of inertia, area, moduli, spring

stiffness, and density. From the model it was concluded that the longitudinal impact forces would be more critical, however the transverse impact is expected to last longer.

Lehigh University full-scale in-air tests were used to compare the predicted impact force and duration in the models. The prototypical debris was swung like a pendulum into impact a load cell. Varying velocities were tested, below a level that would cause significant damage until the final tests where large velocities causing significant inelastic damage could be observed. The in-air tests provided good results from the model equations for impact load and time duration, although the time duration was underestimated.

Reduced-scale shipping containers constructed of acrylic and aluminum were tested in a flume to investigate the effect of wave speed. Peak impact forces generally increase linearly with increased velocity. Little difference was seen in the time histories between the in air and in water tests. There is some small increase in the expected maximum force in the in-water test, but this was much lower than would be predicted from some added mass. It was concluded that the effect of the water was secondary to an in-air impact and can "likely be neglected for design" (Riggs et al., 2013).

After this publication, a more thorough article on the full-scale experimental tests conducted at Lehigh University was released (Piran Aghl et al., 2014). Because this study was a portion of the collaborative project previously described, the assumptions of the one-dimensional bar model were identical, with the formulas to predict peak impact force and impact duration. In addition to the wood utility pole and the shipping container, a 6.1 m steel tube was also investigated. The utility pole represents a common debris types, referred to as the log debris in the previous publication. Storage containers

are likely to disperse in a flood or tsunami. The steel tube was studied to understand the impact characteristics of structural members of the shipping container. There were a total of 194 tests with the three different debris materials. In each case several aspects were under investigation.

In the case of the wood pole, the contact area did not affect the peak impact force. For all elastic collisions, a linear relationship was identified between the peak impact force and the impact velocity. However, the contact time decreases with increasing impact velocity due to the increase in speed of sound through the wood pole. Strain gauges were used to measure this attribute. During an elastic impact the peak force demand decreased and the time duration of the impact noticeably increased. The contact stiffness was found to alter the demand of the peak impact force. Reducing the contact stiffness reduces the peak impact force and increases the time duration of the impact. This effect makes no change to the impulse of the collision.

The steel tube and shipping container were tested in both the elastic and inelastic regimes. As was expected, the impact force increases linearly with increased initial velocity, so long as the impact remains elastic. During an inelastic impact the duration of the impact increased up to 2.7 times that of the elastic. Failure was seen in fracture and buckling of structural members in the containers.

Overall the study conducted indicated that the model is an accurate representation of the peak impact force and reasonable for the time duration for elastic collisions. Time duration of the wood pole impact was not constant, like found in the steel container and tube tests, because of wood's rate sensitive properties. The dimension-independent impulse curves show that the model always results in conservative values for all impact

cases. ASCE 7-10 proposes a conservative dynamic response factor for a single corner impact, but this is not true for the unlikely case of all four corners impacting the structure at the same time.

2.2 Vessel Impact

AASHTO recommends the use of Design Method II for vessel collision design. Method II utilizes a probabilistic approach in selecting a design vessel for the collision analysis. As a result, it requires a significant amount of data. An investigation of the adoption of the new design method was undertaken for the State of Florida (Liu &Wang, 2001). Along the state's complicated inland waterways, there are 547 identified locations susceptible to vessel impact. Of these locations, 52 sites, mainly distributed in coastal areas, were selected to collect data for this study. To conduct the study in accordance with AASHTO, trip frequency was determined by the vessel size and loading condition. Barge width was used to classify the vessel size. Vessels were categorized into four groups, distinguished by barge widths, where the criterion approximates barge types (hopper, tank, and deck). Alternatively, ships were categorized by deadweight tonnage.

The distribution of trips in a single direction was analyzed for distribution based on length, width, and drift for a three-year period. Barge displacement, or weight, was estimated using the available length, width, and drift data, in accordance to AASHTO C5.3.2. Method II becomes increasingly difficult with the integration of barge trains. There are many variations in configurations of barges and tugs. In Florida, barge train mainly consists of one barge and one tug. However, the authors note that multiple barges to one tug are more common in the northwest. The data from South Florida showed that the majority of passages are from small ships, but these are not significant to the design

as an impact would produce forces less than the ultimate strength of the pier. The vessel traffic increase was also considered. Because the extent of the available data is relatively short and there was not waterborne traffic projection available, the Waterborne Commerce of the United States estimated the increase rate. Using this prediction, there were only a few past points that had high increase rates. The vessel transit velocity took great effort to collect, as many factors change the speed that a vessel travels at. Typical values were used and divided into detailed classes.

Finally, an illustrative bridge example was designed with 8 piers in accordance to Method II. This bridge was designed for one of the past points used in the study. This critical bridge had an acceptable risk of collapse of 0.0001 (or 0.01 in 100 years). This was uniformly portioned to the 8 bridge piers, as the assumption was that each pier and the superstructure represent the same replacement cost. After designing for the statistically sized barge and speed for the state of Florida, the annual frequency of collapse for the whole structure was calculated to be below the maximum acceptable level. Looking at larger barges there was only one or two sizes that cause concern to each pier. This can lead to a simplified risk design for the piers, only having to consider one or two categories instead of the original 7 or 9 in each direction. Traffic growth models only showed a small difference in the design, due to the assumptions of the model.

Research focusing on the crushing behavior of a barge through nonlinear pseudo-static collision simulations was conducted using the ADINA finite element code (Consolazio & Cowan, 2003). The simulations were compared to the AASHTO specified crush model. In the AASHTO code, different relationships are distinguished for pier

impact forces from ship vessels and barge vessels, due to the experimental and analytical bases for each vessel type. However, barge impacts have a higher rate of incidence because there are a greater number of waterways that allow vessels with shallow drafts (barges) as deep drafts (ships) cannot pass. The AASHTO method uses both risk assessment and empirical load prediction to develop a predicted impact load. After a design barge is identified, the kinetic energy of the barge is calculated. After which, a two-step empirical method is employed to define the equivalent static barge impact load. These two steps predict the deformation depth of the barge. The research utilizes this method to compare with the modeled results.

Consolazio & Cowan (2003) describe the setup, geometry, and methods of the model in great detail. The model was designed with an appropriate mesh resolution to capture local buckling, yielding, and internal contact in the crushed bow, while still conserving computation efficiency. To achieve this, three separate zones of the barge geometry were established, with appropriate degrees of mesh resolution to achieve model goals. The bow was the most detailed portion of the model, with shell elements built up to represent the channel sections, angle sections, and hull plates. Channel and angle sections made up internal trusses in the bow. For the second section beam elements were used to represent the internal trusses and shells for gusset plates and the hull plates. The remaining portion, and largest portion, of the barge was represented by very course 3D solid elements. Welds, the typical joining mechanism, were modeled with ADINA nonlinear rigid links. Contact-pair definitions were placed to allow the model surfaces to interact with each other. The steel, that comprises the barge, was modeled by a plastic multi-linear model with a defined stress strain relationship. No strain-rate effects were

included in this model, due to the pseudo-static condition of the model. Solid elements were modeled as an elastic model. The pier or impactor in this case, as it was the geometry that had the initial velocity assigned, was modeled using 3D solid elements with a nearly rigid linear elastic material model. Two geometric shapes were studied, square and circular, with varying widths and diameters, respectively, of 4, 6, and 8 ft. The impactor was assigned a constant velocity of 0.4 in/s.

The results from the three simulations with the circular pier showed very little influence from the increase in diameter of the pier. In each case, the force gradually and monotonically increased with crush depth. However, the square pier simulation did not follow this same trend. In these tests, the force quickly increases for small deformations. Following the peak, the stiffness of the barge lessens quickly. Additionally, no monotonic behavior could be recognized in the square pier results. Referring to the internal structure of the bow, this behavior could be anticipated. When a square pier impacts the barge, several trusses colliding with the piers immediately resist the force, acting very stiff, until they buckle, yield, and soften. The impact force has a notable dependence on pier width, due to the increased stiffness with the additional trusses in the contact region. Simulations with the circular pier show a concentrated area that impacts the pier, and therefor only near trusses resist crushing, until they fail and trusses further away from the initial impact must resist the force.

A comparison is made between the 8 ft. circular impactor, 8 ft. square impactor, and the AASHTO crush model. This research showed that the pier geometry is very influential in the impact forces for a given crush depth. In the cases of large crushing, the simulations predicted forces that are significantly less than the AASHTO model. As

previously stated, square pier simulations show that impact forces does not increase monotonically with crush depth. This means that the maximum impact force is not necessarily correlated to the maximum crush depth, as is assumed in the AASHTO method.

Beginning in the early 2000s, Consolazio & Cowan (2002) initiated plans to perform an extensive full-scale test of the barge-bridge column, paralleled with the reconstruction of the St. George Island causeway. Because of the details of the redesign of the causeway, an unprecedented opportunity to conduct full-scale tests on two of the piers was made possible. A structural investigation of bridge and barge components was carried out, with a geotechnical investigation on the in situ soil conditions and response. This was one of the first full-scale experimental investigations of this kind. The most crucial goals of the structural investigation consists of a lengthy list, but in general, collected data can be used to assess the accuracy of the AASHTO barge impact provisions and for the development of new design provisions. The test data also permit validation of design software packages and future development of improved dynamic analyses procedures.

Due to extensive scope and complexity of the experimental program, three phases were created to better focus the efforts. Phase I was a feasibility study, where the effect on the bridge replacement project was addressed, a review of previous testing, and an initial numerical simulation was undertaken on the proposed conditions. Phase II addressed the logistics of the testing and the designing of instrumentation systems for the experimental tests. Numerical models, developed in Phase I, were further developed and instrumentation arrays were designed through theses simulations. The final phase, Phase

III, incorporated the development of testing devises, the full-scale testing, and processing and interpretation of tests data. Several reports publish the details of teach phase of the program (Consolazio et al., 2002, Consolazio et al., 2003, and Consolazio et al., 2006).

Nonlinear finite element analysis models were developed in the software packages LS-DYNA and FB-MultiPier for this testing program. Numerical simulations were used to plan the physical tests, analyzing optimal ranges of parameters for investigation, and to design the instrumentation needed in for physical testing. Numerical models were used after testing to develop an in-depth understanding of the recorded data. Models were developed to appropriately represent the piers, barge, and soil. Model development was discussed with detail throughout the reports.

Extensive data was collected form the tests, measuring loads, deformations, accelerations, displacements, and pressures. There were reported cases of impact loads that were overly conservative in the AASHTO specifications. Crushing of the bow leads to a plateau of the peak impact force. This plateau was found to be 100% conservative in AASHTO provisions. Barge crushing was more related to the internal stiffeners and the pier width rather than the width of the barge and the pier. Additional observations of the structural and geotechnical response, the soil resistance, and fluid forces on the piles were also discussed in Consolazio et al. (2006).

An alternative to finite element simulations to analyze the response of a single barge or barge flotilla colliding with a bridge pier was proposed (Yuan & Harik, 2008). Finite element simulations for this problem are expensive to develop and solve, restricting such work to research purposes. The 1D model uses the most influential factors, including pier geometry, barge/flotilla geometry, stiffness, and dynamic

interactions, involved in a flotilla-pier collision. Separation of barges was not considered, rather the flotilla remains as one unit throughout the collision.

Flotillas are built up using individual barges, tied together with steel cables. The model for the steel cables was represented by a bilinear relationship of the resisting force with respect to a stiffness coefficient. Numerical simulations were used in the development the model for the body of the barge. LS-DYNA was used to derive the stiffness of an individual barge. Similar to the relationship for the cables, a bilinear model is used to describe the stiffness of the barge body, based on the upper bound of the dynamic stiffness. A multi-linear formulation was developed to represent the stiffness of the bow. The upper bounds of the dynamic stiffness were developed for a series of different rectangular shaped pier widths. This was compared to the AASHTO prediction that assumes no relationship with the pier geometry. The force-deformation curve for the bow indicates elastic deformation, plastic deformation, plastic collapse, and unloading, all captured with the piecewise function.

Three nonlinear springs were used to represent the force displacement relationships between the barge impacting the pier, adjacent barges in a column, and adjacent barges in a row. This is vital in developing a MDOF with elasto-plastic behavior. The expressions depend on magnitude of the restoring force and whether displacements are increasing or decreasing relative to the mass (barge). For each case, there were independent loading, unloading, and reloading relationships defined. The dynamic response of the pier was also included in the model. The pier is idealized as a fully supported, cantilevered column with four degrees of freedom, with a mass at the

location of impact and at the top of the pier. Also on top of the pier is a transitional and rotational spring, all representing the superstructure.

The system was represented by a simple matrix formula used in structural dynamics. A FE simulation of a three barge flotilla was developed for validation of this 1D MDOF model, where very good agreement was concluded. Comparatively, the AASHTO and the Modjeski and Masters method overestimate the impact force. However, AASHTO, FE and this proposed method predict similar barge crush depths. Another example flotilla was studied with a total of 15 barges. The interaction between the barges in the flotilla resulted in higher energy dissipation and an average impact force that is less than the AASHTO predicted value. The individual barge displacement was monitored with energy dissipation. This showed the loosening of lashings in the flotilla. This method proved to be suitable for analyzing symmetrical collisions. Although not as representative as an FE simulation, this method correlates well and requires significantly less computational time.

The AASHTO Guide Specifications and Commentary on Vessel Collision Design of Highway employs a simple calculation procedure to determine an equivalent lateral static load for design purposes. The simplified equivalent static force in Method I neglects the dynamic behavior of the bridge and factors that affect the force magnitude. The simplification excludes factors, such as impact duration, pier geometry, barge-barge and barge-pier interactions, and structural characteristics of the bridge, that are necessary to represent the problem. However, to include these factors FE simulations are most often used. FE models for these problems are computationally expensive. As a result, Yuan & Harik (2010) focused on efforts to develop a set of simplified equivalent lateral

force equations that account for pier geometry and the interaction between barges/flotilla and bridge structure.

Both single and multi-barge impacts were addressed using LS-DYNA. The barge was assumed as a jumbo hopper barge, with a geometry obtained from a manufacturer. The models include strain hardening effects, however, material failure and crack propagation effects were not included. Over 100 models were analyzed to obtain the regression formulas to derive barge bow stiffness for single barge collisions. The models used varied parameters for pier geometry as well as barge mass and initial velocity.

Single column barge flotillas were analyzed as well. Flotillas with 1 to 5 barges in a column were studied. Typically, barges are connected using steel cables. A similar connection was assumed in the LS-DYNA. The initial/maximum impact force varies very little with increased number of barges. After the peak impact force, the force curves differ, and different impact durations are observed due to the interactions of the different number of barges. For small energies it was found that the impact force is not proportional to the number of barges in a flotilla, because the impact force is most dependent on the strength of the lead barge bow. The other barges after the lead resist the rebound of the lead barge. Other regression formulas were derived using previously conducted simulations, considering impacts with high energies and velocities less than 5 knots.

The pier geometry was evaluated against the peak impact force. This relationship was found to be more significant for the rectangular piers. AASHTO was found to underestimate the impact force for the majority of geometry configures of rectangular

piers. Whereas, circular pier impact forces are overestimated after the depth of damage is greater than 0.5 m.

The last parameter studied was the impact duration and a related coefficient called the coefficient of restitution. This coefficient indicated the elasticity of the collision. Another set of models were studied to develop regression formulas for the coefficient of restitution. Lastly, limitations for all formulas were listed for the results given in the study. Solutions for determining the equivalent impact force, depth of deformation, and time duration from the study were outlined for three different cases; single barge, single-column three-barge flotilla, and three-column by 5 row 15-barge flotilla. The results from the AASHTO method, the proposed equivalent lateral force method, and FE time history method were compared. Good agreement was observed for all cases between the proposed method and the average force from the FE method.

An investigation to develop a model of the impact problem with nonlinear elements was conducted to capture better response characteristics than in previous literature (Sha & Hao, 2012). In addition a parametric study was conducted to evaluate the effect of barge velocity and barge mass on impact forces. In this study, a jumbo hopper barge was used in the FE model, as it is the most common barge used in the U.S. Additionally, the geometry of the bridge pier was square in cross section. The barge model was built using the software package ANSYS. Bow trusses were modeled using beam elements and outer steel plates were modeled with shell elements. The hopper section was constructed with 3D solid elements. The material model selected for the hopper section was elastic as no deformation was expected in this portion, which saved computational time. A finer mesh was employed in the bow portion of the barge to

capture the behavior of the deformation appropriately. The truss and bow were carefully modeled to capture the actual stiffness of the barge.

The concrete pier was modeled using 3D solid elements for the concrete using a material that is noted to being widely used for modeling the dynamic behavior and damage of concrete. Included in the material model are strain rate effect, plasticity, and damage softening after failure. Through a sensitivity study, a 100 mm mesh size was selected that captured similar impact results to that of the previous work from Yuan (2005). The pier was also examined with different material assumptions: rigid, elastic, and nonlinear. The impact force and the depth of damage of the barge bow were examined to compare the results. Rigid and elastic piers were relatively close in approximating the impact force; however the nonlinear material can result in differences. Likewise, the depth of damage followed similar results as the impact results when comparing the three materials.

Variations on the barge velocity and mass were compared. Large impact energy results in plastic deformation and damage that can compromise the superstructure. The impact forces, time duration and depth of damage were also examined. The damage was noted as being approximately linearly increasing with the increase in velocity until dominating the plastic deformations and crushing the trusses. Damage was monitored in the pier and barge. Increases in mass resulted in greater plastic deformation which caused greater contact times. Peak impact forces were not greatly different with the increased mass for high impact velocities. However, the time duration decreased with less mass.

Using the results found in the study, empirical formulas were developed to predict the crush depth and the impact force. A simplified time history was proposed as well.

Acknowledging that the study only investigated a square pier and neglected influences from soil-structure interaction and the different pier configurations, an extension of this work soon followed (Sha & Hao, 2013). This study focused on circular-shaped piers with different pier configurations and dimensions. Soil-structure interaction and free phase vibration of the pier was also observed in this study. Scaled pendulum impact tests were conducted to predict the impact force of a barge-pier collision. The dimensions and properties of steel were scaled to form a 78 mm circular column with a height of 750 mm. Concrete masses were also cast at each end of the pier. The pier was secured to a stationary steel plate in a wooden box with a prescribed compacted sand layer. Additionally, water was added to a particular level, all to simulate the foundation conditions of a bridge pier. A pendulum hammer system was used to test the piers. A numerical simulation was also conducted on this modeled simulation.

The experimental model was used to calibrate and evaluate the numerical model developed in LS-DYNA. A convergence study was conducted to investigate an appropriate mesh size to use for the pier. The contact algorithm was used to control the contact behavior between the pier and the pendulum hammer. The initial velocity of the hammer was predicted by $\sqrt{2gh}$. The selected concrete material model is widely used to model the dynamic behavior of concrete. It includes strain rate effects, plasticity, and damage softening after failure, while only defining minimal inputs. Because erosion is not integrated into this material model it was separately added to the model, which will delete the failed elements. Dynamic increase factors were used to account for strain rate

effects in the steel and concrete. These were assigned through equations given by Fan et al. (2011) for concrete tensile strength, the Comité Euro-International du Béton (CEB) (1993) code for concrete compressive strength, and Malvar (1998b) for the reinforcing steel. There was good agreement between the numerical and experimental results; however there was some variation in the free vibration phase of the response. The authors note that the numerical simulation reliably predicts both the impact force and displacement in the experimental model under impact loads, and accurate response characteristics of the pier model with plastic deformation and damage could be observed in the numerical model.

After validation, various barge-pier simulations were conducted. Pier support condition, barge velocity, barge mass, pier diameter and mass supported by pier, pier height and barge impact location on the pier were parameters in the simulations. A jumbo hopper barge was modeled for this portion of the study. The material model used for the bow of the barge was so that the isotropic and kinematic hardening plasticity could be captured with strain-rate effects. In most previous studies, soil interaction has been neglected and the foundation is assumed to have a fixed support condition. This assumption was evaluated in the numerical model with soil springs on the nine foundation piles. The fixed condition predicted an almost identical impact force time history, and soil-foundation-pier interaction can be neglected. However, displacement requires detail modeling of foundation and soil to obtain accurate estimates.

Barge velocity was investigated using three typical barge velocities, 2.06 m/s, 3.09 m/s, and 4.11 m/s. Increased velocity resulted in greater peak impact forces as well as longer impact durations. A longer duration should be expected due to greater

deformation of the bow at increased velocities. The displacement increased with increased velocity, however, elastic behavior was observed, as should be expected. The barge mass had an indistinguishable difference in the peak impact force, when comparing masses that represent an empty, half loaded, and fully loaded barge (181 ton, 952 ton, and 1723 ton respectively). The impact duration was greatly influenced by the increased mass. The diameter of the pier had virtually no effect on the peak force, but did alter the displacement of the pier, due to its increased stiffness. Additionally, the height of the column and location of the impact had unnoticeable difference in the peak impact force. Differences were observed in the displacements of the piers.

Concluding the study, formula to develop a triangular pulse load was proposed. The results of the numerical model and the proposed formula were in good agreement. Also, circular and square piers were compared with AASHTO specifications in a figure that compared barge crush depth versus impact force. It was observed that in small impact force conditions, AASHTO tends to underestimate the impact force. When the barge experiences crushing greater than 0.5 m AASHTO over predicts the impact force. The figure shows that pier geometry greatly affects the impact force and the specifications may result in inaccurate impact forces.

Luperi & Pinto (2013) captured accurate results from the impact of flotillas using a 1D model generalization of the work from (Yuan & Harik, 2008). The work conducted assumed that adjacent barges cannot separate from the flotilla. Other research conducted by Consolazio et al. (2008), discussed in this paper, represents flotillas with a single degree of freedom, and therefore the influence of adjacent barges could not be

considered. The present study utilizes a multi-degree of freedom, 2D model and a scheme that allows for nonsymmetric or oblique collisions.

The barge and pier were modeled by groups of points to define the mesh geometry. Contact between the different portions of the model were detected and controlled by a contact algorithm. The algorithm detects when points form a barge mesh falls inside the contour of another, adjacent barge or pier. Lashings between adjacent barges were modeled by 1D elements that sustain only tensile forces and behave elastic perfectly plastic with a defined failure limit. The configurations of the lashings were adopted from the research of Arroyo & Ebeling (2005). Barge crushing was also addressed as it is influential in energy dissipation in the system and maximum impact force in the collision. To account for the crushing of the barge bow, an elastic perfectly plastic relationship was adopted form Consolazio (2008, 2010). The dynamic properties of the impacted structure are accounted for in two different ways. When the impacted structure is the bridge pier directly, the convolution of the load history until a particular time step and the impulse response function of the structure can be used. Whereas, if there is a protecting structure, a piecewise linear spring would be appropriate.

The model, validated by the findings of Yuan & Harik (2008), resulted in very good agreement in the time histories of the impact force and kinetic energy of the barge. The proposed model is used to analyze the influence of adjacent barge columns in a head-on, symmetric impact. Parameters studied include, lashing configuration, number of barge columns, number of barges along the length of the flotilla, friction coefficient between barges, initial velocity, and yield force of the barge bow. Flotillas consisting of 3, 4, 5, and 6 barge columns were considered in the study, resulting in 3600 cases. This

parametric study showed that a simplified model of adjacent barges could be represented by an equivalent mass definition. However, the impact force history can be more accurately estimated using existing methods and the equivalent mass definitions that were developed in this study. Oblique impacts were found to be more accurately represented by the proposed model than by previous 1D model. The 1D model was only able to represent the impact of the center barge column. The load history of the proposed model showed a greater peak value that accounts to the combined impact of both center and adjacent barge columns. The 1D model resulted in an unconservative estimation of energy absorbed by the impacted structure, which was captured by the 2D model.

2.3 AASHTO Guide Specifications

The AASHTO Guide is the controlling document for designing of highway bridges in the U.S. Some of the details have been summarized in the discussions of previous research on barge collisions. The AASHTO Specifications use the kinetic energy of a barge to determine an impact load that influences a bride pier. The kinetic energy of a vessel, in this case a barge, is determined by the following equation:

$$KE = \frac{C_H W (V)^2}{29.2} \qquad \text{Equation 2.1}$$

where,

KE = vessel collision energy (kip-ft)

C_H = hydrodynamic mass coefficient

W = vessel displacement tonnage (tonnes)

V = vessel impact speed (ft/s)

After the kinetic energy is determined, an empirical formula is used to determine a predicted crush depth of the barge bow.

$$a_B = \left[\left(1+\frac{KE}{5672}\right)^{1/2} - 1\right]\left(\frac{10.2}{R_B}\right) \qquad \text{Equation 2.2}$$

where, a_B is the barge bow damage depth, $R_B = B_B/35$ and B_B is the barge width in feet. This relationship was determined from the correlation proposed by Meier-Dörnberg (1983) between crush depth and impact deformation energy. R_B is effectively a barge size coefficient. Finally, an impact force is determined from the deformation of the bow:

$$\begin{aligned} P_B &= 4112(a_B) \quad \text{for } a_B < 0.34 \\ P_B &= 1349 + 110(a_B) \quad \text{for } a_B \geq 0.34 \end{aligned} \qquad \text{Equation 2.3}$$

where P_B is the static impact force in kips. The equation for the impact force is determined from a force-deformation curve developed from a single experimental research (Meier-Dörnberg, 1983). Although this research was a great advance for the development of impact design specifications for bridges, it has its shortfalls. Typical barges in the U.S. are structurally different than the European barge used for the referenced research. Additionally, the experimental results were from a reduced-scale model of a barge, which arguably introduces approximation due to sizing effects.

CHAPTER 3

DROP HAMMER − BEAM IMPACT TEST

This chapter discusses the development of three dimensional (3D) finite element (FE) models for the investigation of impact problems. The drop hammer test is used to evaluate several modeling assumptions and their effect on the results from the impact. The models were developed in the software package LS-DYNA (LSTC, 2013). LS-DYNA is an explicit FE program used for the 3D nonlinear transient analysis of structures. Similar results reported in the literature are used for comparison in the simulations of the beam impact study conducted in this chapter.

3.1 Beam Impact in Literature

An experimental study was conducted by Fujikake et al. (2009) to investigate the impact responses of reinforced concrete beams. In addition, analytical models were created to predict the maximum mid-span deflection and the maximum impact force. Twelve different cases were tested in the drop hammer experiment. The reinforced concrete beam, shown in Figure 3.1, has dimensions of 1700 mm in length, 250 mm in height, and 150 mm in width. The reinforcement in the beam consists of two top longitudinal reinforcing bars, two bottom longitudinal reinforcing bars, and stirrups. Three variations of top and bottom reinforcement within the specimens under investigation include D13, D16, and D22, with yield strengths of 397 MPa, 426 MPa, and 418 MPa, respectively. The beams, distinguished by the longitudinal reinforcement arrangements, are designated as S1616, S1322, and S2222. Where the ‘S’ represents ‘Series’ and the first two numbers are representative of the size of the reinforcement on

the compression side, and the last two numbers are the representative of the size of the reinforcement on the tension side of the beam. Stirrups were D10 bars, with a yield strength of 295 MPa, spaced 75 mm apart.

A 400 kg free falling drop hammer was used to apply the impact load to the top of the reinforced concrete beam. The drop hammer was dropped over the mid-span of the beam at four different heights: 0.15 m, 0.3 m, 0.6 m, and 1.2 m for S1616 beams, and 0.3 m, 0.6 m, 1.2 m and 2.4 m for S1322 and S2222 beams. The portion of the drop hammer that impacted the beam was hemispherical in shape with a radius of 90 mm. The beam was supported centered over 1400 mm to allow rotation, but prevent it from moving. The setup of the experiment can be seen in Figure 3.2. The hammer was instrumented with a dynamic load cell. To measure the contact force, a laser displacement sensor was used to measure the mid-span displacement of the beam.

Failure modes were observed in the twelve specimens. S1616 were noted as experiencing overall flexural failure from all drop heights, where the S1322 and S2222 beams only experienced overall flexural failure with drop heights of 0.3 m and 0.6 m. Also, these beams experienced local failure with heavily crushed concrete at drop heights of 1.2 m and 2.4 m.

The impact responses were observed where the impact force and displacement time-histories were compared. The general patterns of the impact load are "characterized by an initial pulse-like waveform with comparatively high amplitude followed by a blunt waveform with comparatively low amplitude." This is the expected behavior that should be observed by such loading cases. The peak of the pulse increased with increasing drop height, however the duration of this portion remained approximately 2.0 ms. The blunt

portion of the wave responded oppositely, where the peak is approximately the same, regardless of drop height, but the duration increases for greater drop heights. Mid-span deflection and impulse also increased with greater drop heights. It was also observed that the flexural rigidity of the beam appeared to affect the duration of the impact loading, the maximum deflection, and time of the maximum mid-span deflection. A nonlinear analysis was developed to determine the load-deflection relationship at the mid-span of a reinforced concrete beam. The development of this analysis involved the determination of moment-curvature relationship, which includes strain rate relationships for both concrete and steel rebar. Last, an analytical model was used to determine the maximum mid-span deflection. Where beams experienced only an overall flexural failure mode, the analytical model showed good results in comparison with the experimental results.

Based on the experimental tests conducted by Fujikake et al. (2009), a series of studies followed investigating the impact response of RC beams. These investigations conducted numerical simulations of the beam impact experiment with 3D nonlinear FE analysis. Numerical simulations in LS-DYNA, modeled from experimental tests (Fujikake et al., 2009), were conducted using an elasto-plastic damage cap (EPDC) model (Jiang et al., 2012). In material libraries, concrete models can be divided into three different categories of constitutive models based on the methods to calculate the plastic deformation. The EPDC model uses associated flow to calculate the plastic strain increment. The plastic volume strain increment is obtained from the incremental flow rule, where dilatancy under shear loading at low confining pressure is captured. The other two categories were also summarized, which include material models that will be used in future simulations in this thesis.

Jiang et al. (2003) modeled the RC beam with eight-node hexahedron elements and the drop hammer was modeled in two sections to develop its total mass inertia. Four-node tetrahedrons were used to build the drop hammer model. Reinforcing bars were modeled with truss elements, sharing nodes with concrete elements. Solid elements use one-point Gauss integration and viscous hourglass control during the simulations. To model the impact properly, eroding type surface to surface contact was assigned to the drop hammer and top surface of the beam. Friction coefficients were introduced to account for the frictional forces that occur at the interface. The beam was supported to only restrict vertical displacement.

The EPDC model used for the concrete was proposed by Schwer and Malvar (2005) and treats the plastic flow and damage accumulation as separate processes. A total of 22 parameters define the material. The parameters are associated with the unconfined compressive strength of the concrete. In this case, the unconfined compressive strength at the 28^{th} day was assumed to be 30 MPa. A series of drop heights were investigated. To decrease computational time, initial velocities were assigned to the drop hammer set 1 mm away from the top of the beam. Considerable accuracy was obtained for the impact force curves during all drop heights. Post-peak vibrations were also captured considerably well, although some discrepancies were reported. Variations in the relative velocities attribute to this behavior. Pre-peak mid-span deflections were successfully modeled. The post-peak behavior calculates larger residual displacements. Increased drop heights increases the duration of the post-peak impact forces and reduces the error in the impact force and mid-span deflection. Concrete damage was also observed in the models and compared to the experimental photographs. It was observed

that as the drop height increases, the cracks tend to navigate toward the center and the diagonal shear cracks are expected to begin to form.

Other parameters in the material model were investigated by simplifying model features. Influences of damage, cap surface, deviatoric plane stress, meridian plane shape, and meshing technique were all investigated as part of this study. It was found that the influence of the deviatoric plane shape was the only parameter that had no significant influence on the results. Additionally, reinforcement sharing nodes with concrete elements results in better results than the coupled run.

A similar experimental program conducted with the aid of Fujikake et al. (2009) investigated two variables, loading rates and shear reinforcement, in the beam (Adhikary, Li, & Fujikake, 2012). The three amounts of shear reinforcement were 0% (RC3_S0), 0.12% (RC3_S12), and 0.56 % (RC3_S56). For each of the shear reinforcement specimens, there are four loading rates under investigation. The four loading rates through displacement control are static (4×10^{-4} m/s), low (4×10^{-2} m/s), medium (0.4 m/s), and high (2 m/s).

Other than the shear reinforcement, the beams followed the geometry of the test conducted in (Fujikake et al., 2009). The longitudinal reinforcement was constant for all specimens, including two top and bottom D22 rebars. Shear reinforcement selected was D6 stirrups. The concrete had a compressive strength of 40 MPa. The beams were well instrumented with a load cell, strain gauges, and accelerometers to capture the load, accelerations, displacements, and rebar strains. Deflection was captured with a laser-type variable displacement transducer.

Evident increases in carrying capacities were observed as loading rates increase in all three shear reinforcement amounts. For the RC3_S0 beam, the capacity increased by 20%, 52%, and 66%, as the loading rate increased progressively from low to high. During the static and low loading rate cases, the peak load increased quickly and dropped due to brittle shear failure. Despite this, there was a significant amount of residual strength, with more strength present in the low loading rate than the static case. The medium and high loading rates results indicated that the crack development was occurring and post-peak vibrations were observed. The RC3_S12 beam recorded strength increases of 20%, 33%, and 45% due to increased loading rates. The slope of the post-peak portion of the load-mid-span deflection curve increased for high loading rates for the shear-critical beams. Similarly, the RC3_S56 beam load resistance increased by 7%, 11%, and 15%, for increased loading rates, compared to the static case. The results from this beam indicated a specific yield point for static, low and medium loading rates, but no specific point could be indicative in the high loading condition. Other observations on the dynamic increase factors, stiffness, energy absorption, strain in the longitudinal rebar, and crack patterns were also discussed.

LS-DYNA was used to develop FE models of the RC beams using a relatively coarse mesh size of 25 mm. Approximately 7300 elements created the geometry of the beam impactor and supports. Reinforcement node locations were shared with concrete elements, forming a perfect bond. The supports were designed as two rigid cylinders that were allowed to rotate about their longitudinal axis without translation. Concrete was modeled with Material 072, which develops parameters based off the negative value of the unconfined compressive strength, density, and unit conversion factors. Material 024

was employed for the steel reinforcement and a rigid material was used for the loading plate and supports. The experimental setup is shown in Figure 3.3.

Models were analyzed under displacement controlled simulations. Reasonably good agreement with published results was reported. The numerical model was used in a parametric study. The study analyzed the influence of longitudinal reinforcement ratio, transverse reinforcement ratio, and shear span to effective depth. Longitudinal reinforcement ratio had no effect on the dynamic increase factor (DIF) without the presence of transverse reinforcement. DIF increased with decreasing longitudinal reinforcement, as loading progressively increases. Transverse reinforcement influenced the DIF for the high loading rate. Confinement resisted catastrophic failure of the beam under loading rates greater than the static state.

Following the goals of this study, a similar investigation was conducted on the response of reinforced concrete deep beams (Adhikary et al., 2013). The experimental setup was essentially identical to the investigation that the authors had previously reported in (Adhikary et al., 2012). Two variables, the amount of shear reinforcement and the loading rate, were investigated in twenty-four, paired deep beam specimens. All the beams had a shear-span to effective-depth ratio of 1.9, with the same amount of longitudinal reinforcement, consisting of two D22 mm rebars for the top and the bottom reinforcement. The percentages of shear reinforcement under investigation are 0%, 0.42%, and 0.84%provieded in beams RC1.9_S0, RC1.9_S42, and RC1.9_S84, respectively. Loading rates were similar to that of the previous study, where static, low, medium, and high rates are under investigation. Experiments were conducted through displacement controlled test. Specimens were instrumented with load cells, strain

gauges, and accelerometers, in addition to a laser-type variable displacement transducer to monitor the mid-span displacement. Increases in the shear resistance are obvious in the load versus mid-span deflection curves. The capacity of the RC1.9_S0 beam increased by 50%, 100%, and 150%, for low, medium, and high loading rates, respectively. In addition, beams for all increased loading rates had more residual strength than the static case. Increases in peak load for the RC1.9_S42 were found to be 11%, 33%, and 53%, for increasing loading rates, with sufficient residual strength compared to the previous one. Under all loading rates, the RC1.9_S84 specimens behaved ductile due to the high level of transverse reinforcement, indicative by the load versus mid-span deflection curves. Dynamic increase factors of the maximum resistance are more significant for beams without shear reinforcement.

In addition to load versus mid-span deflection curves commentary on the strain at the mid-span in longitudinal rebar, crack profiles were recorded. Shear reinforcement increased the stiffness of the deep beam under higher loading rates from that recorded during static state. Minor increases in stiffness were observed in beams with shear reinforcement for low, medium, and high loading rates. Peak strain rates were one order of magnitude higher for each level of loading rate.

Numerical simulations were developed using LS-DYNA. Assumptions for the model were identical to the previous setup from (Adhikary et al., 2013). The model was validated by load-deflection curves and crack profiles, displayed in the model through effective plastic strain fringes. Finally a parametric study addressed the effects of the longitudinal reinforcement ratio, transverse reinforcement ratio, and the shear-span to effective-depth ratio.

3.2 Modeling Assumptions

In the current study, the models of the RC beam with spherical drop hammer were examined. Simple shape meshing was utilized to develop the geometry of both the RC beam and the drop hammer. Model geometry selected followed the experiment of the S1616 beam of (Fujikake, et al., 2009). An example image of the geometry can be seen in Figure 3.4. The distribution of shear reinforcement and the spacing can be better visualized with the transparent solid elements in the figure.

3.2.1 Boundary Conditions

The reinforced concrete beam has dimensions of 1700 mm × 250 mm × 150 mm with a 90 mm radius spherical drop hammer. The beam and drop hammer were modeled with eight-node solid elements. The beam is simply supported 150 mm from each end, restricting axial displacement only in the Z coordinate direction. The drop hammer contained 12096 elements whereas three different mesh sizes were developed for the beam to investigate the effect of the size of elements on the impact response. The mesh sizes are designated as coarse, medium, and fine, consisting of 5336, 51000, and 110160 elements, respectively. Reinforcing steel was modeled with beam elements, sharing nodes with the nodes of the concrete elements. This assumes that there is a perfect bond between concrete and rebar. Although this assumption is not entirely true to the real world, it is appropriate to assume a perfect bond in the models.

In the original experiment, the drop hammer was released from rest at four different heights: 0.15 m, 0.3 m, 0.6 m, and 1.2 m. In order to limit the computational time of the models, the drop hammer sphere is located 1 mm above the top of the beam

with an initial velocity. The velocity of the drop hammer was calculated through the following kinematic equation for an object in free fall:

$$v_f = \sqrt{v_i^2 + 2gd} \qquad \text{Equation 3.1}$$

where v_f and v_i are the final and initial velocity respectively, g is the gravitational acceleration, and d is the distance of free fall. The final velocity in the given equation is assigned as the initial velocity to the model.

Gravity loading on the bodies in the model can be executed at any stage of modeling prior to solving the model. When loading/stressing is added to the model prior to the beginning of the model solution, it is known as dynamic relaxation. This is necessary when prestressing exists, such as a column supporting a large mass. Before time 0 of the model, dynamic relaxation phase is executed to find equilibrium within the model from the defined loads. Dynamic relaxation was not considered in the drop hammer simulations because the mass of the beam spanning over the supports is not large enough where dynamic relaxation would significantly change the results. However, the effects due to gravity can alter the results and should be investigated in this study. For this purpose, a universal loading is applied to individual parts in the model in the negative Z direction.

Contact interaction that occurs between the drop hammer and beam must be assigned. Without a contact definition the program will not know how to handle overlapping and intersecting nodes and elements. Two contact algorithms were considered to control the interaction in the drop hammer and the beam. Both algorithms require the user to define a slave and master segment or surface. The eroding contact is recommended for use when solid elements are subject to erosion. The contact algorithm

allows the contact surface to be updated as the exterior elements erode. In the contact algorithm, coefficients for dynamic and static friction should be defined. Literature suggests that an appropriate value for both coefficients is 0.3.

The selection of an appropriate time step is essential in monitoring the correct amount of detail from the model. Small time steps can result in high levels of fluctuations, not particularly representative of the behavior of the model. Large time steps can lose important details of behaviors. Time steps selected in the current study were 10 times smaller than the time step of the plotted data. Figure 3.5 shows that there is very little difference in the data collected over different ranges of time steps.

3.2.2 Constitutive Material Models

Because the concrete is a composite material and has a complex response to impact loading, several constitutive material models have been developed and are available in the LS-DYNA material library. The different material models have various advantages and disadvantages when modeling the behavior of concrete. An appropriate material model should be selected based upon the user's background knowledge and experience with concrete.

3.2.2.1 CSCM Concrete

Although originally developed for the analysis of roadside safety structures for the National Cooperative Highway Research Program, this concrete model can be used for other dynamic analyses. There are two available options in LS-DYNA for input data of this material model. The first option requires that all the material parameters are supplied by the user, including moduli, strengths, hardening, softening, and rate effects parameters. The second option, however, presents a more convenient option where the

default parameters are provided by the code through three inputs: unconfined compressive strength, aggregate size, and the units. Default parameters are given values fitted for unconfined compressive strengths between 20 and 58 MPa.

This concrete material model is an elasto-plastic damage model that incorporates rate effects. There are six general categories of formulations that comprise this concrete model: the elastic update, plastic update, yield surface definition, damage, rate effects, and kinematic hardening. The model includes four isotropic constitutive formulations: a three stress invariant shear surface with translation for pre-peak hardening, an expanding and contracting hardening cap, damage based softening with erosion, and rate effects. A general overview of key aspects of this model will be discussed.

As concrete is generally assumed to be an isotropic material, Hooke's Law has been used for the elastic portion of the stress-strain relationship. The bulk modulus, K, and shear modulus, G, are used to define this relationship. These constants, determined through the following empirical formulations, are a function of the user input value of the unconfined compressive strength, f'_c. The compressive strength of concrete is derived by the CEB code formula:

$$E = E_C \left(\frac{f'_c}{10} \right)^{1/3} \qquad \text{Equation 3.2}$$

where E is the modulus of elasticity and E_C is the modulus of elasticity when $f'_c = 10\ MPa\ \ (E_c = 18.275\ \ MPa)$. The bulk and shear moduli are derived through the following relationships with Poisson's ratio, υ, taken to be 0.15 for the default parameters.

$$K = \frac{E}{3(1-2\upsilon)}$$ Equation 3.3

$$G = \frac{E}{2(1+\upsilon)}$$ Equation 3.4

After the elastic behavior, yielding and failure can occur depending on the state of stress. At each time step, if the stress lies beyond the yield surface, the material behaves elasto-plastic, with the possibility of damage, hardening and strain rate effects. However, if the stress lies on or within the surface, the behavior remains elastic and no plasticity occurs. Plasticity is modeled in a more complex manner to capture dilation after yielding. A three-dimensional yield surface is used to determine the yield stresses. This material model is extended to calculate the yield surface by three stress invariants: the first invariant of the stress tensor, second invariant of the deviatoric stress tensor, and the third invariant of the deviatoric stress tensor, respectively. The surface utilizes a multiplicative formulation, combining the shear surface with the hardening compaction surface smoothly and continuously, hence the materials name continuous surface cap model (CSCM).

Concrete softens under tensile and relatively low compressive loading conditions. This softening effect is captured through the damage formulation. Without this formulation the material would be unrealistic behaving perfectly plastic in tension and low confinement. The damage is formulated through both strain softening and modulus reduction. Strain softening is identified as a decrease due to progressive straining beyond peak strength. Modulus reduction is the decrease in slope for loading/unloading curves that are observed in cyclic loading.

Rate effects implemented in the model increase in strength with higher strain rates. Rate effects are applied to the plasticity surface, damage surface and the fracture energy. The yield surface rate effects applied to the model are based on an extension of the Duvaut-Lions formulation purposed by (Simo, et al., 1988) that requires one user-defined fluidity coefficient, η.

$$\sigma_{ij}^{vp} = (1-\gamma)\sigma_{ij}^{T} + \gamma\sigma_{ij}^{P} \quad \gamma = \frac{\Delta t/\eta}{1+\Delta t/\eta} \qquad \text{Equation 3.5}$$

where σ_{ij}^{vp}, σ_{ij}^{T}, and σ_{ij}^{P} are the viscoplastic, viscid, and inviscid stress tensors, respectively. The CSCM concrete model can better fit high strain rate data through the use of two parameters, η_0 and η, instead of the one viscoplastic formulation parameter through this simple form:

$$\eta = \frac{\eta_0}{\dot{\varepsilon}^{\eta}} \qquad \text{Equation 3.6}$$

This material model has 37 different parameters that must be defined. Nineteen of them are fit data so that the model can accurately simulate real world behavior. However, as previously mentioned, this material model has been made easier to use with default parameters based on three inputs. The simplified approach for parameter formulation has been utilized in this study.

3.2.2.2 KC Concrete

This concrete model, also commonly known as Release III of the K&C concrete material model or KCC model, was developed to improve the results of high fidelity physics-based finite element analyses of reinforced concrete walls subjected to blast loading. Key behaviors of concrete and other cementitious materials, including concrete

strength, confinement effects, compression hardening and softening, shear dilatancy, tensile fracture and softening, biaxial response, and rate effects, must be captured by the model to be suitable in high dynamic loading conditions.

The KCC material model uses three fixed deviatoric stress invariant surfaces to compute the plastic response. This formulation for the plasticity uses a measure of the material damage to develop a new yield surface at each time step. The newly predicted yield surface is based on the current state of the material at a given material point. The three surfaces used, known as the yield, limit, and residual surface, remain fixed through user input and the value of computed damage parameter previously described. Rate effects have to be incorporated into the model through user-defined tabular data of dynamic increase factors. The yield surface expands and contracts proportionally to the dynamic increase factor. Further discussion of strain rate effects in material models will continue later in this chapter.

To fully define the KCC model, there are close to 50 parameters that need to be defined, plus an equation of state (EOS) that defines the pressure-volumetric strain relationship of the cementitious material. There are two options for the obtaining data for this model. Several experimental tests and extensive simulations can be used to define the individual parameters for this model. Alternatively, in the latest release of the KCC model all the required parameters can be automatically generated from fitting based on the strength of concrete. The fit is based on a suite of concrete data form a specific concrete type. Automated fitted data is computed by scaling the default parameters by the unconfined compressive strength of the concrete. It should be emphasized that the default parameters and scaled values are based off a specific type of concrete and

therefore a good fit might not result from generic scaling. There have been some issues noted with the generic data. First, the compression softening does not reflect for element size, where the fit was established for a 4 inch element height. Furthermore, how aggregate size regularizes the fit data has proven to be problematic for small elements. Other discrepancies were also noted in various tests.

3.2.2.3 Reinforcing Steel and Drop Hammer Materials

The drop hammer part was modeled the same throughout all simulations. The drop hammer consists of 12096 solid elements. The drop hammer was assigned a rigid material model. With the modulus of elasticity assigned a value like that of steel, in this case 200 GPa was used. The density was assigned such that the mass of the sphere would be equal to 400 kg. Reinforcing steel are beam elements and assigned dimensions to match the (Fujikake et al., 2009). The piecewise material model was used for the reinforcing steel and the corresponding stress train curves are idealized as bilinear curves.

3.2.3 Strain Rate Effects

Reinforced concrete is often used as the main structural material for protective structures subject to blast and impact loading. These types of loading can produce very high strain rates, up to 1000 s^{-1}. The response of concrete and reinforcing steel due to these high strain rates is often subject to investigation. High strain rates can produce a significant increase in the strengths of both materials. The dynamic increase factor (DIF) is a ratio of the dynamic versus static value (i.e., strength or yield stress). DIFs are often reported in a curve as a function of strain rate. Knowledge and understanding of DIF for both materials is significantly important for the design and analysis of reinforced concrete structures exposed to explosive or impact forces. Such curves have been published in

several manuals by the Tri-Services, the Defense Special Weapons Agency, the Air Force, and the Department of Energy. However the data for these curves are limited. Following will be a review on strain rate relationships for both concrete and reinforcing steel.

3.2.3.1 Concrete Strain Rate Effects

Dynamic increase factors can exceed 2 for compressive strain rates and may reach up to 6 for tensile strain rates. As strain rates increase so does the strength of the concrete. This phenomenon can be seen in Figure 3.6, where a collection of data has been compiled in (Bischoff & Perry, 1991). The Comité Euro-International du Béton (CEB) proposes a comprehensive relationship using two bilinear formulations for the DIF-strain rate curves, one for the compression regime and the other for the tensile regime. The CEB formulas indicate a change in slope located at 30 s^{-1} (on log-log axis).

The CEB model for concrete in compression is well known to appropriately replicate the actual behavior of concrete and is accepted by most researchers. The dynamic increase factor for the compressive strength of concrete is given by:

$$CDIF = \frac{f_c}{f_{cs}} = \left(\frac{\dot{\varepsilon}}{\dot{\varepsilon}_s}\right)^{1.026\alpha_s} \qquad for\ \dot{\varepsilon} \le 30\ s^{-1}$$
$$CDIF = \frac{f_c}{f_{cs}} = \gamma_s\left(\frac{\dot{\varepsilon}}{\dot{\varepsilon}_s}\right)^{1/3} \qquad for\ \dot{\varepsilon} > 30\ s^{-1} \qquad \text{Equation 3.7}$$

where f_c is the dynamic compressive strength at strain rate $\dot{\varepsilon}$, f_{cs} is the static compressive strength at strain rate $\dot{\varepsilon}_s$, $\log \gamma_s = 6.156\alpha_s - 2$, $\alpha_s = 1/(5 + 9 f_{cs}/f_{co})$, and $f_{co} = 10$ MPa. The relationship is given for strain rates, $\dot{\varepsilon}$, ranging from 30 $\times 10^{-6}$ to 300 s^{-1}, where the static strain rate, $\dot{\varepsilon}_s$, is determined to be 30 $\times 10^{-6}$ s^{-1}.

In tension, the CEB defines the DIF similarly as:

$$TDIF = \frac{f_t}{f_{cs}} = \left(\frac{\dot{\varepsilon}}{\dot{\varepsilon}_s}\right)^{1.016\delta} \qquad for\ \dot{\varepsilon} \le 30\ s^{-1}$$
$$TDIF = \frac{f_t}{f_{cs}} = \beta\left(\frac{\dot{\varepsilon}}{\dot{\varepsilon}_s}\right)^{1/3} \qquad for\ \dot{\varepsilon} > 30\ s^{-1}$$

Equation 3.8

where f_t is the dynamic compressive strength at strain rate $\dot{\varepsilon}$, f_{cs} is the static compressive strength at strain rate $\dot{\varepsilon}_s$, $\log \beta = 7.11\delta - 2.33$, $\delta = 1/(10 + 6\, f_{cs}/f_{co})$, and $f_{co} = 10$ MPa. The relationship is given for strain rates, $\dot{\varepsilon}$, ranging from 30×10^{-6} to 300 s^{-1}, where the static strain rate, $\dot{\varepsilon}_s$, is determined to be 30×10^{-6} s^{-1}.

This tensile DIF for concrete does not appear to fit findings from other researchers. The break in slopes has been reported to be too far to the left of data in comparison plots. Hence, a modified version of the CEB formulation was developed in (Malvar & Crawford, 1998). Due to this situation, the modified form will be adopted in this thesis for the dynamic increase factors of concrete. The formulation for DIF, including the compressive DIFs will be referred to as the CEB/Malvar formulation in this thesis.

The modified formula for tensile DIFs is similar to the bilinear function in log-log scale, however the change in the slope occurs at 1 s^{-1}, closer to where data showed a change in slope. The modified model defines DIF in tension as:

$$TDIF = \frac{f_t}{f_{cs}} = \left(\frac{\dot{\varepsilon}}{\dot{\varepsilon}_s}\right)^{\delta} \qquad for\ \dot{\varepsilon} \le 1\ s^{-1}$$
$$TDIF = \frac{f_t}{f_{cs}} = \beta\left(\frac{\dot{\varepsilon}}{\dot{\varepsilon}_s}\right)^{1/3} \qquad for\ \dot{\varepsilon} > 1\ s^{-1}$$

Equation 3.9

where f_t is the dynamic compressive strength at strain rate $\dot{\varepsilon}$, f_{cs} is the static compressive strength at strain rate $\dot{\varepsilon}_s$, $\log \beta = 6\delta - 2$, $\delta = 1/(1+8 f_{cs}/f_{co})$, and $f_{co} = 10$ MPa. The relationship is given for strain rates, $\dot{\varepsilon}$, ranging from 10^{-6} to 160 s^{-1}, where the static strain rate, $\dot{\varepsilon}_s$, is determined to be 10^{-6} s^{-1}. A plot of the CEB/Malvar DIF is shown in Figure 3.7.

3.2.3.2 Reinforcing Steel Strain Rate Effects

The American Society of Materials and Testing (ASTM) prescribes many static properties of reinforcing steel, often requiring minimum values to be met. Increase strengths up to 60% for strain rates up to 10 s^{-1} and 100% for higher strain rates have been observed under dynamic loading conditions. High strain rates result in the increase of the steel's yield and ultimate stress. However, relatively constant values of modulus of elasticity and ultimate strain were noted in the static and dynamic loading conditions.

The following DIF formulation was developed by (Malvar & Crawford, 1998), for both the yield and ultimate strength:

$$DIF = \left(\frac{\dot{\varepsilon}}{10^{-4}}\right)^{\alpha}$$

$$\text{For yeild stress}: \alpha = \alpha_y = 0.074 - 0.040\frac{f_y}{414} \qquad \text{Equation 3.10}$$

$$\text{For ultimate stress}: \alpha = \alpha_u = 0.019 - 0.009\frac{f_y}{414}$$

where f_y is the yield strength in MPa and $\dot{\varepsilon}$ is the strain rate in s^{-1}. This formulation is for yield strengths between 290 MPa and 710 MPa and strain rates ranging from 10^{-4} to 225 s^{-1}. A constant slope can be observed when the logarithm of the DIF is plotted on the vertical axis and logarithm of the strain rate on the horizontal axis.

According to (Murray, 2007), there is a simplified curve for modeling dynamic increase factors for rebar. No indication was found concerning the background or source of this curve, but the reference indicates this curve as an example of DIF for rebars. All the DIF curves have been plotted in Figure 3.8, from the Malvar formulation for 295 and 426MPa, as well as the curve given in the FHWA Manual (Murray, 2007).

3.2.4 Hourglass Effects

Hourglass modes are non-physical deformation modes that can be seen due to underintegrated elements. In particular, solid elements and shell elements with single integration points create these zero stress deformation modes. Examples of hourglass modes can be seen in Figure 3.9 for solids and shells. Hourglassing can be avoided by using fully integrated solids and shells or by using tetrahedrons and triangular elements, all of which either come at a cost or are less favorable. Fully integrated solids are computationally expensive and weaker in large deformation cases. Tetrahedrons and triangles can lead to element locking. These considerations commonly lead to the use of the more favorable one-point integration method for solids and shells with controls to minimize hourglassing. Hourglass controls work by applying internal forces to resist the development of hourglass modes.

There are many different options for the hourglass control type, however only the first few are of particular interest in this study. These can be categorized into two groups, viscous and stiffness forms of hourglass control. Viscous forms of hourglass control develop hourglass forces corresponding to nodal velocities that result in hourglass modes. The viscous forms are recommended for high velocity or strain rate situations. Alternatively, stiffness forms generate hourglass forces resulting from nodal

displacements contributing to hourglass modes. Problems with lower rates, such as crash simulations like those investigated in this research, should utilize the stiffness forms for hourglass control. Stiffness type control can result in artificially stiffer responses.

To control hourglass energy and minimize stiffening effect, appropriate hourglass coefficients should be chosen. LSTC (2013) recommends using reduced values for stiffness forms of hourglass control. In addition, they state the hourglass energy should be less than 10% of the total internal energy of the whole system and each part, as a general "rule of thumb." The listed methods for controlling and monitoring hourglass energy will be used to select an appropriate hourglass coefficient for each model. The selection of an appropriate hourglass coefficient will later be discussed in detail.

3.3 Results from Impact Simulations

A series of simulations using two different material models were conducted examining the impact response of the beam, including the impact force and deflection time histories. Developed numerical models were compared to the results obtained by Fujikake's experimental tests (Fujikake et al., 2009) and Jiang's numerical tests (Jiang et al., 2012). Modeling assumptions previously described were used in the analysis of the drop hammer numerical models. This parametric study on the drop hammer impact will lead to viable assumptions for future simulations of a barge impact.

3.3.1 Results for CSCM Concrete

To maintain much of the same concrete characteristics used in the Fujikake tests (Fujikake et al., 2009), unconfined compressive strength is set to 42 MPa and the maximum aggregate size is 10 mm. Unless otherwise stated, simulations were developed using the coarse mesh and the 0.15 drop height velocity.

3.3.1.1 Dynamic Increase Factors and Contact Algorithms

First, under investigation are a series of numerical models where the dynamic increase factor for the steel reinforcement and the contact algorithm were variables to consider. Various stiffness hourglass coefficients (HG) are also considered as they can alter or refine the results. Several coefficients, ranging from 0.0001 to 0.1, were selected to determine the sensitivity of hourglass control in the simulations. It should be mentioned that a full integration method was also utilized. This method does not require the use of hourglass controls as no approximation is made in the integration.

The first pair of results, Figure 3.10 and Figure 3.11 compare the DIF method for the steel reinforcements when the automatic contact algorithm is used. Analyzing the two impact force plots, the two DIF methods demonstrate similar results. The initial peak force exhibits close to identical values. At the third peak a minor increase in the peak force is observed in the Malvar method. The decrease in hourglass coefficients shows a decrease in the peaks observed in the response.

Both mid-span deflection time histories match the peak deflection very well. The result from the model with the HG = 0.1 shows a behavior that is similar to the behavior of deflection curve from Jiang's numerical results (Jiang et al., 2012). The effect of the steel DIF can be clearly observed in the free vibration phase of the impact, after approximately 15 ms. The FHWA method for DIF in the steel results in a marginal increase in deflection during the free vibration phase. However, the FWHA method with HG = 0.1 is the closest representation of the results reported by (Jiang et al., 2012). The Malvar designation for the DIF curve shows more rebound in the beam compared to that observed in the experimental results.

Observing the eroding contact in Figure 3.12 and Figure 3.13 there is greater effect on the chosen hourglass controls. Jiang et al. (2012) reported that eroding contact was used for the numerical models. In general, the peaks of the impact force time histories are lessened by this contact type, with a smaller difference in the initial peak. Peaks almost match the numerical model reported by Jiang et al. (2012), still slightly higher than the expected from experimental data. The displacement curves show a similar overall behavior with respect to the results from the automatic cases, where there is a small increase in the FWHA DIF results during free vibration. There was one anomaly seen in the FHWA curve set, when the HG = 0.1, hourglass energy observed in the model always remained less than 10% of the internal energy.

The results between the two contacts types are fairly similar, although the eroding contact type may show closer agreement to the findings in the literature. The automatic contact model still developed appropriate results and computational time was notably quicker than the eroding contact models. Due to this situation, the automatic contact type will be used in future models. If significant erosion is observed at the contact, it may be more appropriate to use eroding contact models.

3.3.1.2 Gravitational Forces

The results from the first set of numerical models reveal the effects from the additional loading due to gravity on all bodies of the model. Gravity was implemented at the start of the model rather than initiating the gravitational forces, in the dynamic relaxation phase, as discussed above. The impact response of the beam, seen in Figure 3.14, shows the results of simulations with and without gravity in the setup of the model. Other model conditions include a drop height of 0.15 m, automatic contact algorithm, and

dynamic increase factors for steel rebar as described by Malvar (1998). Overall, the impact force time histories show three peaks in the first 10 ms, which are present in both the Fujikake and Jiang results (Fujikake et al., 2009; Jiang et al., 2012). All impact responses result in greater peaks than was observed by both the experimental and EPDC cases. The impact forces show a minor change after the initial peak force is reached at about 2 ms. In the case of deflection at the mid-span, there was an almost identical match in the peak deflection and behavior of the curve when the hourglass coefficient is 0.1, when compared to EPDC model that was reported by (Jiang et al., 2012).

3.3.1.3 Stiffness versus Viscous Hourglass Control

Although LSTC (2013) suggests using stiffness controlled hourglass, (Jiang et al., 2012) reportedly used viscous hourglass controls in the numerical models. Hence, an investigation into the two types of hourglass controls was conducted to understand the effect of each type of hourglass control. Figure 3.15 displays the results of this investigation. The viscous hourglass control closely follows the peaks of the experimental data. The contact times of the impacts with viscous hourglass coefficients of 0.001 and 0.0001 are slightly shorter than the others. It can be seen in the deflection curves that these two curves result in a deflection that is continuously increasing. Observation of the model shows crushing of the concrete at the supports. This behavior is not the expected behavior of the beam, especially at a drop height of 0.15 m. Deflection of the two other viscous hourglass coefficients bound the smaller stiffness hourglass coefficients. The curve behavior of stiffness HG = 0.01 and velocity HG = 0.001 appear to have very similar patterns. The viscous hourglass type is more sensitive to changes in the coefficients and can quickly exhibit instability in the results.

3.3.1.4 Mesh Size

The previous series of results have used a coarse mesh configuration. The automatic contact algorithm and the Malvar designated DIFs for steel rebar were used in the models for the medium and fine mesh configurations, with a drop height of 0.15 m. Figure 3.11 should be consulted for the coarse mesh results, whereas Figure 3.16 and Figure 3.17 report the results from the medium and fine mesh configuration, respectively. As mesh sizes decrease so does the stability of the results, as smaller hourglass coefficients are considered. In the coarse mesh, there are no results in which the concrete crushes at the supports, i.e., where the deflection curve indicates a continuous increase in deflections. When these patterns of continuous deflections are observed, it is common to see impact force curves that do not conform to the expected response. In the medium mesh results, with HG = 0.0001, the third spike does not reach a range like that of other results and the contact time is about 3 ms less than the other results.

In the fine mesh results, the two smallest hourglass coefficients resulted in instability. The impact force of HG = 0.001 shows a much prolonged fluctuation, where the contact time exceeds 22 ms. The smallest hourglass results in a contact time that is less than 10 ms. In regards to the deflection curve, the fine mesh series resulted in no curve that appears to fully converge to the experimental data, however the results show attributes of the numerical results from literature.

3.3.1.5 Variations in Drop Height

As discussed earlier, the change in drop height means that the initial velocity of the drop hammer changes. For this particular study, the medium size mesh was used. The results of the 0.3, 0.6, and 1.2 m drop height simulations are reported in Figure 3.18,

Figure 3.19, and Figure 3.20, respectively. The results from the 0.3 m drop height have some obvious stability issues with the largest and smallest hourglass coefficients. The hourglass coefficient of 0.01 has the most stability and gives appropriate approximation of the impact force. The deflection curve, with HG = 0.01, show approximate results, although not the best match. The force curve with HG = 0.001, also gives an appropriate response to the impact force time histories. The deflection curve is even more closely matched to the numerical model in the Jiang et al. (2012).

In the impact response from the 0.6 m drop height, there is still evidence of instability in some of the results. Instead of bounding the appropriate results, as seen in the previous drop height, here the instability is only seen in the smaller coefficient values. The force time series with HG = 0.001 appears to show promising results, however a few indications, such as the instantaneous change form decreasing to increasing at about 1.5 ms lead to question the stability of this coefficient. Furthermore, analyzing the deflection curve for the same hourglass coefficient can quickly conclude that this coefficient does not capture the peak deflection. The next smaller number shows even more unstable values, where that crushing behavior at the supports was once again observed. Alternatively, the curve with HG = 0.001 was the best fit to the expected results. Images of the beam with HG = 0.001 were taken analyzing for von Mises stress (Figure 3.21) and plastic strain (Figure 3.22). The mesh size makes it possible to see the contribution from the shear reinforcement. Diagonal concentrations of stress are indicative of the diagonal cracks that can are observed when bending a RC beam. The plastic strain figure shows the damaged elements of concrete. The areas of plastic strain are located in places where these crack line might be expected.

Lastly, the 1.2 m drop height results depict a similar pattern where smaller hourglass coefficients are unable to manage appropriate results for the impact scenario. Only hourglass coefficients of 0.001 and 0.0001 were able to predict a reasonable response for both the force and deflection curves. Most appropriate results were when a coefficient of 0.01 was used. There is about 50 kN overestimate in the peak impact force, within the first 3 ms. The experimental and numerical models from previous literature sources are approximately the average response during the free vibration phase. In the deflection response, there is good agreement in the first 14 ms of the response. The simulations conducted using HG = 0.1 and 0.01 follow the experimental response better than the EPDC model post peak deflection and represent the impact well overall. Through investigating several velocities, it is evident that the hourglass coefficient becomes a more crucial parameter for structural response assessment. As dynamic rate effects increase due to higher impact velocity, so does the effect of larger coefficients.

3.3.2 Results for KC Concrete

To capture the concrete characteristics reported in the experimental tests, the unconfined compressive strength of concrete was initially set to 42 MPa. Although the aggregate size is not a parameter in this case, Poisson's ratio and the density were selected to be 0.2 and 2400 kg/m^3, respectively. For further details of the model, the previous section on concrete constitutive models should be referenced. Beginning the investigation of this material model, various drop heights were considered. Then because of the results, an investigation of the influence of the material inputs was conducted to derive more appropriate response.

3.3.2.1 Variations in Drop Height

Results of the 0.15 m drop height can be seen in Figure 3.23. The impact curve behavior shows approximately good results especially with the first three hourglass coefficients. The peak impact force, at about 2.5 ms, was overestimated, but by a similar margin of the results seen in the previous material model. More instability in the result curves is present in the smaller values of hourglass coefficients. The impact curve with HG = 0.001 represents the best fit to the reference data. Deflection curves show that the KCC model captures concrete recovery better than the CSCM model, with a final deflection of about 3 mm at the end. All models, except H = 0.0001, show similar responses. They are able to record the peak deflection at approximately the correct time and all agree on the same free vibration phase.

The 0.3 drop height, Figure 3.24, is where the model begins to lose accuracy. The peak impact force ranges from 50 kN to 150+ kN of error. Furthermore, the data curve begins to lose the sinusoidal shape that was reported by Jiang et al. (2012). Another important feature of the impact plot beginning at ~2.5 ms where there is reportedly no impact force. This behavior is unlikely in reality. Hourglass coefficients of 0.1 and 0.01 results in the most stable results and estimate the peak deflection and the time at which it occurs well. A similar pattern can be seen in Figure 3.25 as the drop height is increased to 0.6 m. Initial peak forces deviate further from the findings in literature. Despite this, general trends are still captured, with similar end times. Once again, the smallest of the hourglass coefficients does not follow the general trend of the other curve. This can be due to the error in the deflection curve, such as was seen in the CSCM results. Other deflections follow the general trend well but overestimations are typical, both in the

deflection and the time of maximum deflection. Behavior of the experimental deflection results seems to be better matched than the other numerical result.

Images were taken of the KC concrete simulation results for a drop height of 0.6 m, similar to the CSCM concrete beam. For this case, Figure 3.26 shows the von Mises fringe component and Figure 3.27 is the plastic strain for the KC concrete. The mesh resolution was twice as large as the figures presented for the CSCM concrete beam. Even with the larger meshing pattern the contribution of the reinforcement is still evident. At the t = 5 ms the stress has a higher concentration on the edges than seen with the previous model. Because the peak quickly experiences high levels of plastic strain, there appears to be small levels of stress at the bottom of the beam.

The same trend is once again captured for the 1.2 m drop height (See Figure 3.28). There was a higher degree of discrepancy in the peak impact force, where 100-200 kN differences can be seen. The deflection was 5-10 mm greater than the peaks expected in the reference curves. In attempt to capture better results for these results, the 0.3 m drop height simulations were tested with various changes in modeling assumptions to analyze the influence of parameters on the impact response.

3.3.2.2 Eroding Contact

The eroding contact was examined in this set of results to ensure that this material model still behaves appropriately. As this parameter does not directly influence the behavioral aspects of materials, this should make no more difference than was seen in the example with the CSCM material. Figure 3.29 shows the impact response of the beam with a drop height of 0.3 m. As was expected, there were no significant changes to the

impact response. There was some control problems with one of the curves, which parallels the response that was given in the other eroding controlled simulations.

3.3.2.3 Steel Dynamic Increase Factor Curve

Previous models used the Malvar designated DIF curve for the steel rebars. Another curve was the curve proposed by the FHWA. The example DIF curve was used in this set of analysis cases. The impact curves from these simulations (Figure 3.30) show that the zone where there is no impact force, at about 2.5 ms, has been minimized. However, this had minimal effect on the peak impact force at the first peak. The deflection curves were approximately similar to the Malvar DIFs. It appears that the FHWA DIF deflection curve results in greater variation, but still appropriate to the two reference curves.

3.3.2.4 Concrete Dynamic Increase Factor Curve

Within the Murray (2007), there is an approximated curve of DIFs for the CSCM material. This was used in place of the CEB/Malvar curve, in attempt to approach more similar results to that of the reference curves. Results from this parameter can be found in Figure 3.31. The impact force curves show much higher levels of instability than reported with the CEB/Malvar DIF concrete curve. Even in the higher hourglass coefficients, predictions can be made and validated with increased deflection based on the increased contact time. The deflection time history responds in a similar manner, where the instable curves do not portray appropriate behavior and the two that suggest more stability have deflections that are overestimated by about 8 mm.

3.3.2.5 Viscous Hourglass Control

Although viscous hourglass control will not directly change the response of the concrete, hourglass coefficients can change the peak impact forces. This phenomenon can be observed in many of the previous series of results. The type of hourglass control may only contribute to the effectiveness to govern the results. Figure 3.32 shows a series of simulations with viscous hourglass control. Also included is a curve where hourglass controls are turned off. It was found that the option with no hourglass control yielded the best results. Viscous hourglass was able to control the peak impact force recorded, even though this was relatively minor. While this coefficient did not alter the peak, the free vibration phases changed significantly and the deflection curve showed further deviations with increasing the hourglass coefficient.

3.3.2.6 Unconfined Compressive Strength

The unconfined compressive strength is one of the three parameters that are used to derive the fit values for the material model. Several somewhat typical values for the concrete strength were selected, ranging from 30 MPa to 48 MPa. Figure 3.33 displays the impact results with varying concrete compressive strengths and a constant hourglass of 0.01. The impact forces show some effect due to the change in strengths. As the strength is increased, the peak impact force does as well. The peaks have a range of about 40 kN with the change in strength alone. The general trend is followed by all four curves, except when the concrete strength is 30 MPa, possibly due to hourglass controls. Despite this curve not following the “common trend”, it still represents the impact well. Observing the deflection curves, variations in the impact deflection is similarly recorded.

In this case, when the concrete strength increases, less overall deflection was reported. All curves apparently represent the reference data well.

3.3.2.7 Poisson's Ratio

The second input parameter to formulate generic fitted data, Poisson's ratio, is investigated as a parameter contributing to the response of the impact. Figure 3.34 shows the results of this study, where both the Poisson's ratio and the hourglass coefficient are changed. There is some variability in the beam response, but the variability is insignificant. The curves are grouped by color to highlight the response curves that are more strongly associated with the hourglass controls. This behavior is seen in both plots, with less variability in the deflection plot.

3.3.2.8 Concrete Density

The density is also used to automate parameters fitting in the KCC material model. Various densities were chosen and the response was plotted in Figure 3.35. The density of the concrete had no effect on the initial peak impact force. Some variability in the response can be seen after this initial impact, but variations are inconsequential. As seen in the deflection curves, the density has a trivial effect on the response of the beam impact. The deflection curves lie so close to one another, they are hard to distinguish.

3.3.2.9 Effects of Damping

In attempt to control the impact forces, damping was added to the model. Global damping was introduced to closer represent reality in a structure. Damping ratios of 0%, 1%, 2%, and 5% were used to illustrate the effect of damping. In addition to damping ratios, hourglass controls were altered in this study. Figure 3.36 displays the response

from the investigation in damping. The impact forces were, seemingly, slightly affected by the levels of damping investigated. A damping ratio of about 5% can decrease the initial peak impact, equivalent to the effect that the hourglass coefficients have. Drawing conclusions further from the deflection curves, it its evident that damping ratio can effectively decrease the deflection inspected in the model, despite the small effect on the recorded impact force.

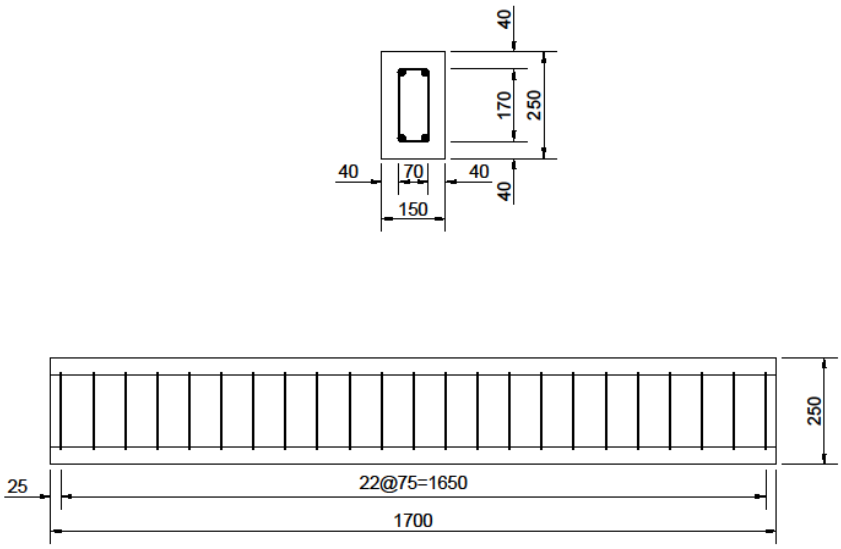

Figure 3.1 Beam geometry with rebar arrangement.
Cross-section (above) and side-view (below) (Fujikake et al., 2009)

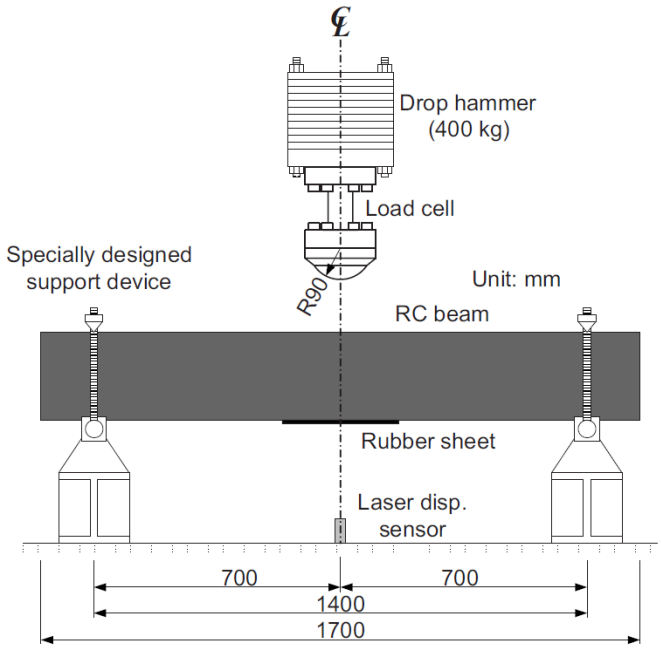

Figure 3.2 Experimental setup for tests (Fujikake et al., 2009)

Figure 3.3 Experimental setup (Adhikary et al., 2012)

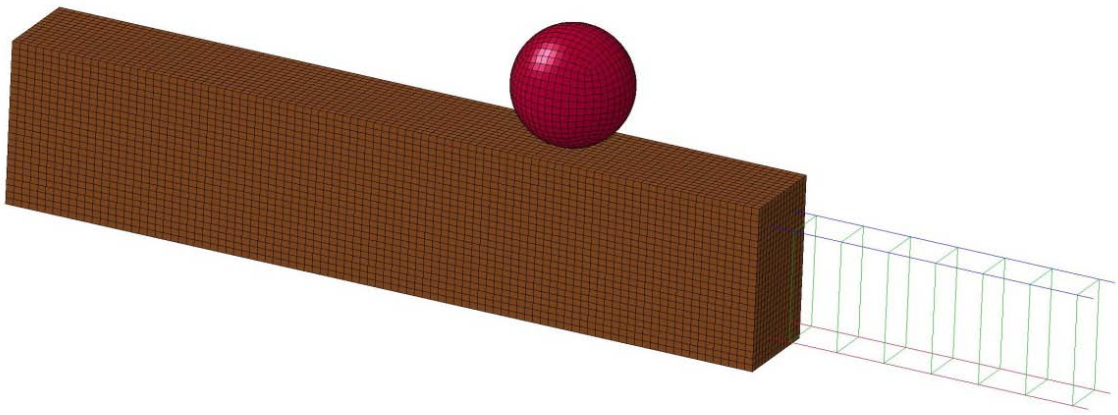

Figure 3.3 FE model geometry with section cut away to see reinforcement

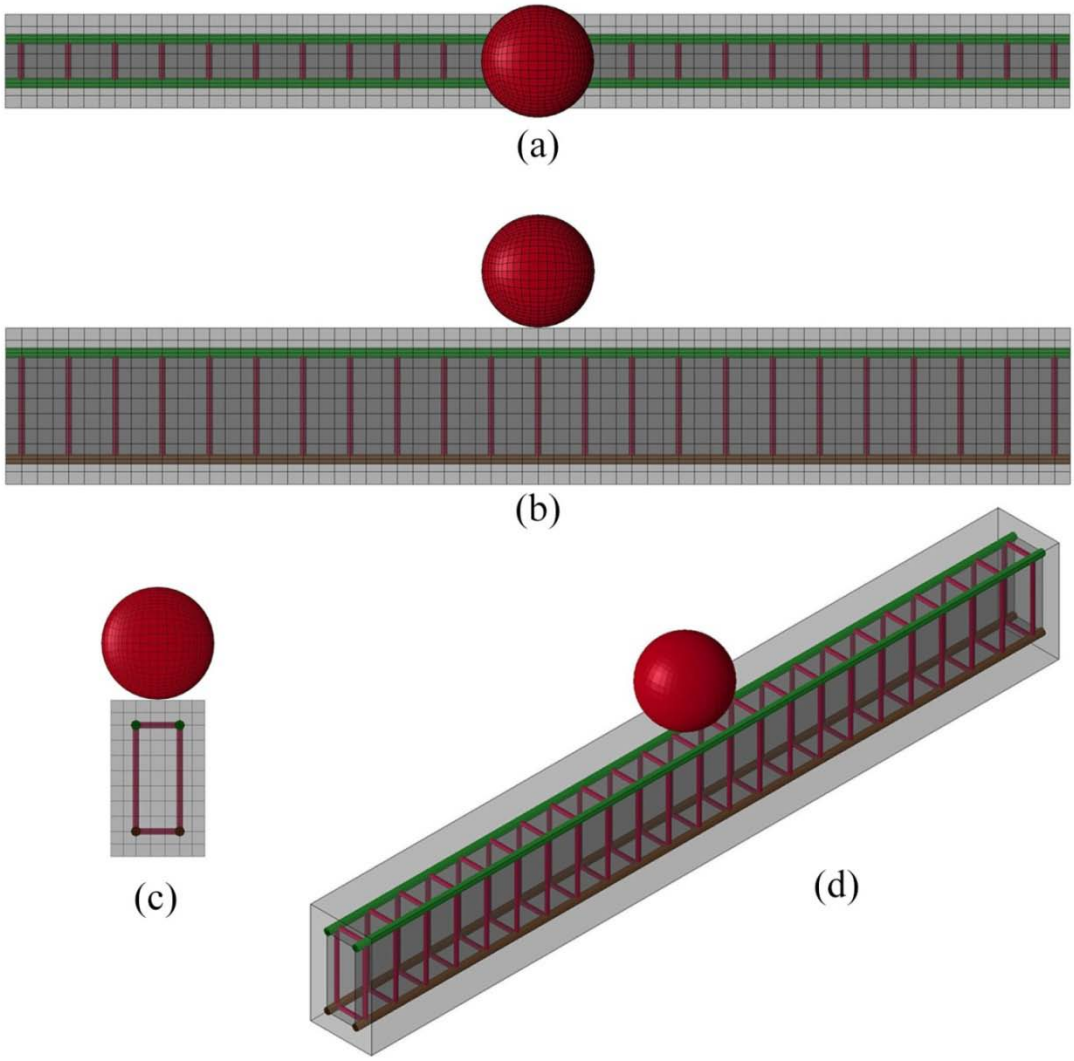

Figure 3.4 Top (a), front (b), and side (c) faces and isometric view of beam geometry used in beam impact study

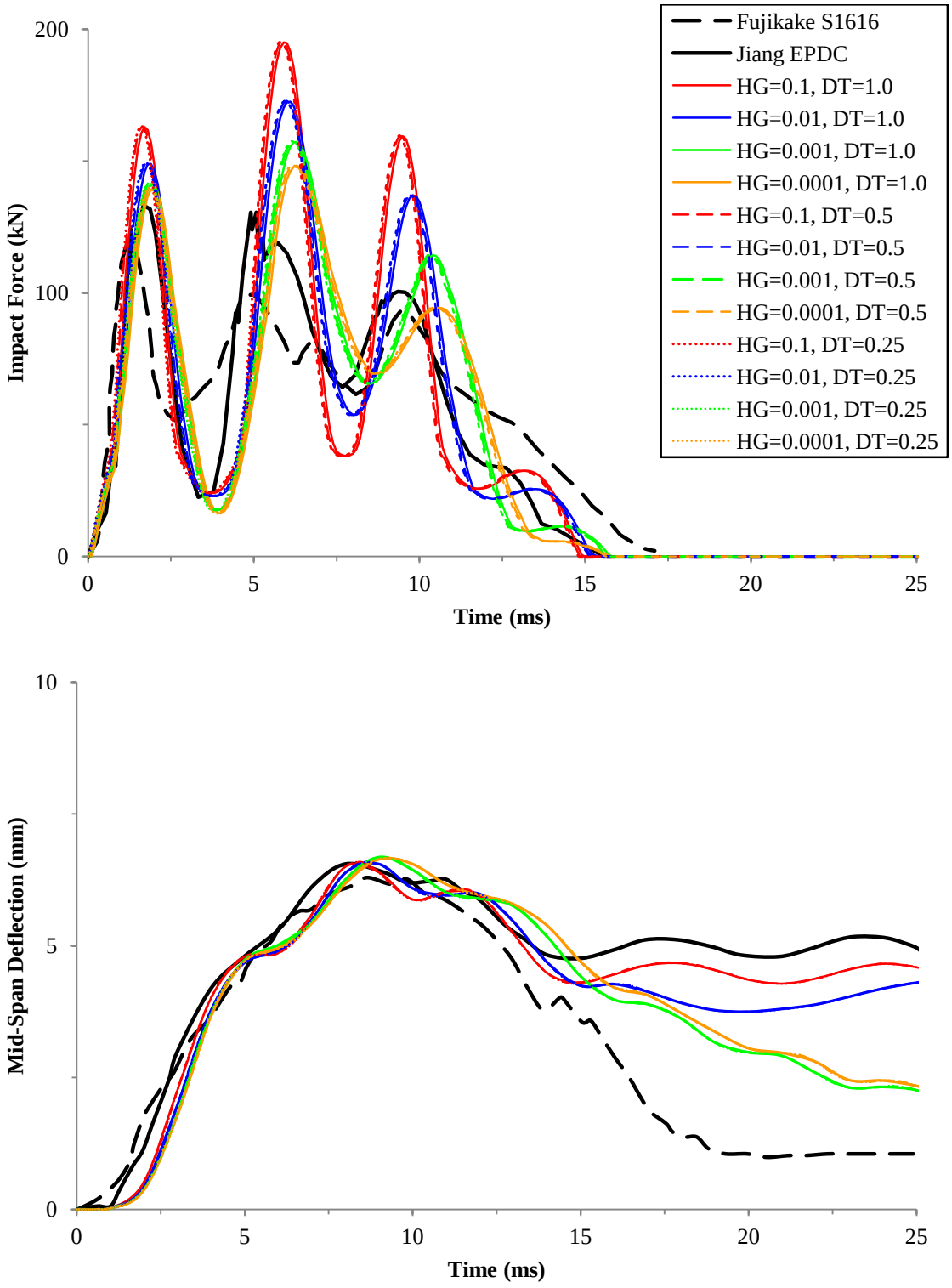

Figure 3.5 Impact force (above) and deflection (below) of RC beam; CSCM concrete, 0.15 m drop height, automatic contact, Malvar designated DIF, and coarse mesh size

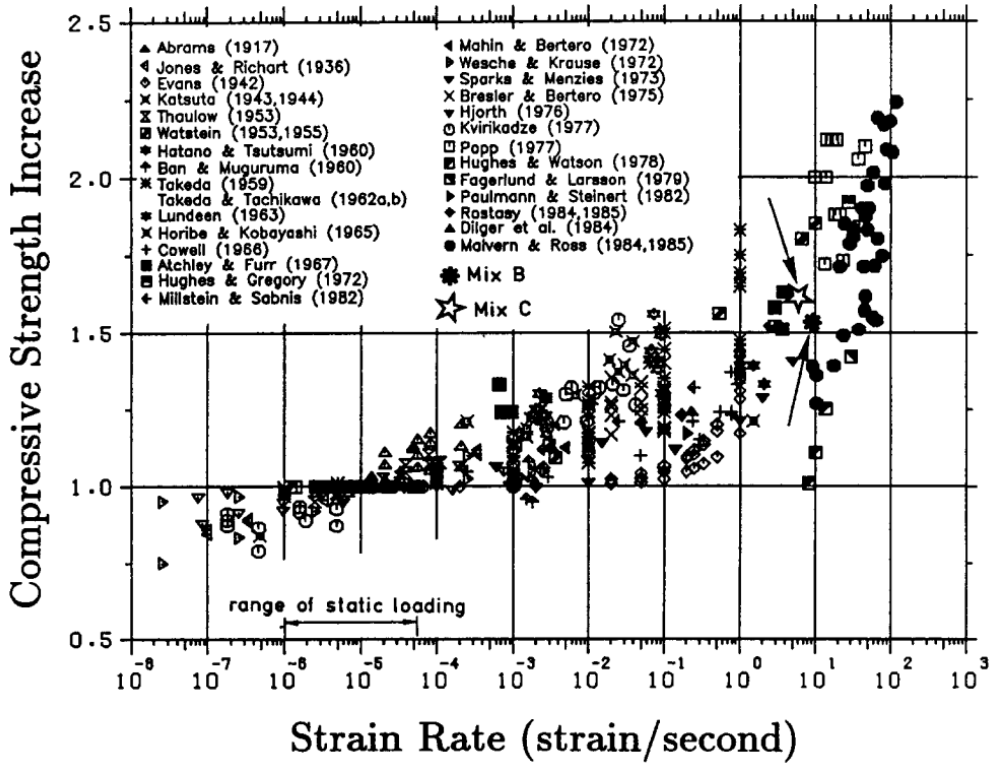

Figure 3.6 Collected data showing increases in compressive strengths with increase in strain rates (Bischoff and Perry, 1995)

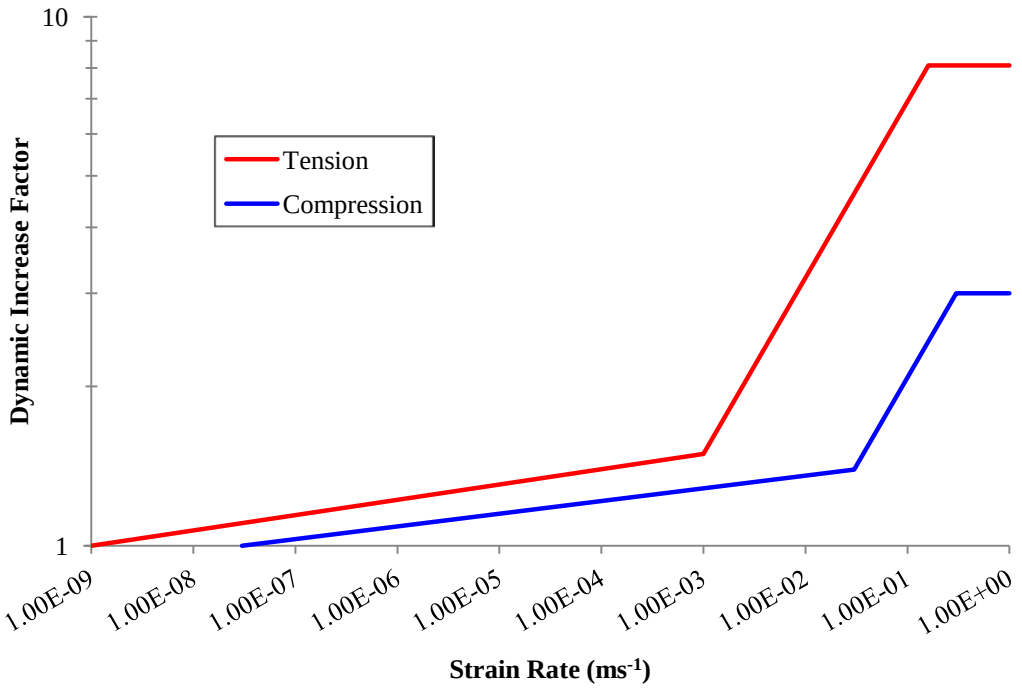

Figure 3.7 Strain rate effects of concrete using CEB/Malvar formulation

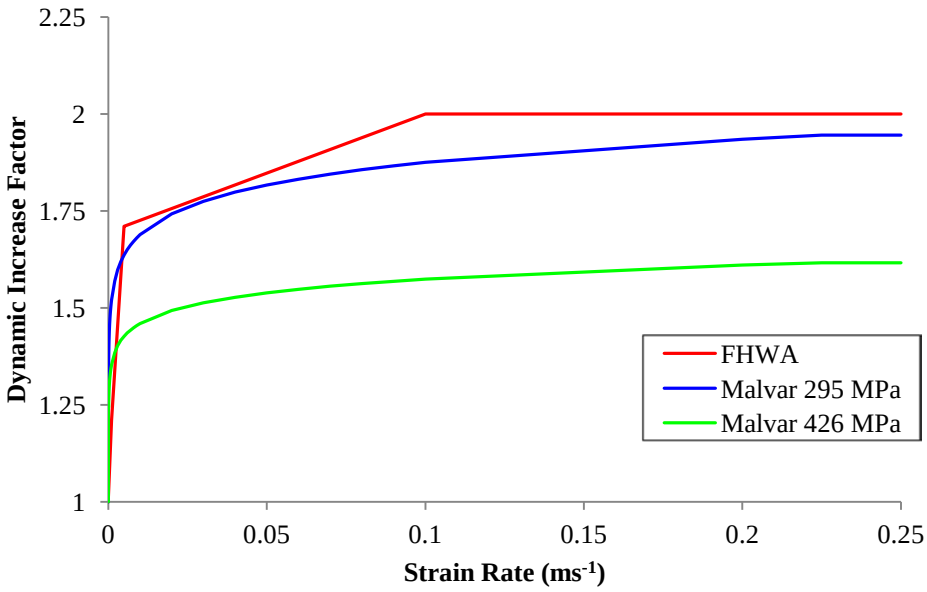

Figure 3.8 Comparison of strain rate effects for reinforcing steel rebars

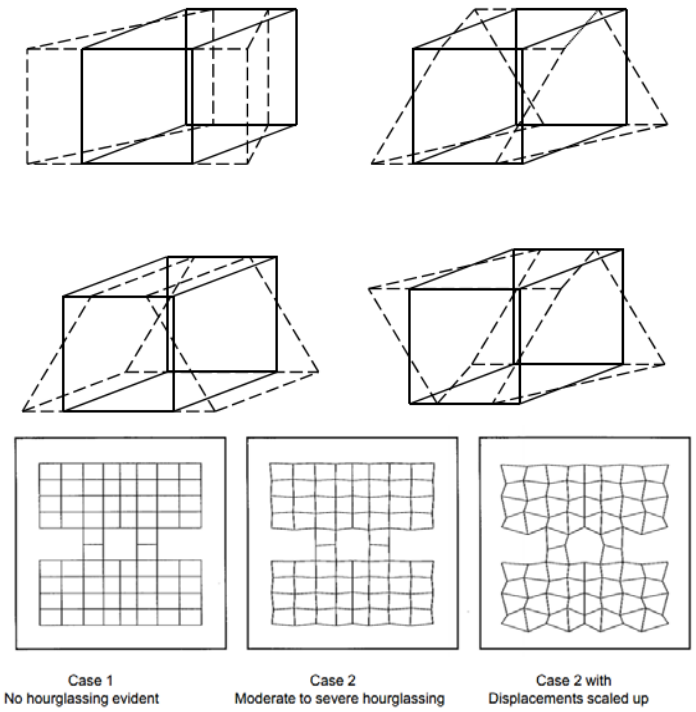

Figure 3.9 Example hourglass modes in solid element (above) and shell elements (below) (LSTC, 2013)

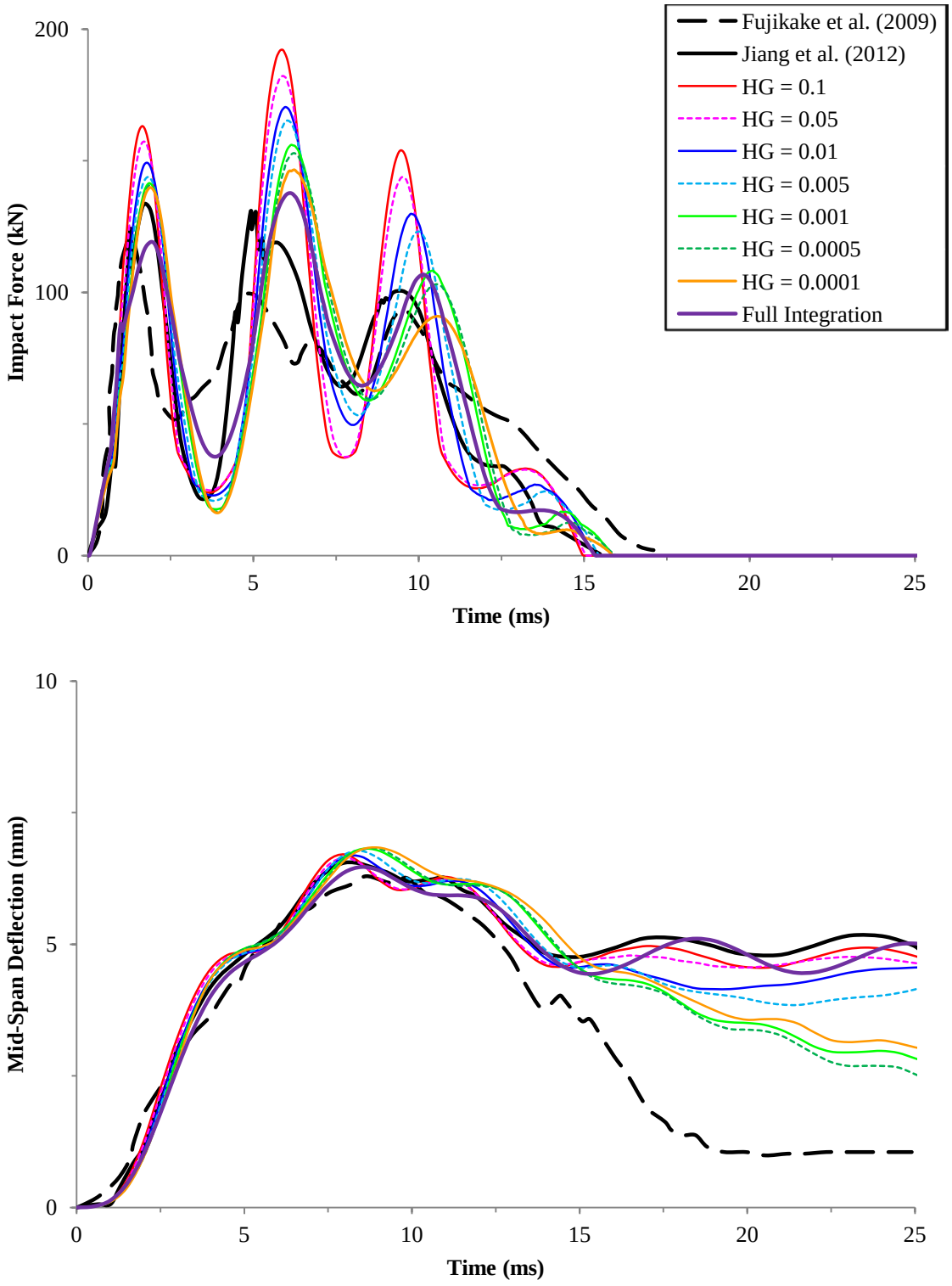

Figure 3.10 Impact force (above) and deflection (below) of RC beam; CSCM concrete, 0.15 m drop height, automatic contact, FHWA designated DIF, and coarse mesh size

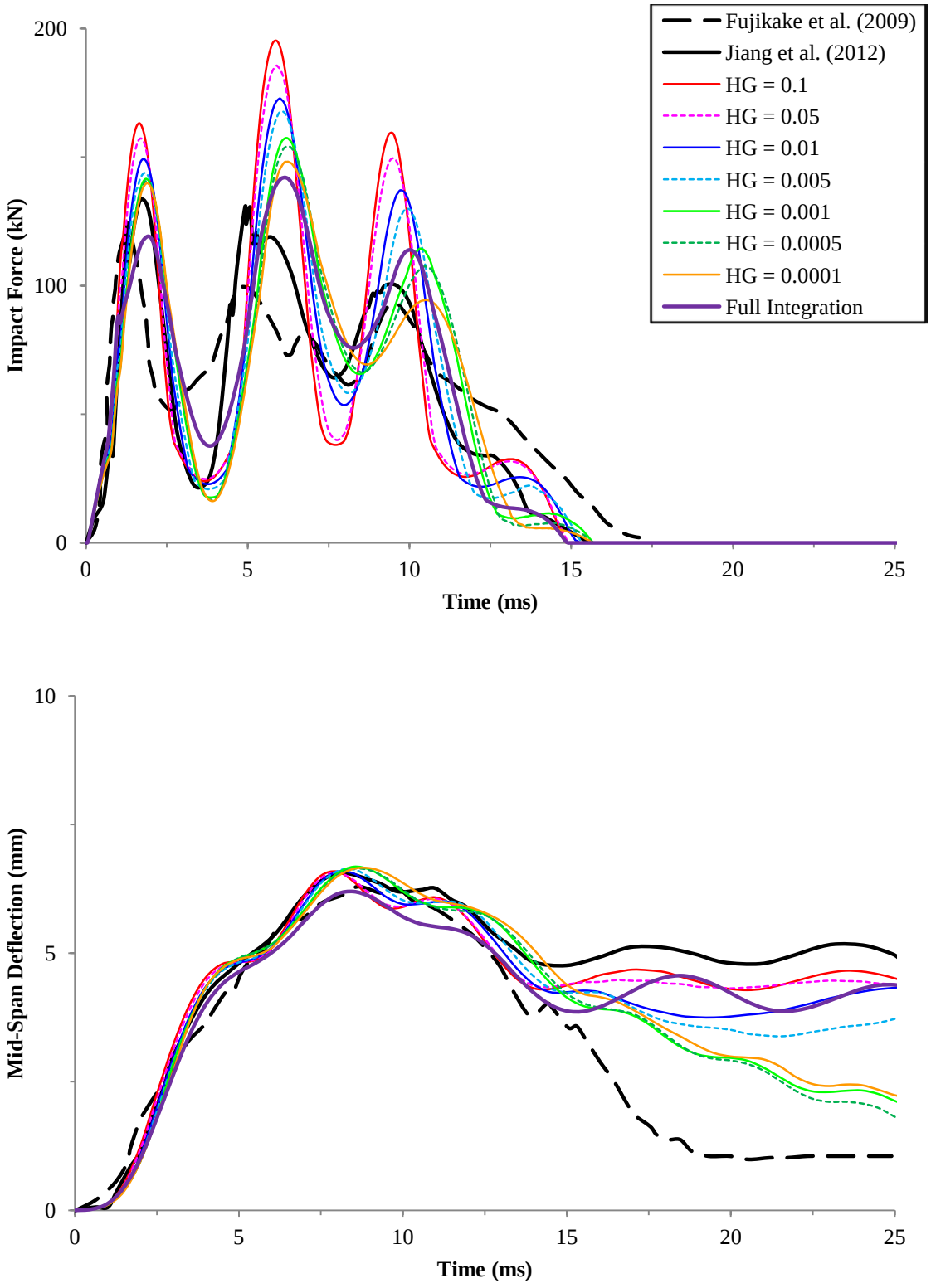

Figure 3.11 Impact force (above) and deflection (below) of RC beam; CSCM concrete, 0.15 m drop height, automatic contact, Malvar designated DIF, and coarse mesh size

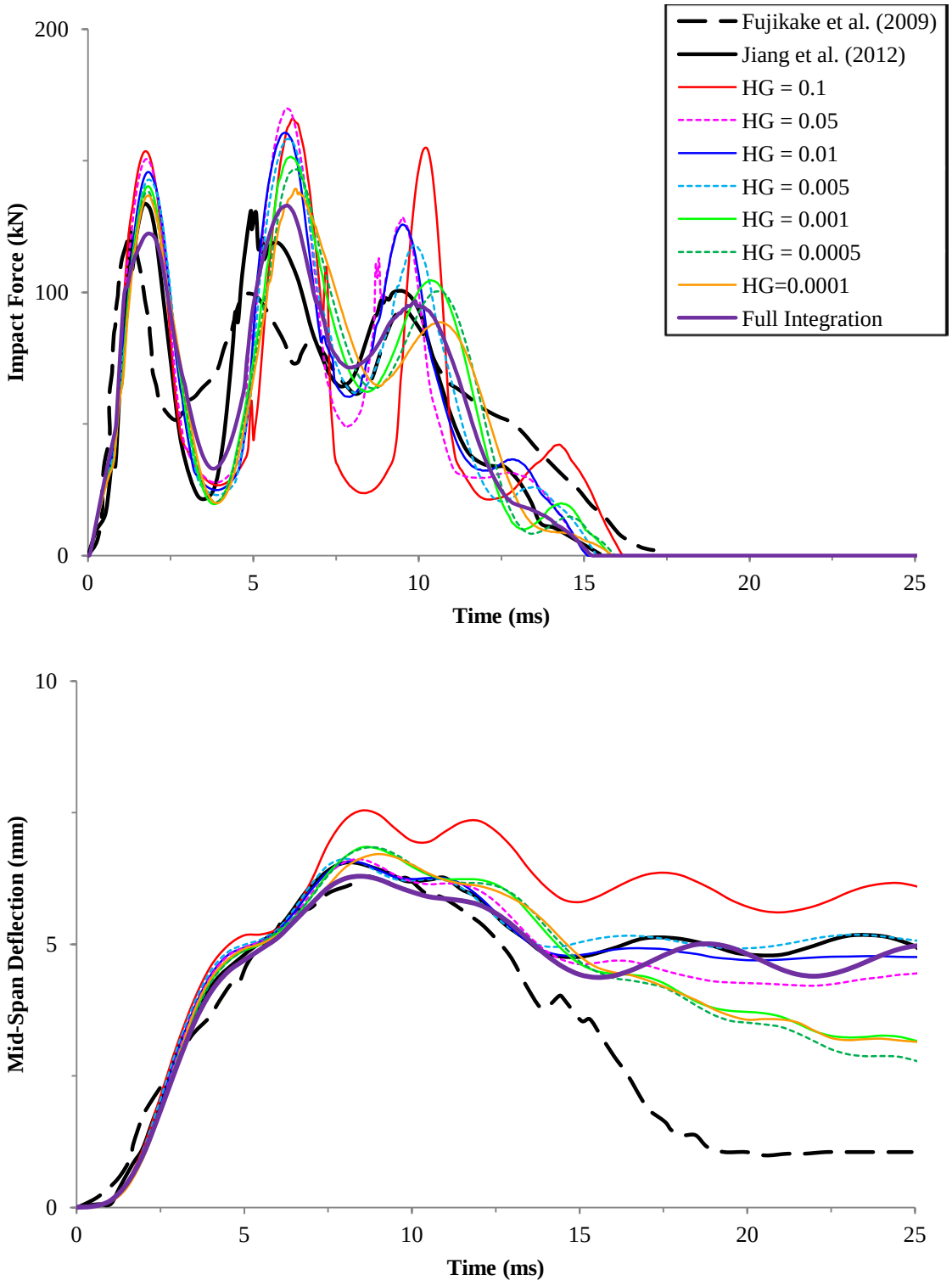

Figure 3.12 Impact force (above) and deflection (below) of RC beam; CSCM concrete, 0.15 m drop height, eroding contact, FHWA designated DIF, and coarse mesh size

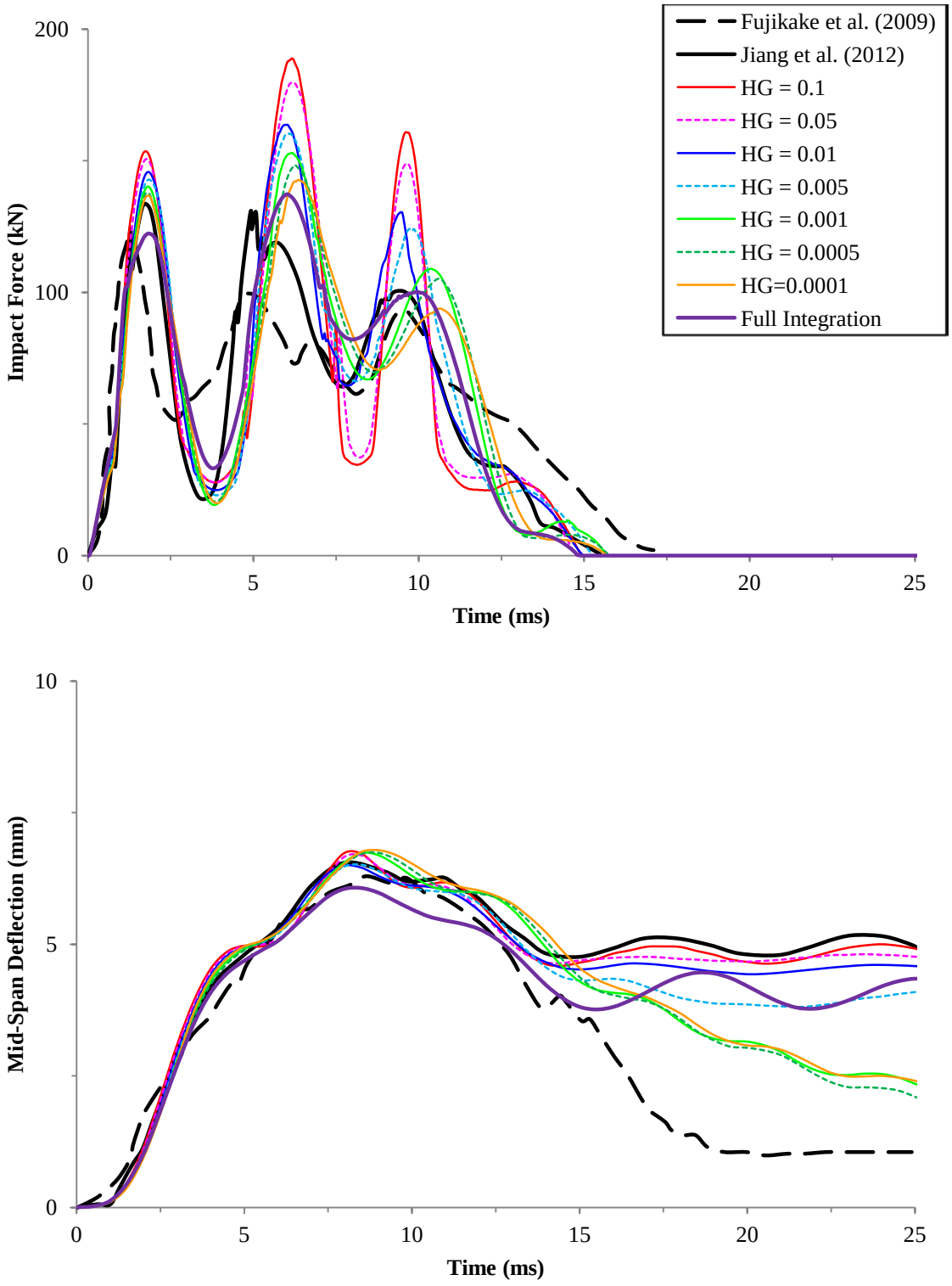

Figure 3.13 Impact force (above) and deflection (below) of RC beam; CSCM concrete, 0.15 m drop height, eroding contact, Malvar designated DIF, and coarse mesh size

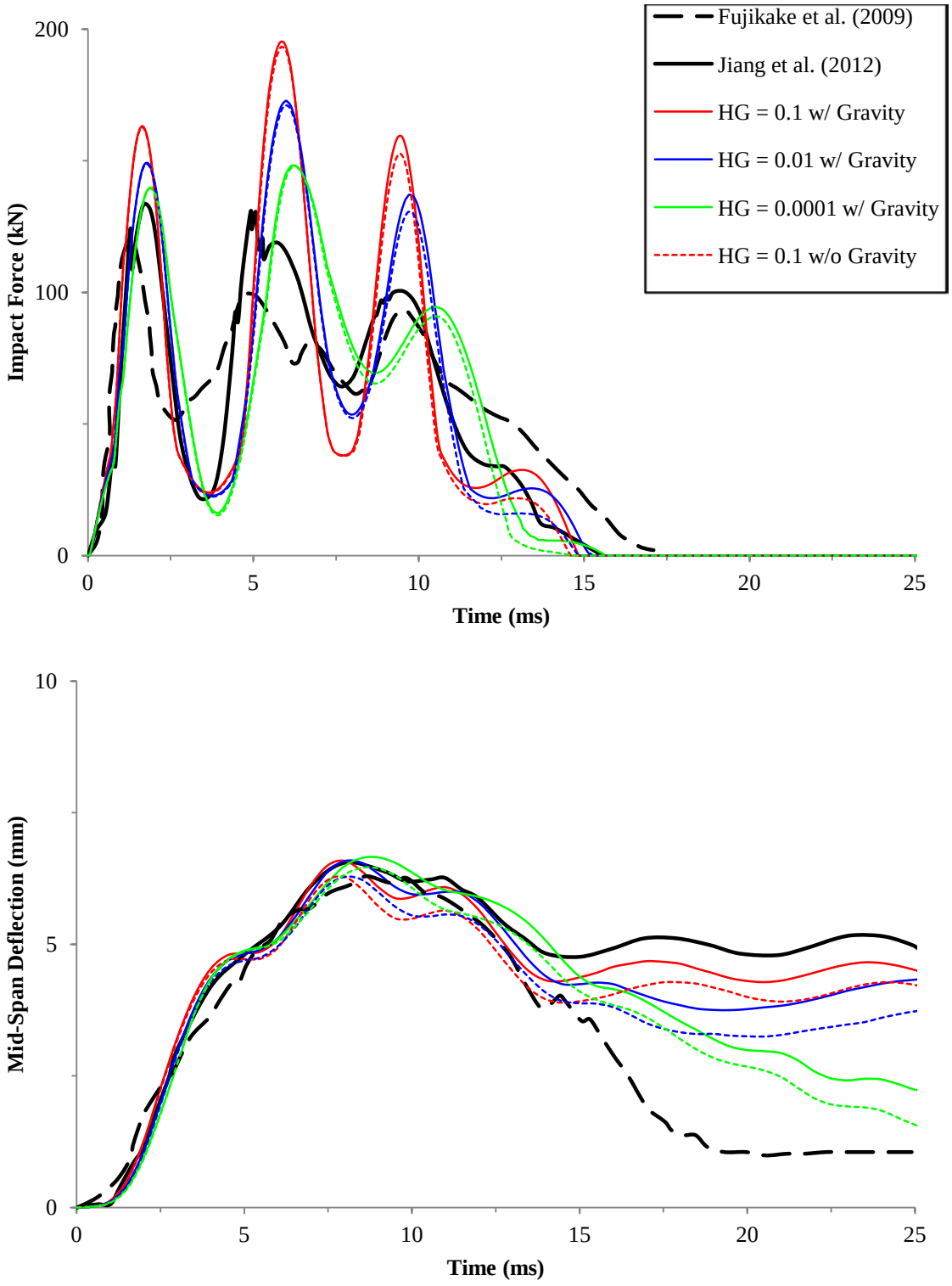

Figure 3.14 Impact force (above) and deflection (below) of RC beam; CSCM concrete, 0.15 m drop height, automatic contact, Malvar designated DIF, and coarse mesh size, with and without gravity load

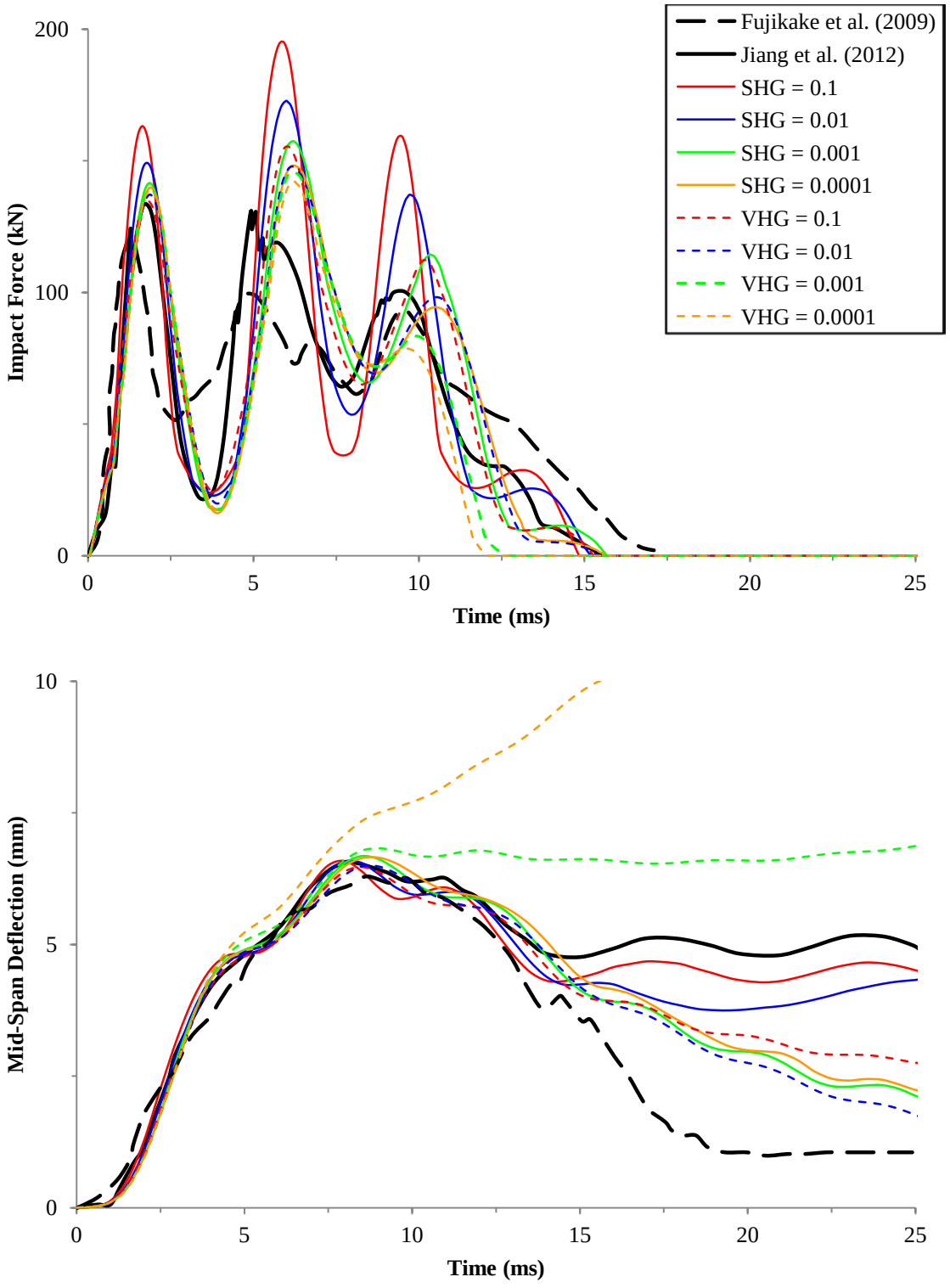

Figure 3.15 Impact force (above) and deflection (below) of RC beam; CSCM concrete, 0.15 m drop height, automatic contact, Malvar designated DIF, coarse mesh size, different hourglass types

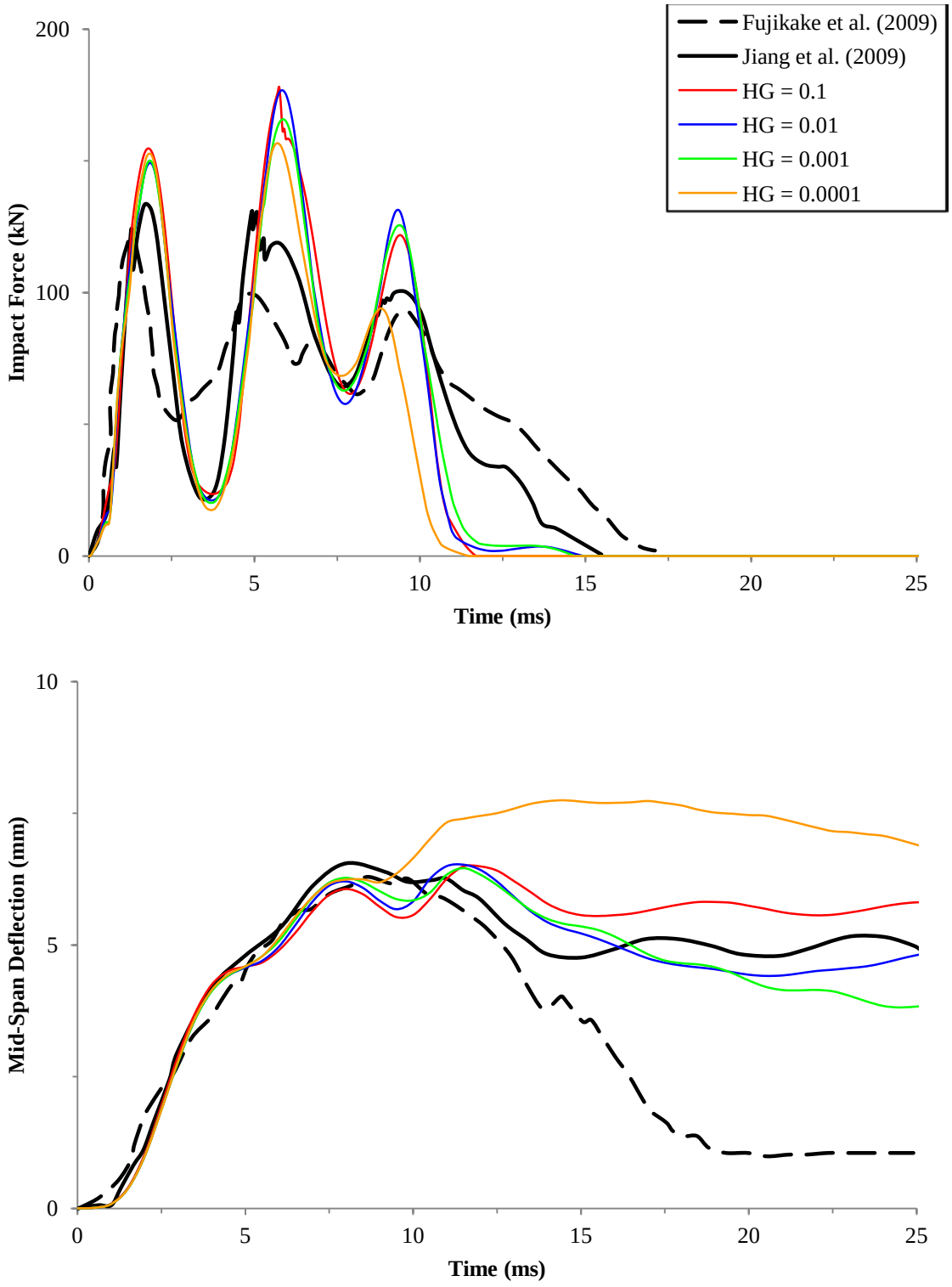

Figure 3.16 Impact force (above) and deflection (below) of RC beam; CSCM concrete, 0.15 m drop height, automatic contact, Malvar designated DIF, and medium mesh size

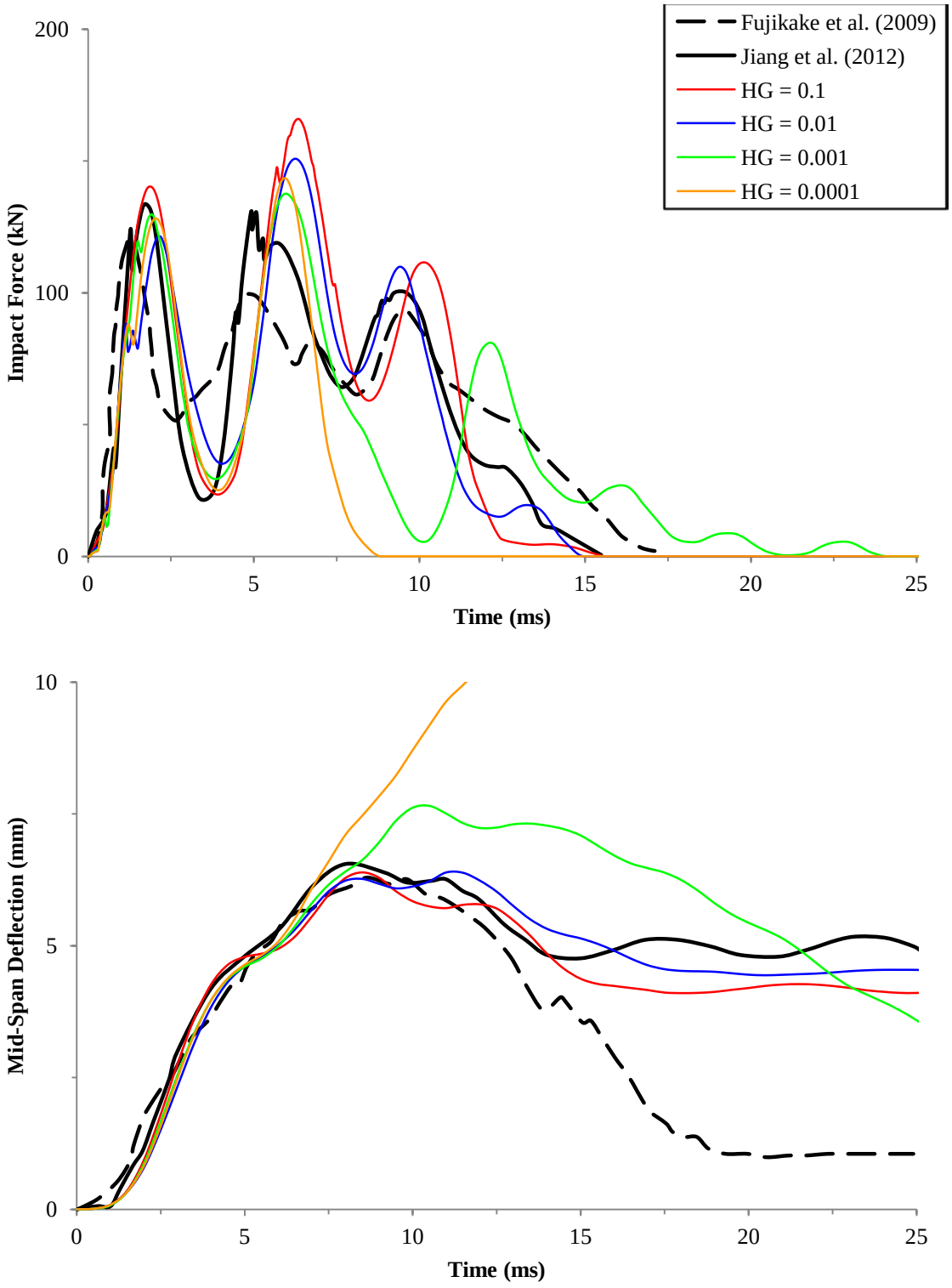

Figure 3.17 Impact force (above) and deflection (below) of RC beam; CSCM concrete, 0.15 m drop height, automatic contact, Malvar designated DIF, and fine mesh size

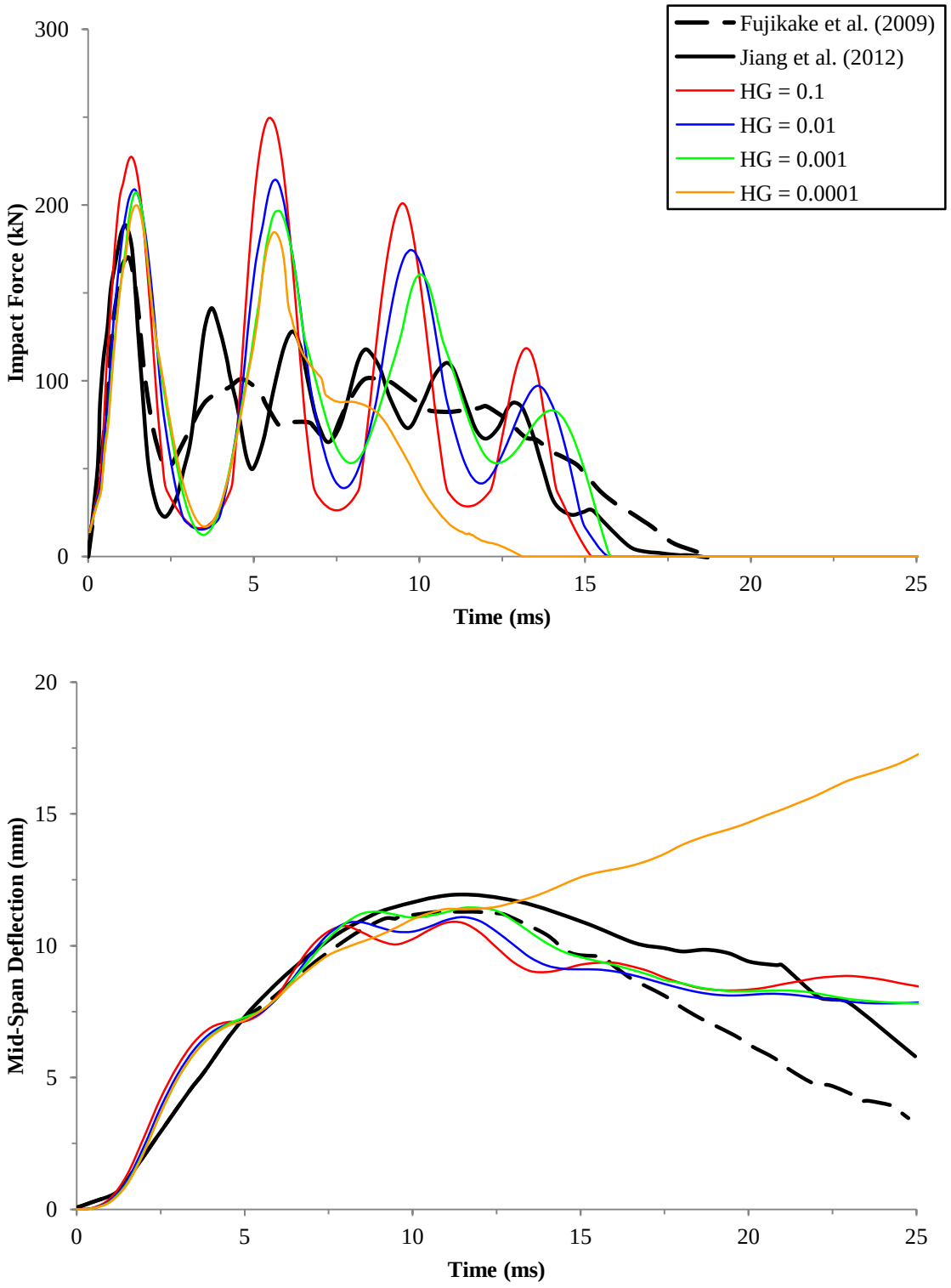

Figure 3.18 Impact force (above) and deflection (below) of RC beam; CSCM concrete, 0.3 m drop height, automatic contact, Malvar designated DIF, and coarse mesh size

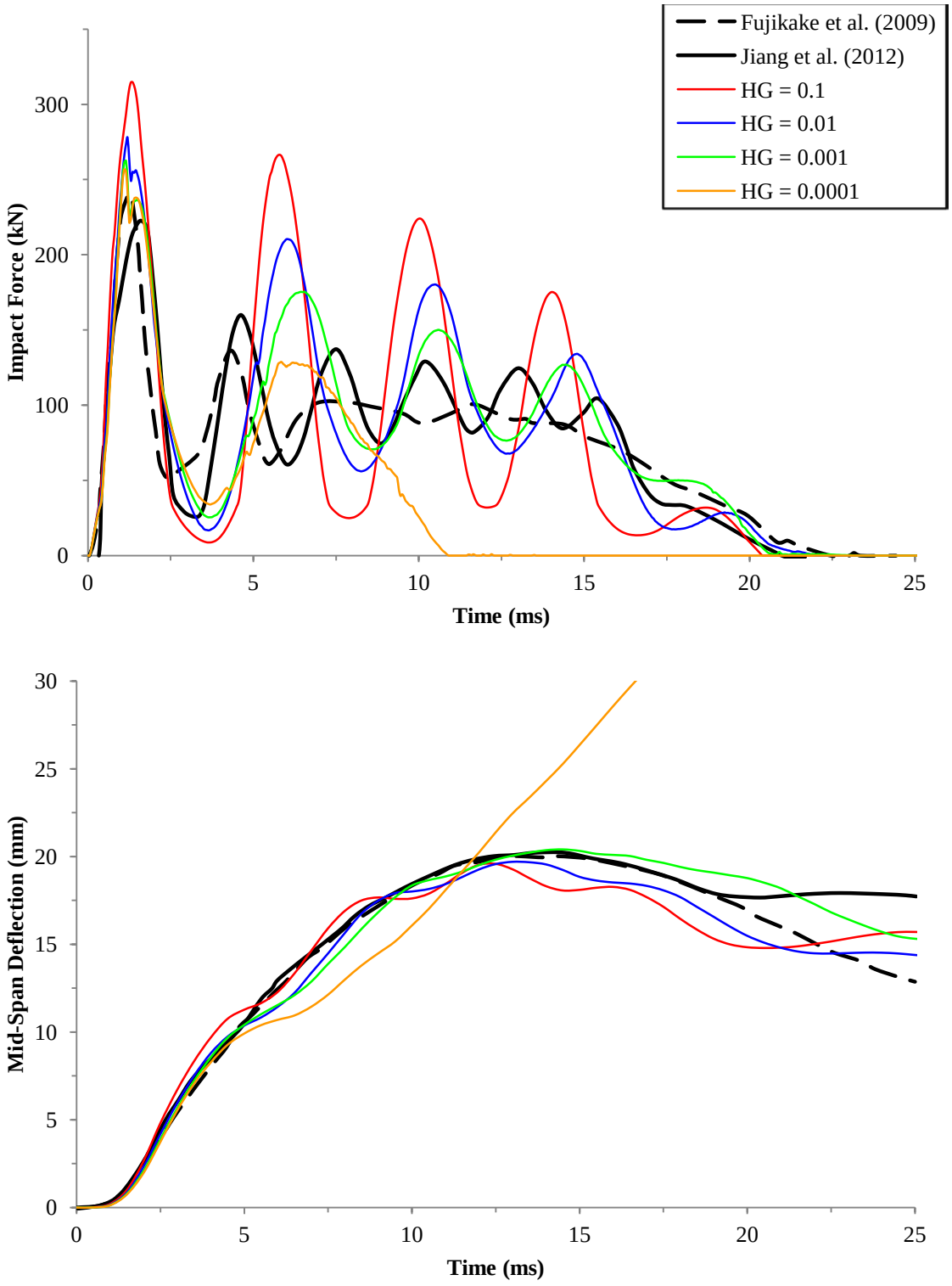

Figure 3.19 Impact force (above) and deflection (below) of RC beam; CSCM concrete, 0.6 m drop height, automatic contact, Malvar designated DIF, and coarse mesh size

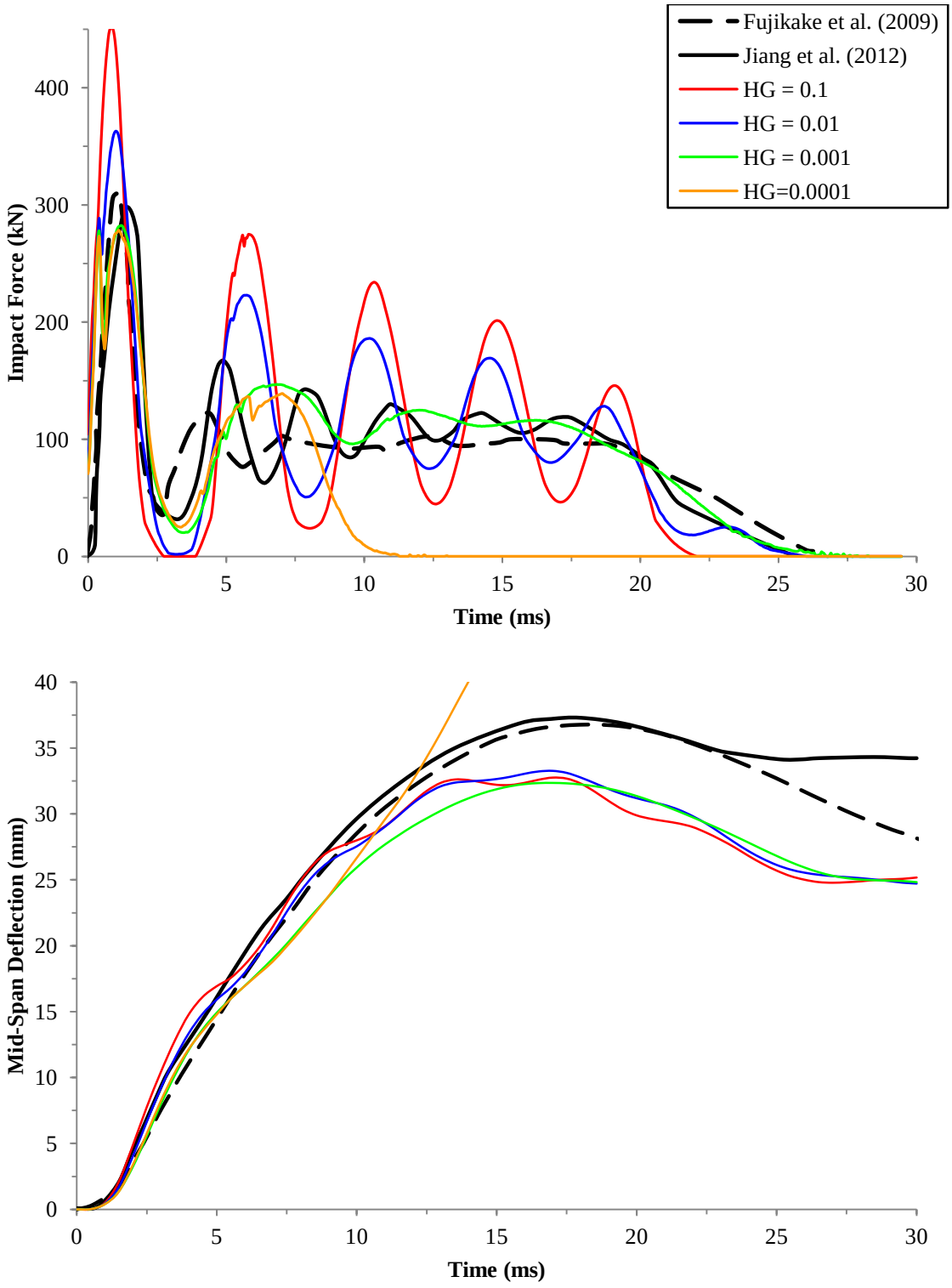

Figure 3.20 Impact force (above) and deflection (below) of RC beam; CSCM concrete, 1.2 m drop height, automatic contact, Malvar designated DIF, and coarse mesh size

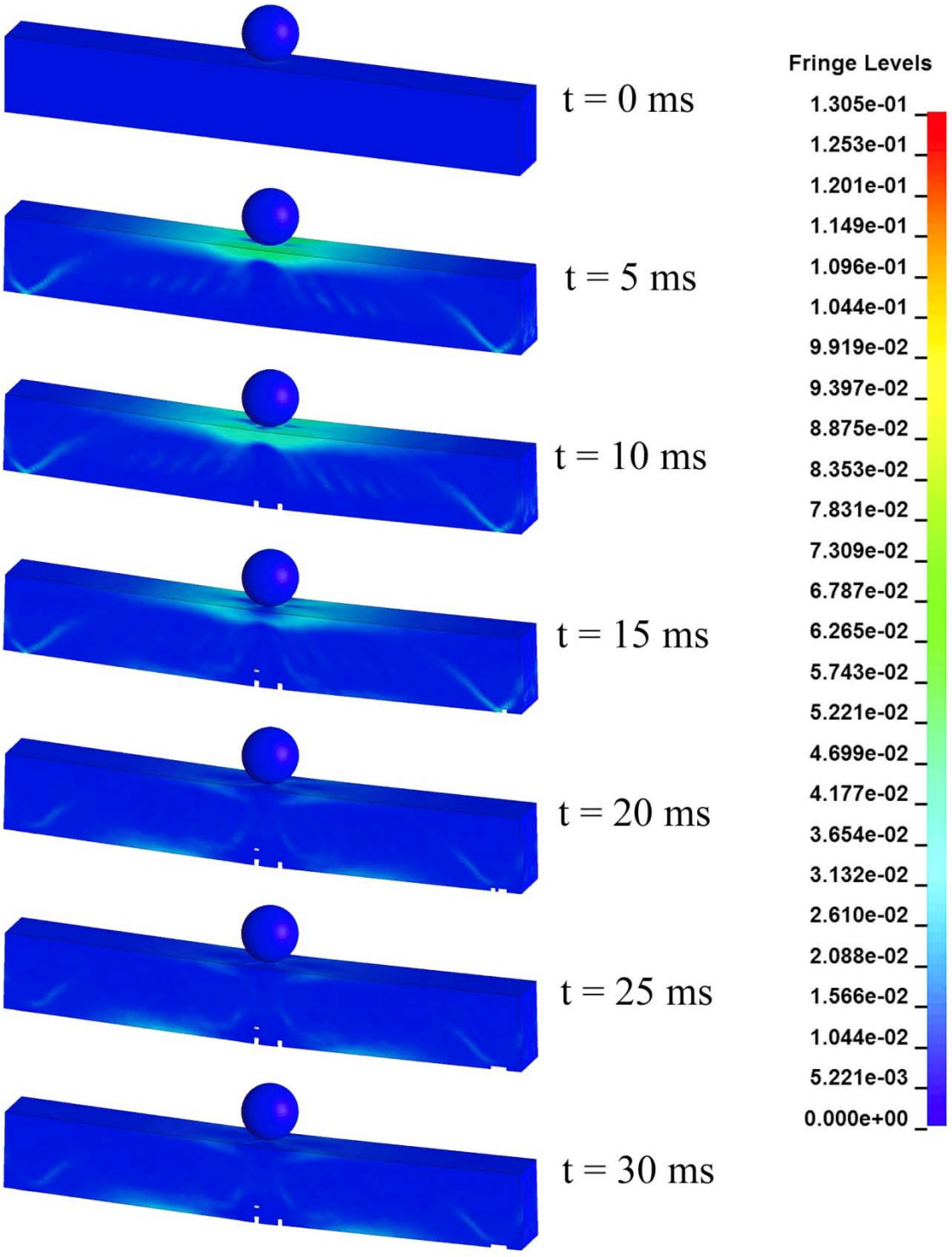

Figure 3.21 Snapshots of 0.6 m drop hammer impacting CSCM concrete beam with medium mesh size. Fringe displays distribution of von Mises stress in concrete

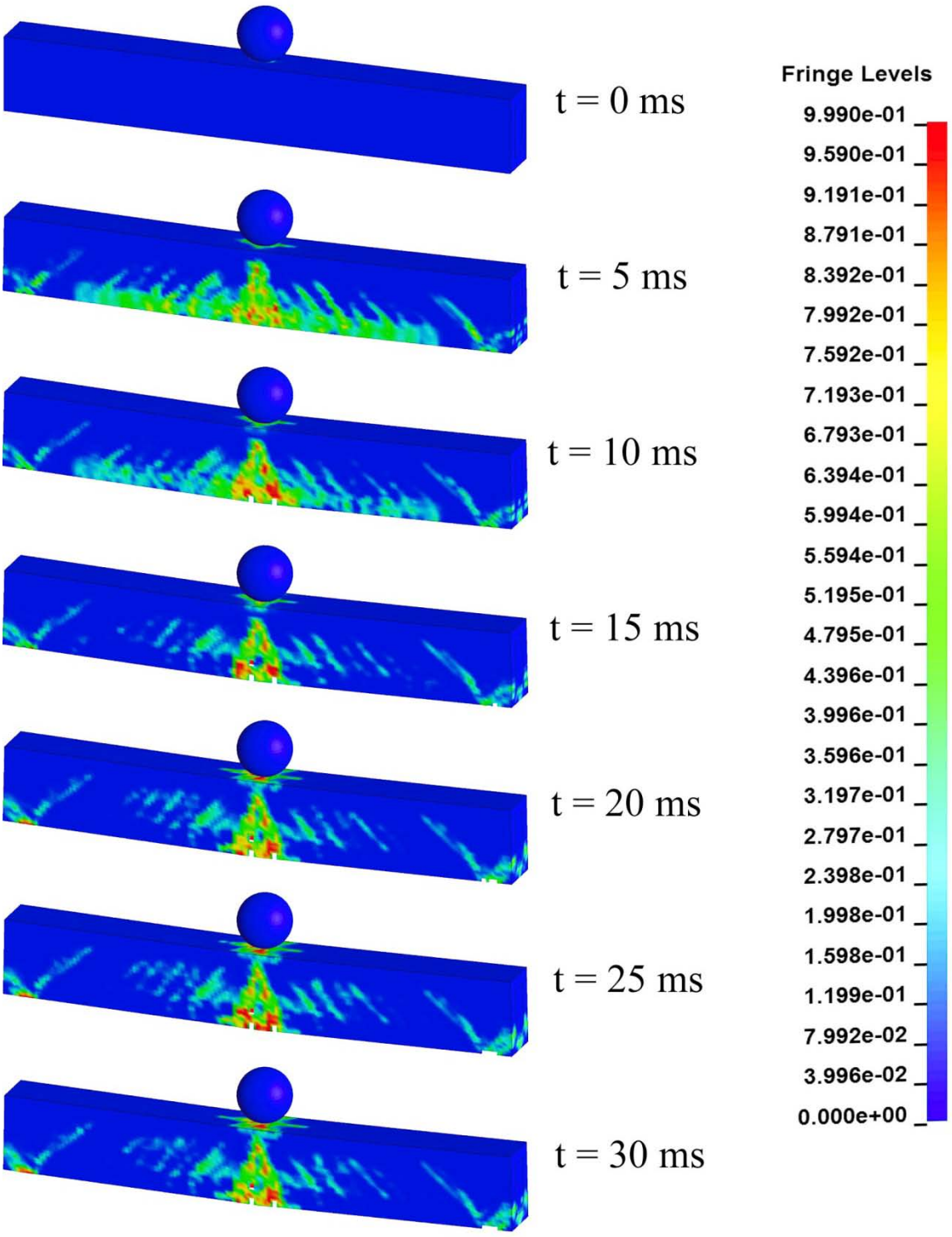

Figure 3.22 Snapshots of 0.6 m drop hammer impacting CSCM concrete beam with medium mesh size. Fringe shows plastic strain distribution in concrete

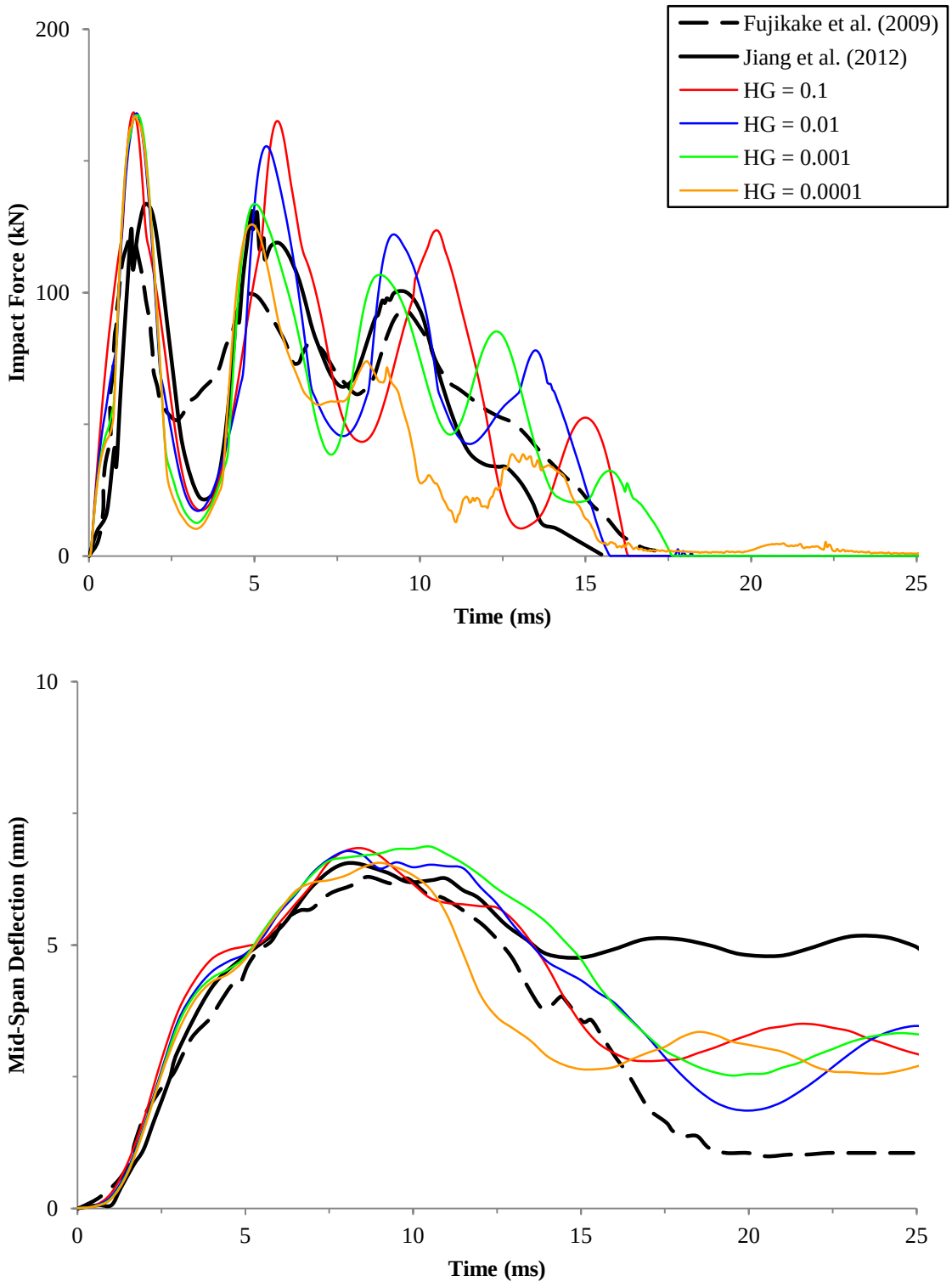

Figure 3.23 Impact force (above) and deflection (below) of RC beam; KC concrete, 0.15 m drop height, automatic contact, Malvar designated DIF, and coarse mesh size

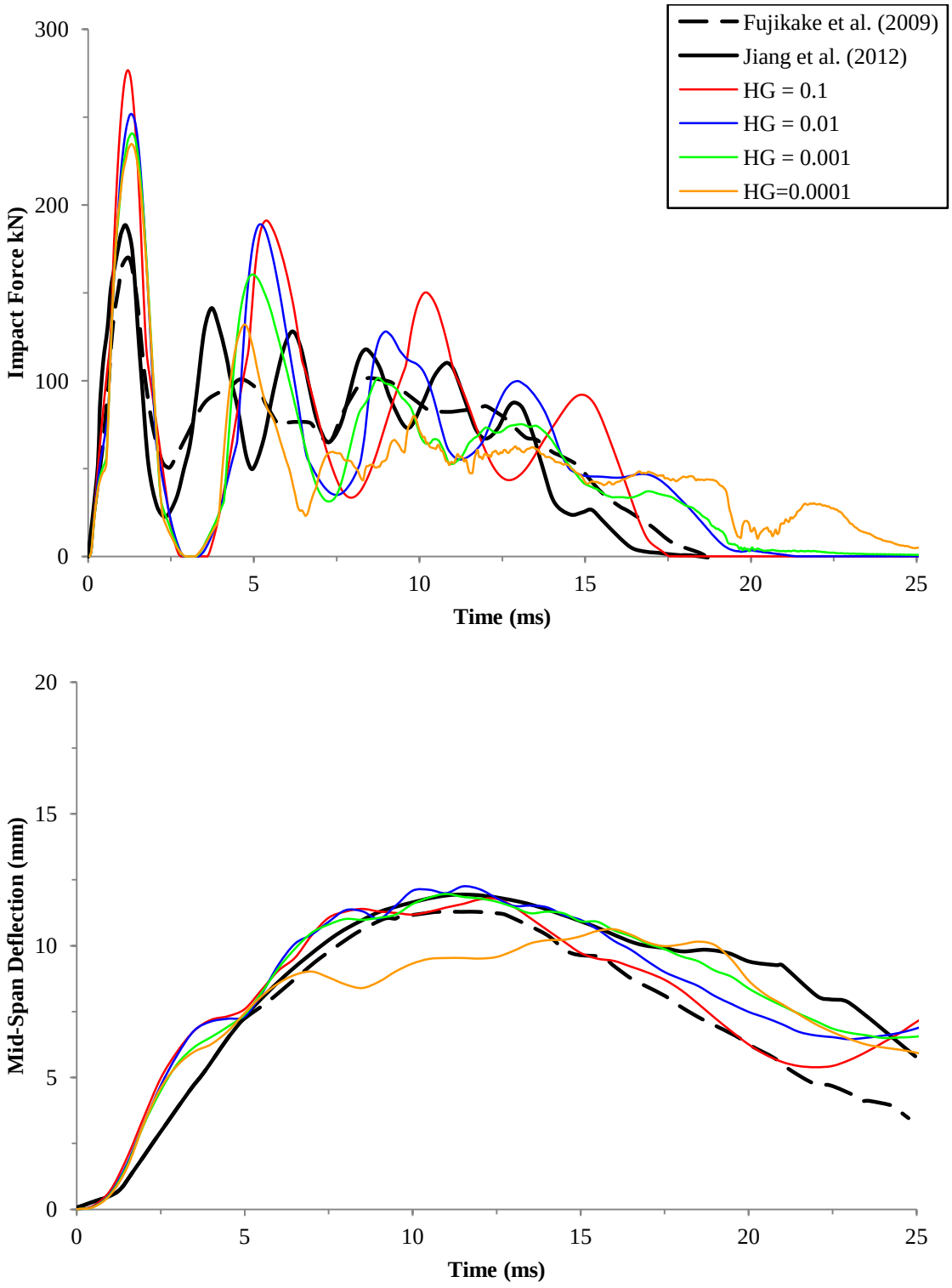

Figure 3.24 Impact force (above) and deflection (below) of RC beam; KC concrete, 0.3 m drop height, automatic contact, Malvar designated DIF, and coarse mesh size

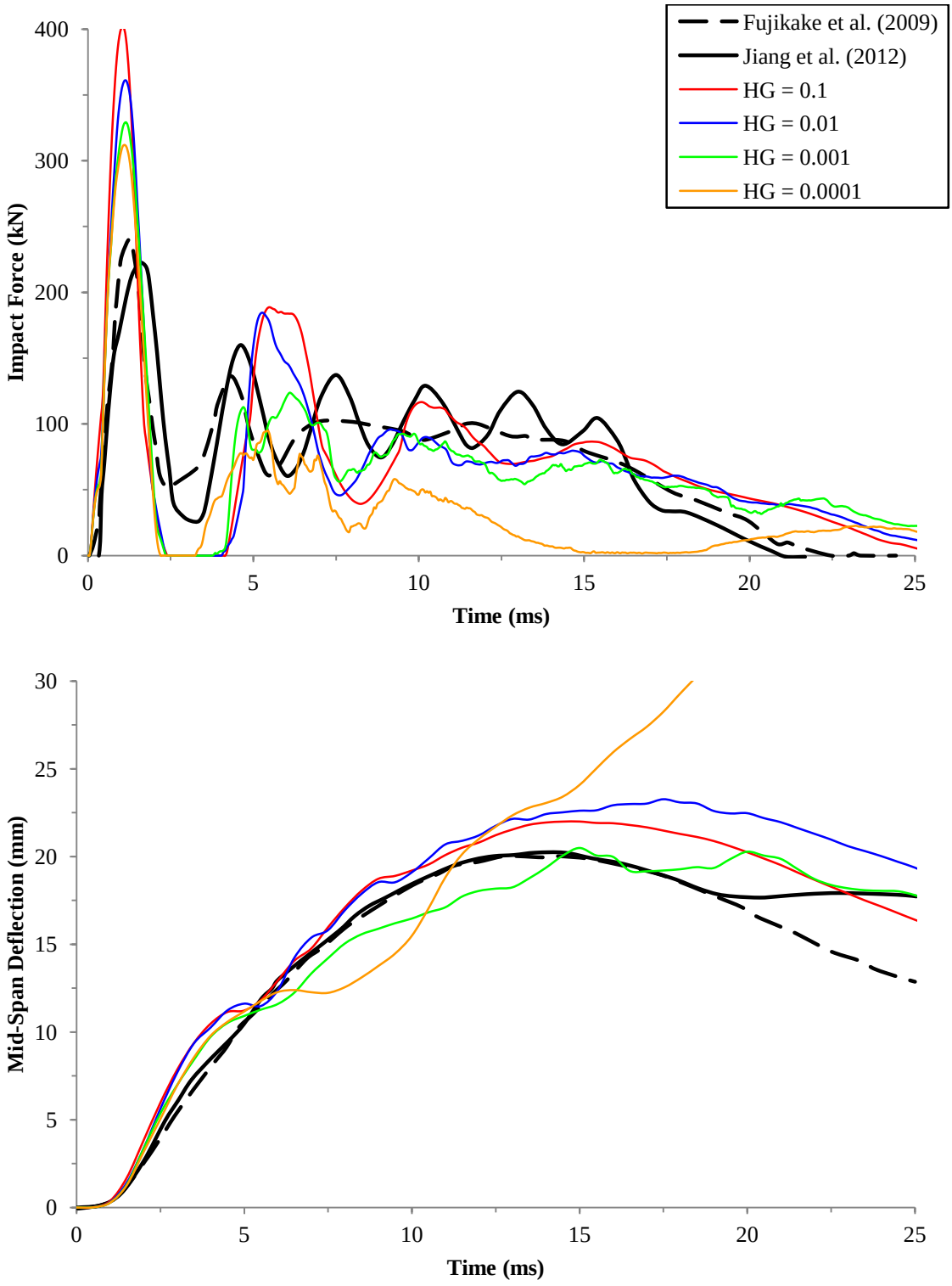

Figure 3.25 Impact force (above) and deflection (below) of RC beam; KC concrete, 0.6 m drop height, automatic contact, Malvar designated DIF, and coarse mesh size

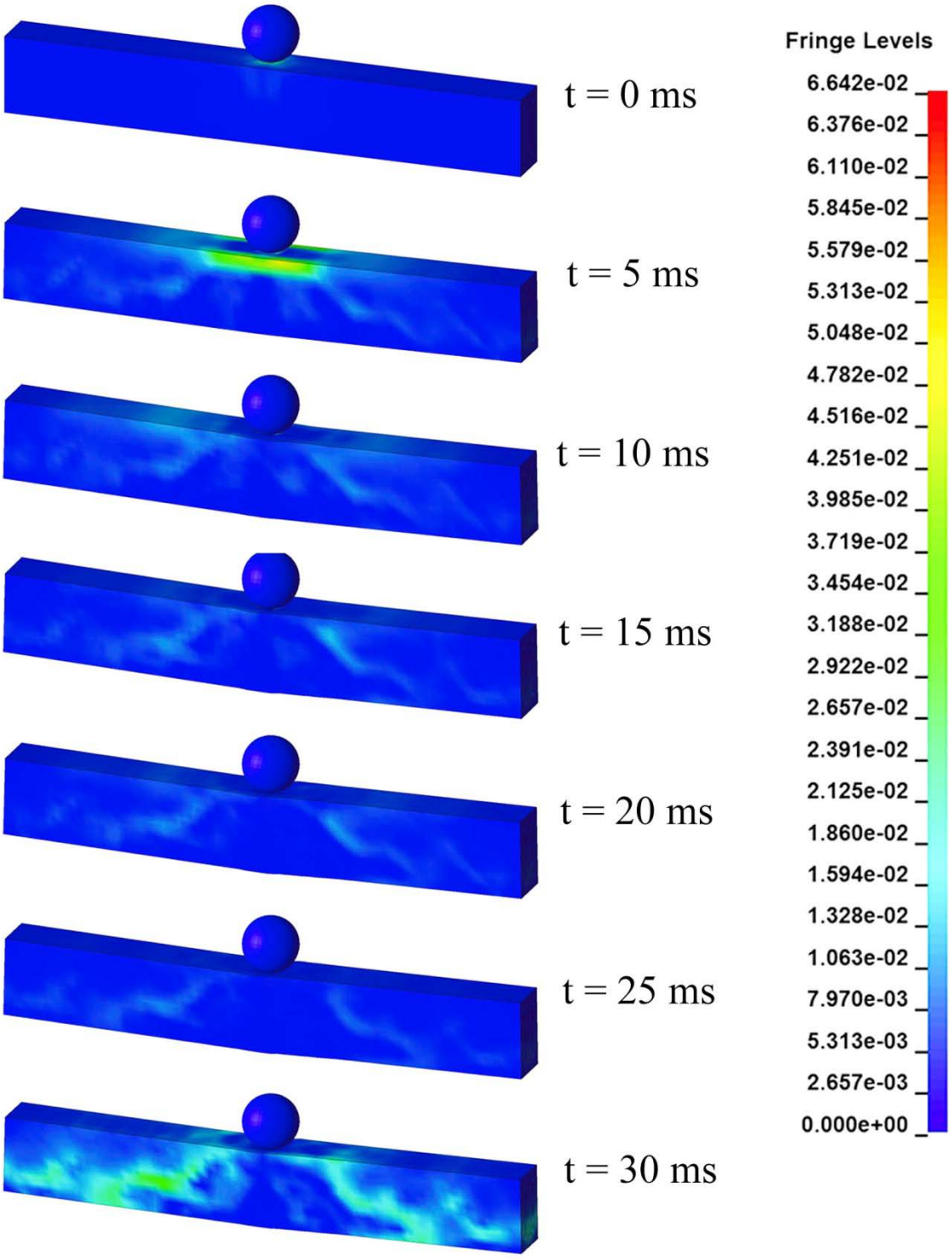

Figure 3.26 Snapshots of 0.6 m drop hammer impacting KC concrete beam with medium mesh size. Fringe displays distribution of von Mises stress in concrete

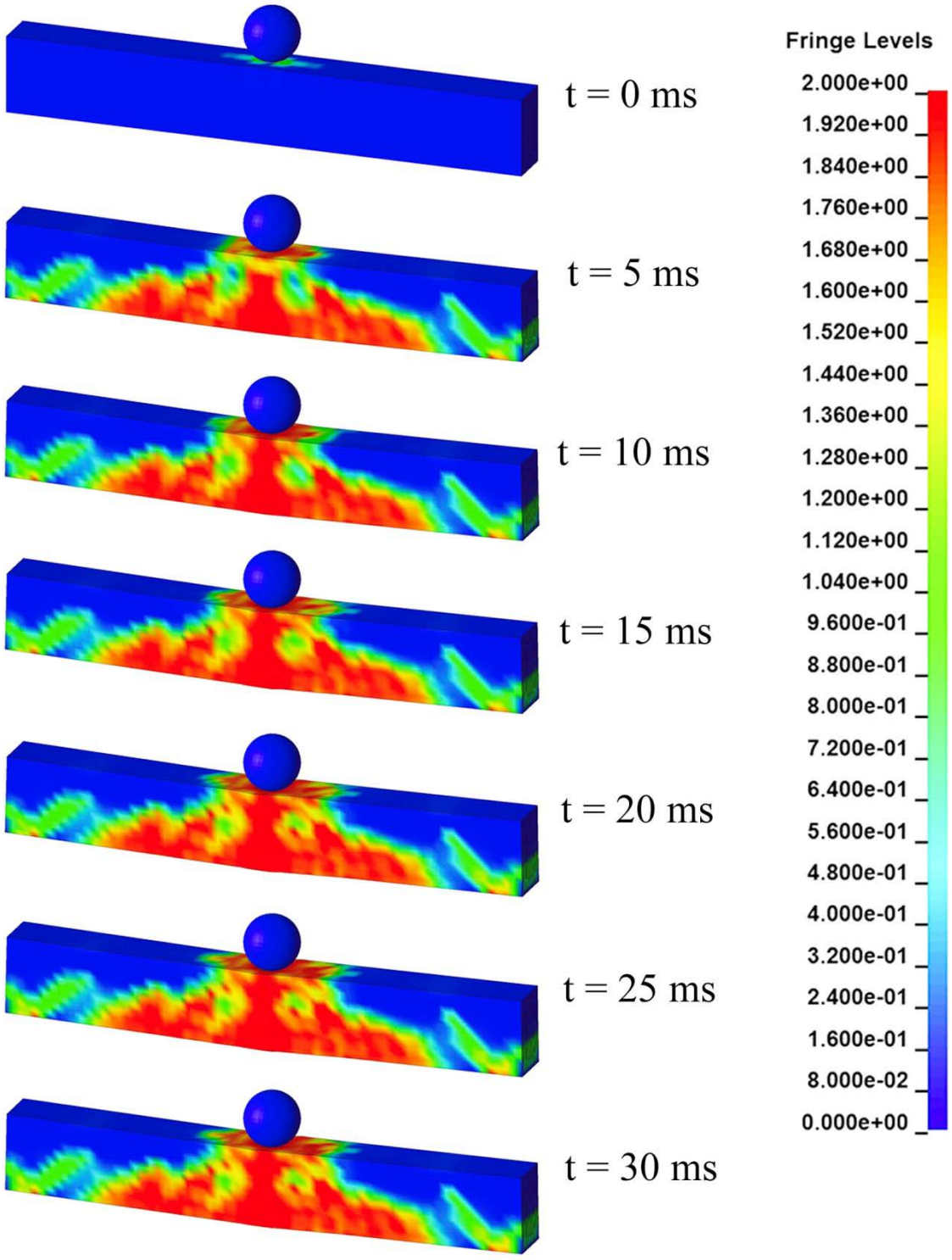

Figure 3.27 Snapshots of 0.6 m drop hammer impacting KC concrete beam with medium mesh size. Fringe shows plastic strain distribution in concrete

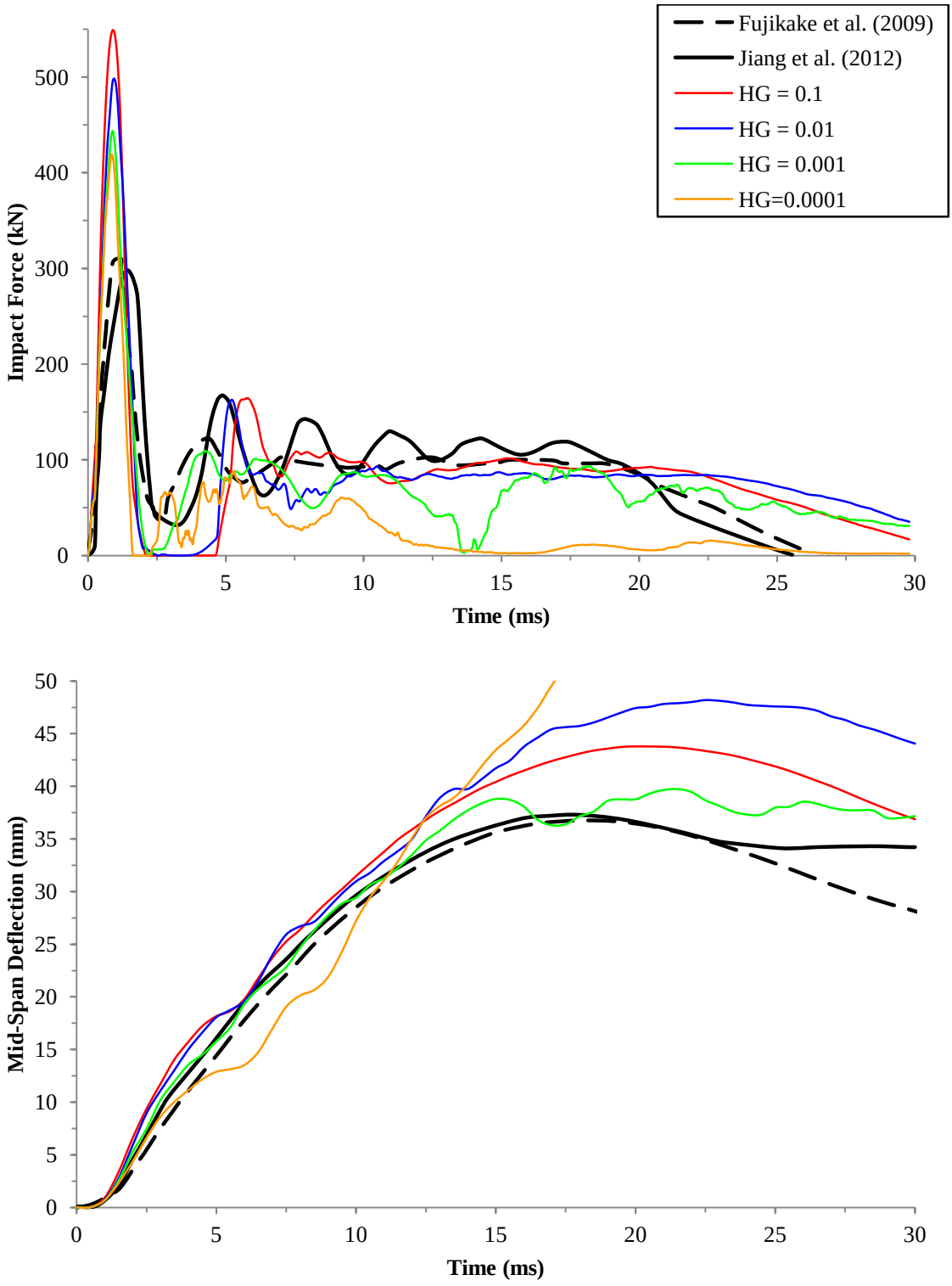

Figure 3.28 Impact force (above) and deflection (below) of RC beam; KC concrete, 1.2 m drop height, automatic contact, Malvar designated DIF, and coarse mesh size

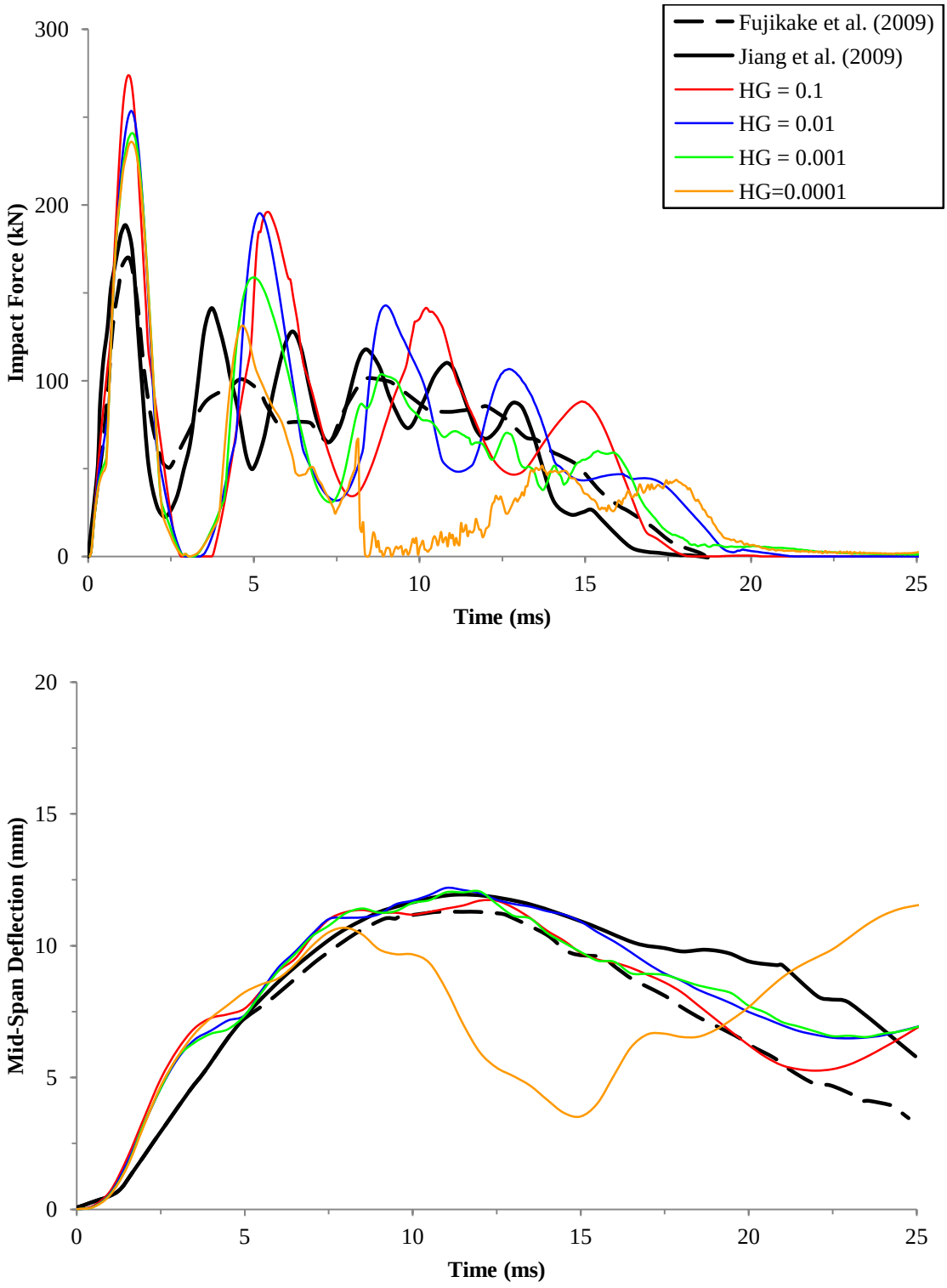

Figure 3.29 Impact force (above) and deflection (below) of RC beam; KC concrete, 0.3 m drop height, eroding contact, Malvar designated DIF, and coarse mesh size

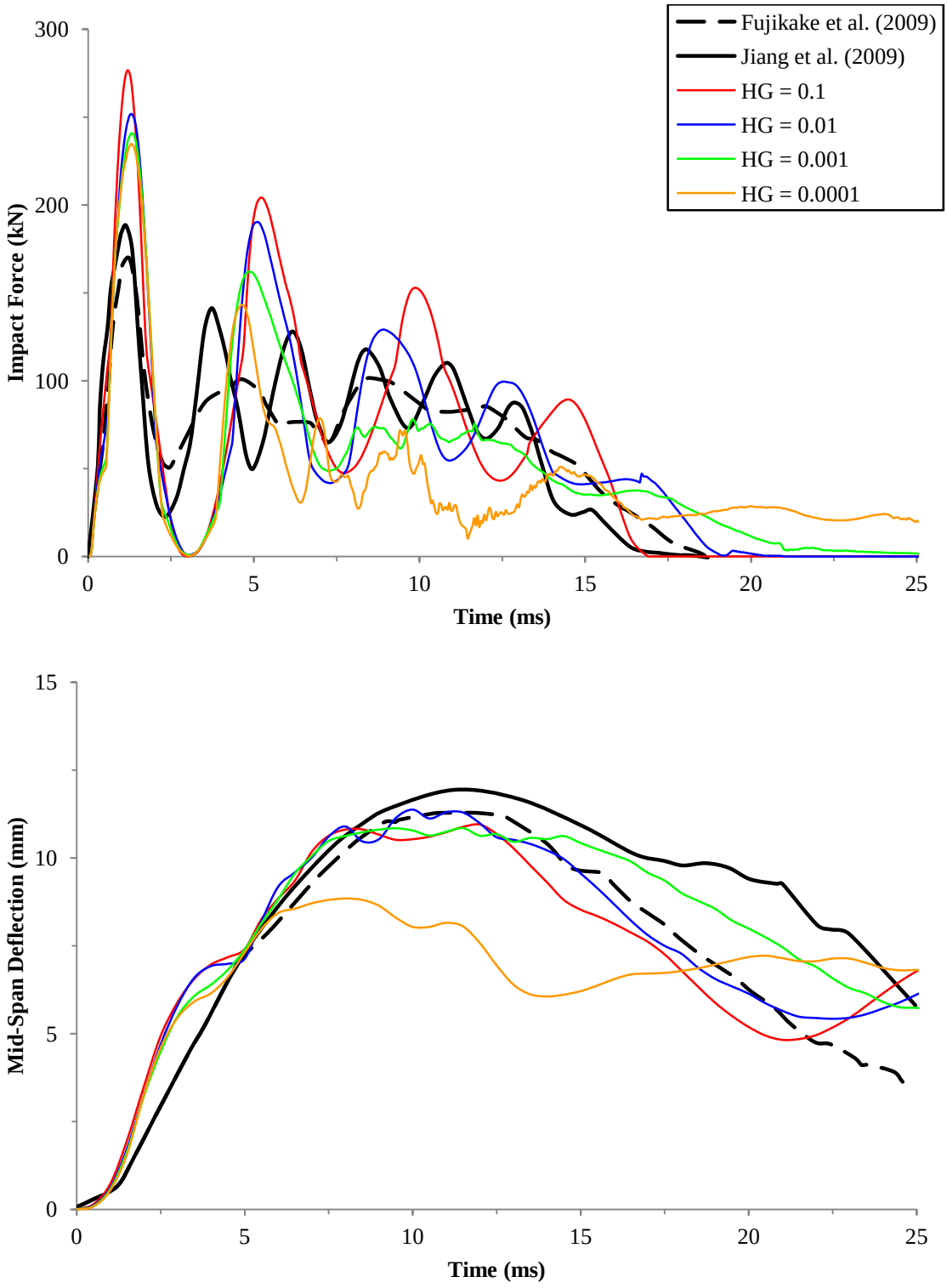

Figure 3.30 Impact force (above) and deflection (below) of RC beam; KC concrete, 0.3 m drop height, automatic contact, DOT designated steel DIF, and coarse mesh size

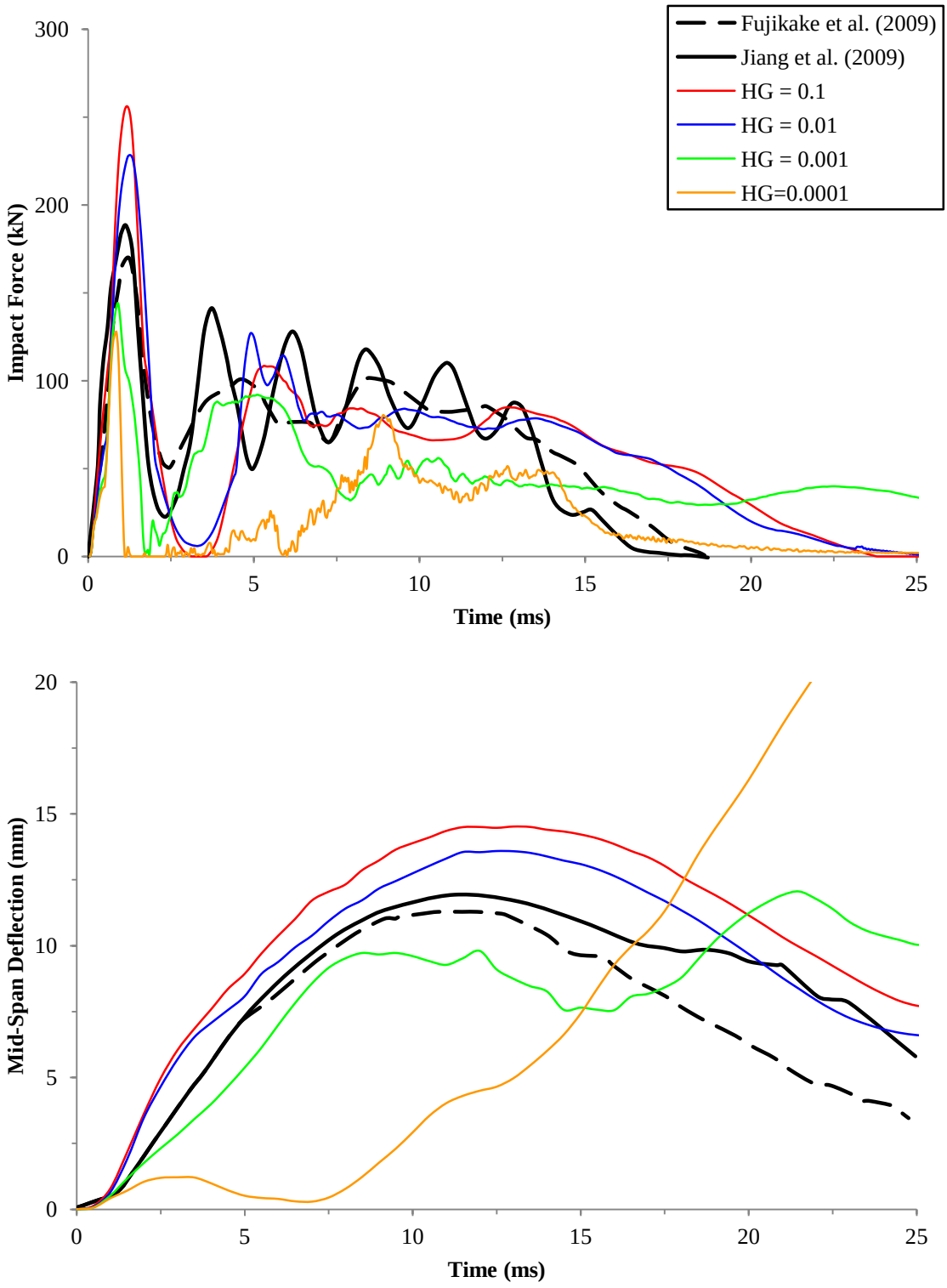

Figure 3.31 Impact force (above) and deflection (below) of RC beam; KC concrete, 0.3 m drop height, automatic contact, DOT designated DIF for concrete, and coarse mesh size

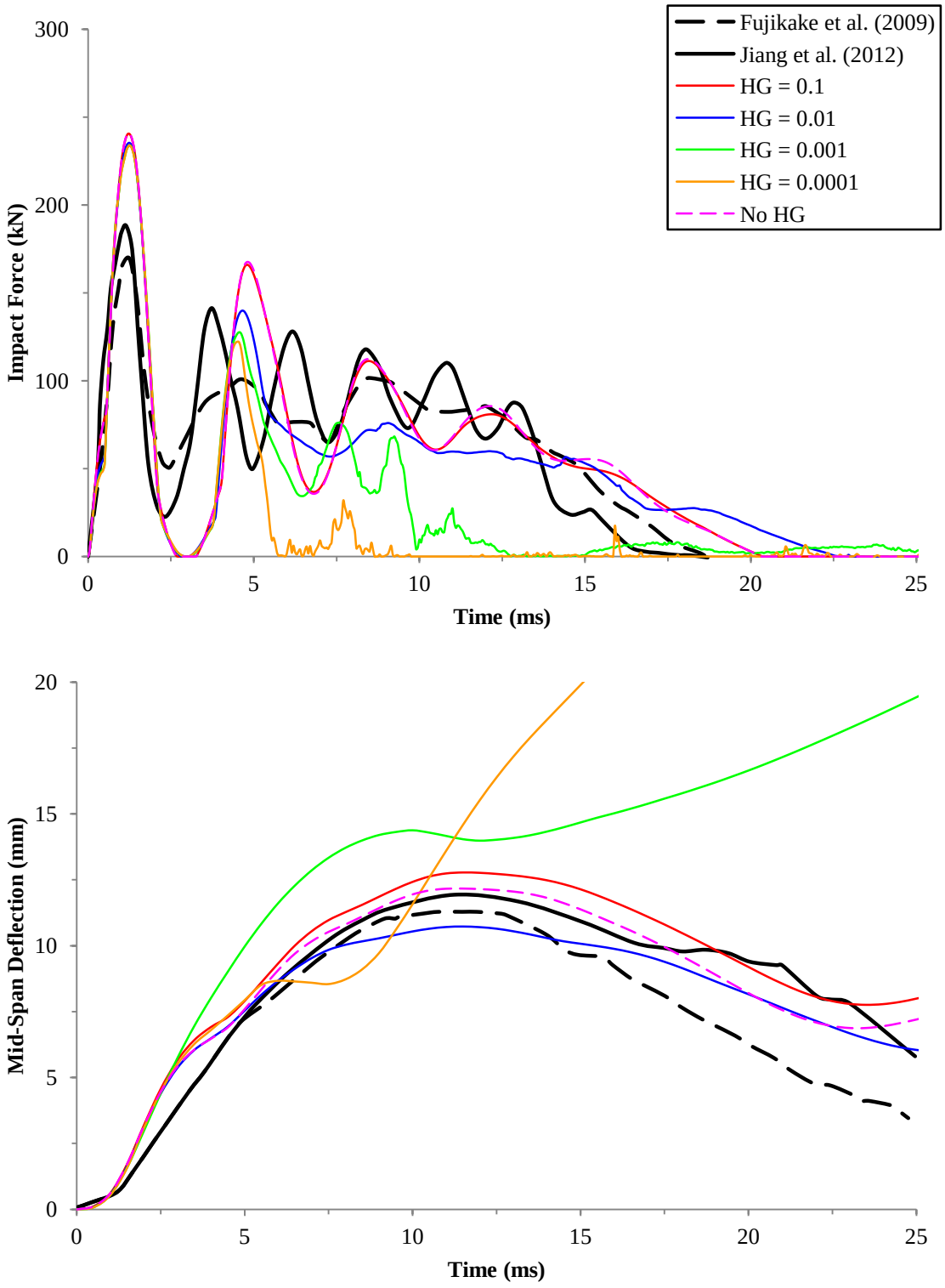

Figure 3.32 Impact force (above) and deflection (below) of RC beam; KC concrete, 0.3 m drop height, automatic contact, Malvar designated DIF, viscous HG, and coarse mesh size

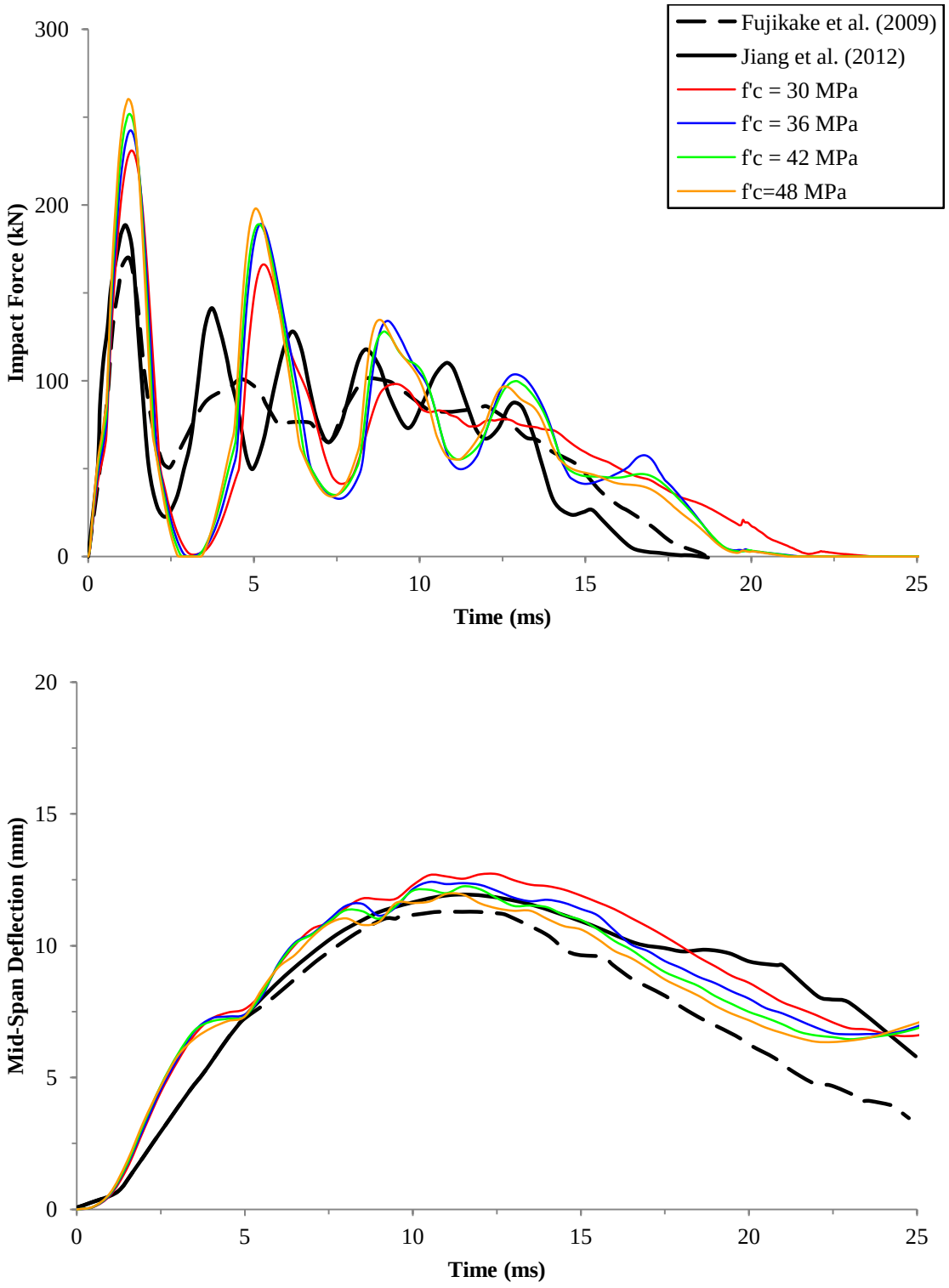

Figure 3.33 Impact force (above) and deflection (below) of RC beam; KC concrete, 0.3 m drop height, automatic contact, Malvar designated DIF, HG = 0.01, and coarse mesh size

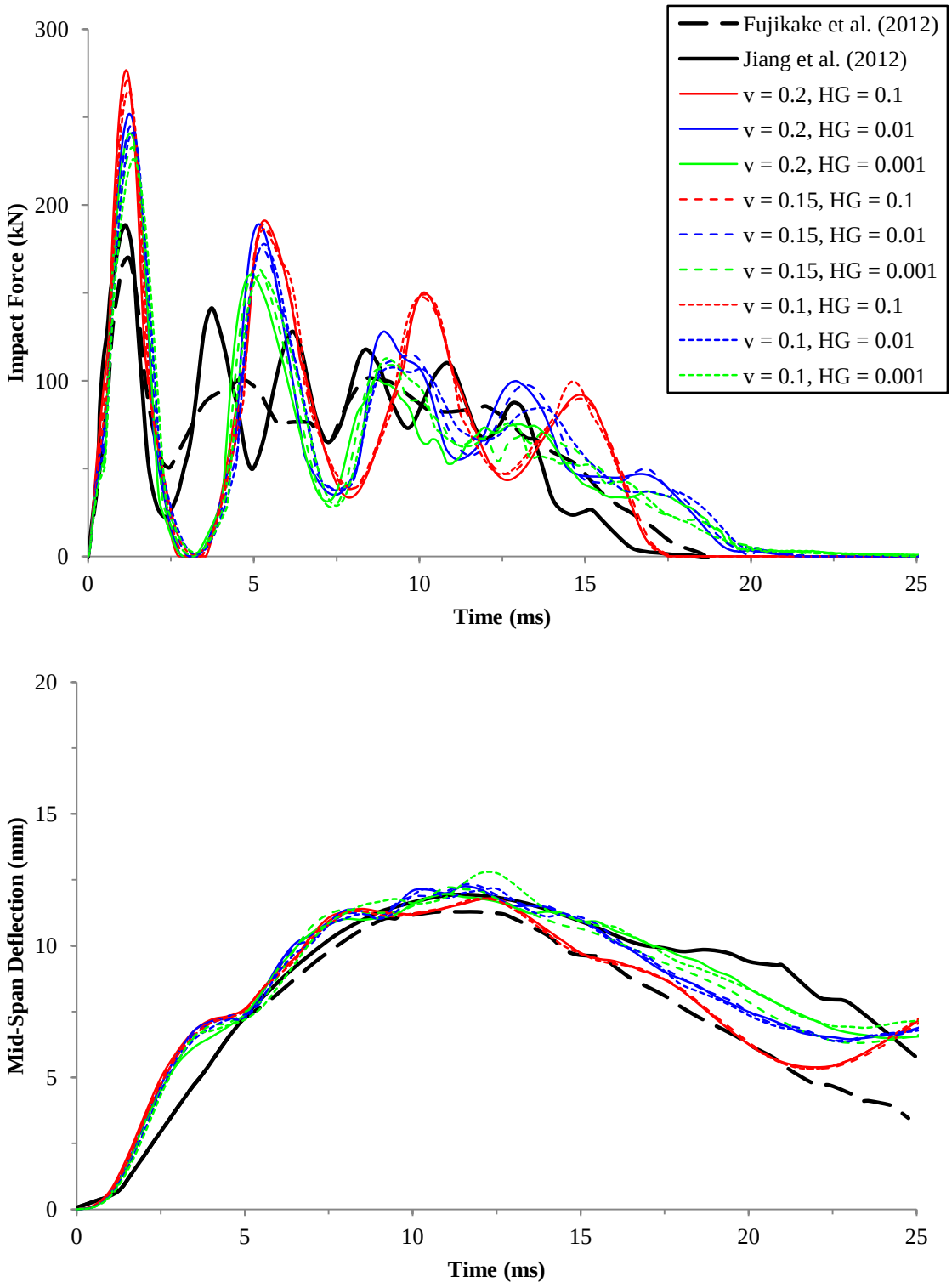

Figure 3.34 Impact force (above) and deflection (below) of RC beam; KC concrete, 0.3 m drop height, automatic contact, Malvar designated DIF, various Poisson's ratios, and coarse mesh size

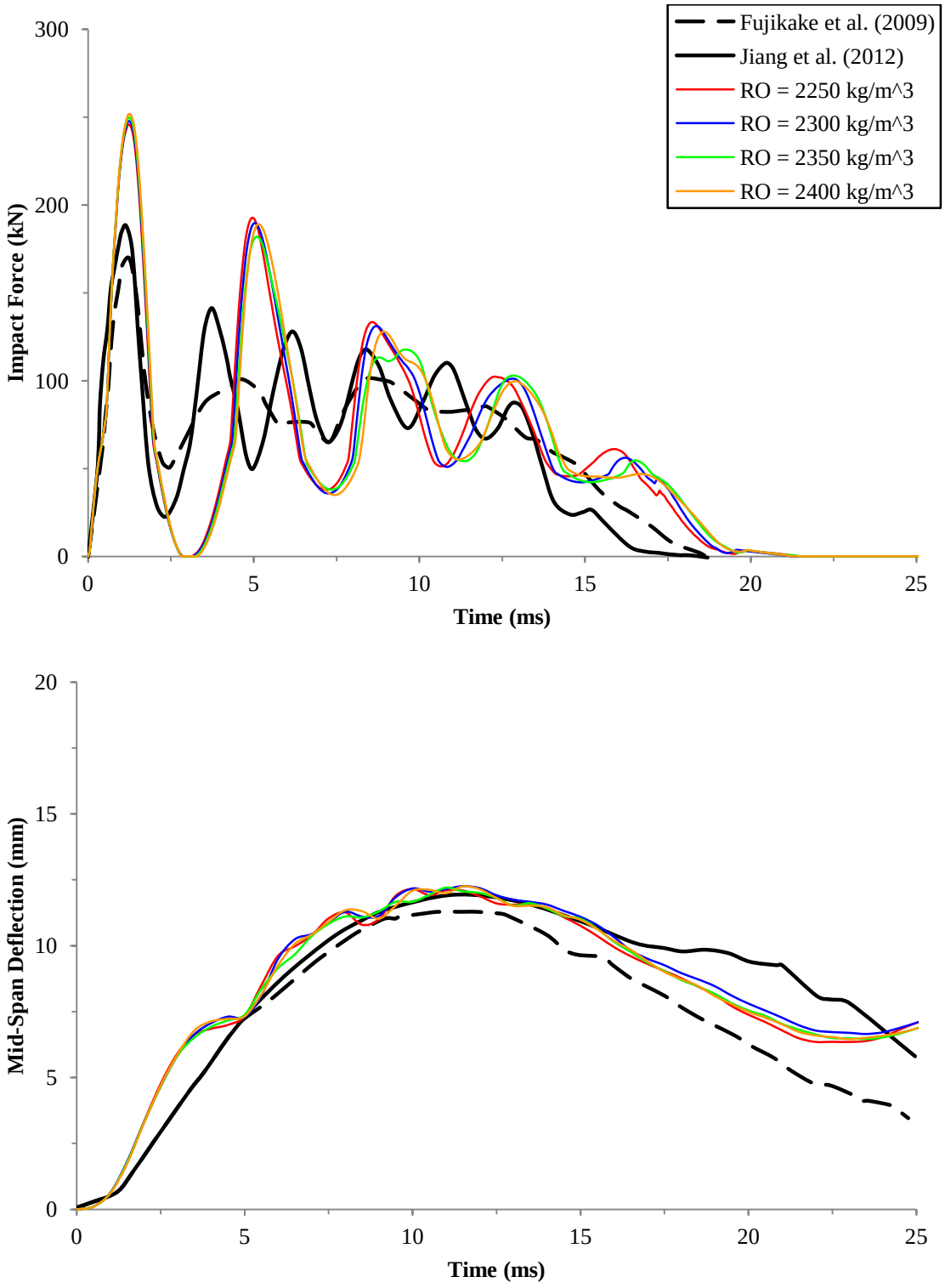

Figure 3.35 Impact force (above) and deflection (below) of RC beam; KC concrete, 0.3 m drop height, automatic contact, Malvar designated DIF, HG = 0.01, and coarse mesh size

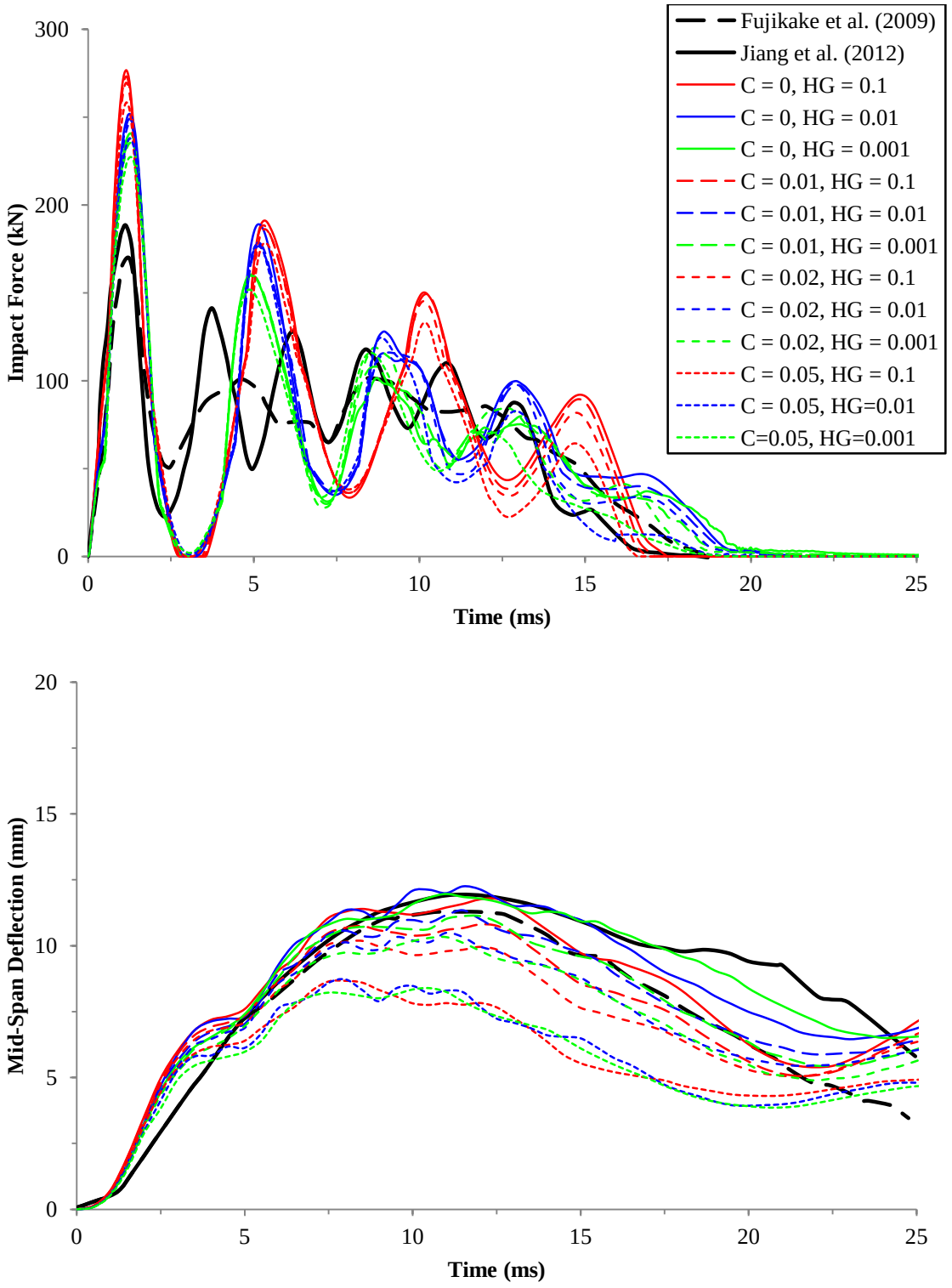

Figure 3.36 Impact force (above) and deflection (below) of RC beam; KC concrete, 0.3 m drop height, automatic contact, Malvar designated DIF, GLOBAL damping, and coarse mesh size

CHAPTER 4

BARGE − BRIDGE PIER IMPACT

The threat of impact from vessel is one of the largest considerations for bridge design in navigable waterways. A barge-bridge collision can be a highly significant event, due to the high mass that a barge could be carrying, and the water height needed to float a barge. Barges have a greater frequency of impact than ships due to the increase of waterways with bridge crossings that are navigable by barges. Barges are relatively shallow draft vessels, whereas ships have deeper draft limitations. A vessel's draft is defined by the lowest point of the vessel hull to the water line. Draft limits can be as shallow as 2 ft., allowing navigation in shallow water depths where ship navigation would not be possible. Despite this fact, up until recently, the majority of research has been focused on ships rather than barges. In addition to the shallow draft requirements, barges are highly massive structures, resulting in highly dynamic impact forces.

Because bridge design is often controlled by impact loading, there is a need to interpret and understand the mechanics of barge collision. The previous chapter discussed the mechanics and response of the reinforced concrete structures subject to impact loads. The current chapter focuses on the mechanics of the barge collision, in particular the crushing behavior of the barge. For this purpose, the details required for the model to capture the crushing of the barge using nonlinear FE analysis are provided. The geometry of the barge should be simplified for efficiency, but appropriate to develop accurate results. Dynamic impact analyses will be employed to approach acceptable barge stiffness. Additionally, a sensitivity analysis will be conducted to understand how barge responds to various impacts. This preliminary investigation was modeled after

Yuan (2005). Other references are used to guide assumptions in geometry setup, material models and initial conditions.

4.1 Barge Modeling

The Jumbo Hopper (JH) Barge was selected for this study. The JH is the baseline fo AASHTO crush depth fumulas thereby allowing for direct comparison to the emperical calcualtions presented in the *AASHTO Guide Specifications and Commentary for Vessel Collision Design of Highway Bridges.*

4.1.1 Geometry

In cooperation with the goal of this work, a well-defined model of the barge is developed to ensure acceptable deformations and impact forces from the barge. Although the behavior of the barge is not a focus of this work, proper representation is required to account for energy absorption through plastic deformations in the barge. JHs are fabricated with steel plate hulls varying in thickness and several structural steel members connected using welded construction. The representative JH model selected for the current study measures 195×35×12 ft. Since head-on collisions are studied within this work, greater details are modeled in the front region of the barge. A basic schematic of a JH barge is shown in Figure 4.1 with the front region (bow) shaded in grey.

The modeled portion of the barge was developed with moderately high mesh resolution, with particular focus on the bow region. The hopper region is idealized by large elastic solid elements, whereas it is important that the bow is modeled with particular detail. Taking the time to set up an accurate geometry initially will save time and produce more dependable results. The hull, the watertight outer most skin-like structure of a ship, is represented by shell elements and the internal bow trusses are built

of beam elements with appropriate cross section properties. There are a total of 14 trusses in the bow with two transverse members; an angle section at the very front of the bow and a channel section about halfway into the depth of the bow (Figure 4.2). The trusses are symmetric about the center line of the barge. The first truss is one foot from the centerline. Then 6 more are spaced 2' 2" apart, leaving a 3'6" spacing from the most exterior truss to the side hull plates. Considering that the sections used in the truss are not axisymmetric sections, the orientations of the beam sections were adjusted so that the trusses on the port side were reflections of the starboard side trusses. This orientation is highlighted in Figure 4.3, showing only two trusses one on either side of the centerline. Attention to offset the internal trusses (beam elements) from the hull plate (shell elements) was taken to avoid initial penetrations and account for the cross section dimensions. This detail is particularly important for the contact between the beam and shell elements. A contact surface will be defined by a cylinder for beam elements. The cylindrical surface is defined by the equivalent radius of the beam cross-section. For shell elements, the contact surface is defined as a surface offset half the thickness on either side of the shell, whereas the geometric plane defined is the mid-surface plane.

Internal beams were constrained to the hull shell using several spotwelds at each truss. Figure 4.4 illustrates the construction drawing dimensions with the overlay of the proposed model barge section at one of the truss locations. Beam section dimensions as well as hull plate thicknesses are the same as detailed in the provided construction drawings. To include this in LS-DYNA, a separate integration rule for the beam section is needed to adjust for the corresponding section. Figure 4.6 and Table 4.1 show the properties needed to define the beam section integration rule. $D1$, $D2$, $D3$, and $D4$ are the

dimensions used to define the cross section. A_c is the cross-sectional area, A_{st} is the gross area of the dimensions in the *s* and *t* local axes ($D1 \times D3$), and R_A is the relative area defined by the ratio of the cross sectional area and the gross area.

Typical A36 steel properties were defined using the piecewise material model for the bow. As large deformations may occur during an impact it is important that the material model is capable of capturing sufficient nonlinear behavior. The true (Cauchy) stress versus true (logarithmic) strain relationship depicted in Figure 4.7 contains enough detail to capture the nonlinearity and failure of the steel material. The original data has been obtained from standard 18-in coupon tests conducted at the University of Florida (Consolazio et al., 2002), but is also used in the development of barge models by other research groups, e.g., (Yuan & Harik, 2010) and Consolazio et al. (2009). Sha & Hao (2012, 2013) however did not use this steel model.

The hopper region utilizes the elastic material model for steel with adjusted density to result in the desired barge mass. If desired, the mass could further be refined by adding nodal mass to a node at the rear of the elastic block along the centerline. The density of the elastic material was determined as such:

$$\rho_{hopper} = \frac{M_{barge} - M_{bow}}{V_{hopper}} \qquad \text{Equation 4.1}$$

where ρ_{hopper} is the density of the hopper, M_{barge} is the total mass of the barge, M_{bow} is the mass of the barge, and V_{hopper} is the volume of the hopper region. Fully loaded barges weight 1900 short tons (1723.7 metric tons) which will typically be used for impacts in this research. An empty barge is 200 short tons (181.4 metric tons). The densities and additional mass for different loading cases are detailed in Table 4.2.

The interaction between internal bow trusses and adjacent bow trusses and trusses with the hull plate is possible, especially in cases of large deformation. To control the interaction of these parts the automatic single surface contact algorithm was used for all parts of the bow. Static and dynamic coefficients of friction were set to 0.2 for steel-steel contact. Initial velocity is set to the nodes of the barge elements in the forward traveling direction. Nodes at the base of the hopper are restricted against motion in the vertical direction.

4.1.2 Elasticity of Barge Impact

The elasticity of the barge is used to evaluate the strength and behavior of the barge model following the methodology proposed by Yuan et al. (2005). The elasticity is a measure of the kinetic energy before and after the collision. As kinetic energy is a function of the traveling velocity of an object, the velocities before and after a collision are often used to measure the elasticity. The coefficient of restitution, *e*, for head-on impacts of a barge and rigid pier can be defined as the ratio of the velocity after a collision, V_{td}, and the initial velocity before impact, V_i:

$$e = \frac{V_{t_d}}{V_i} \qquad \text{Equation 4.2}$$

If a collision were to be perfectly elastic, this ratio would be equal to unity, whereas a perfectly inelastic collision would have a coefficient of zero. The coefficient of restitution cannot be greater than unity as this would imply that the velocity after impact is greater than the initial velocity, which is only possible with an increase in mechanical energy. The coefficient of restitution can be determined by monitoring the average nodal

velocity before and after the impact. Additionally, the impulse momentum law can be used to determine the velocity at any given time, *t,* by the following:

$$V(t) = V_i - \frac{\int_0^t P(t)\,dt}{m_b} \qquad \text{Equation 4.3}$$

substituting this into the equation for restitiution:

$$e = 1 - \frac{\int_0^{t_d} P(t)\,dt}{I_i} \qquad \text{Equation 4.4}$$

where $P(t)$ is the force curve, m_b is the mass of the barge and $I_i = m_b V_i$ is the initial momentum of the barge.

The ratio of the barge to pier width, α, varies the contact area during the collision. For flat faced piers, the wider pier the greater the number of bow trusses that are directly engaged in resisting the initial impact. For the special case of α =1.0 (or greater) the entire bow is resisting the impact. For circular piers the two center trusses are always the first to resist the impact initially, until enough deformation occurs to allow contact with the next outward adjacent trusses. This behavior was also observed in the literature (Consolazio & Cowan, 2003). Numerous impact simulations were conducted with the barge on circular and flat faced rigid piers to determine the coefficient of restitution for the impact. Automatic surface to surface contact is defined between the barge and the pier with friction coefficients defined as 0.3. In all these cases the pier is assumed to be rigid and fixed against all degrees of freedom. Although a rigid material model, properties of reinforced concrete are defined to ensure appropriate contact behavior.

As the elasticity is based on the initial kinetic energy and the energy absorbed by the impact, namely deformation and also friction, a range of barge masses, impact

velocities, and pier sizes were studied. Five velocities (0.5, 1, 2, 3, and 4 m/s) four loading conditions (fully, half, quarter, and empty loaded) and six barge-pier ratios (0.1, 0.3, 0.5, 0.7, 0.9, and 1.0) resulting in 120 different cases for each pier shape were developed to populate Table 4.3 and Table 4.4. The barge damage depth and the resultant impact force were collected for each simulation. Both previously discussed methods for determining the coefficient of restitution were observed for any case. A less than 10%, often around 5% error, was found when comparing the calculated impulse method and the reported nodal velocity. Although small, this is attributed to error in integration due to sampling frequency and noise in the impact force plot, which is minimized through increasing the sampling rate.

Using a similar regression proposed by Yuan (2008), the forming regression formulas can be used to estimate the coefficient of restitution in terms of the pier to barge width ratio, α, and the initial kinetic energy, E_i.

For square piers with $0.05 \le \alpha \le 1.0$:

$$e = 0.2501 + 0.0323\,\alpha - (0.0739 + 0.0153\,\alpha)\ln E_i \qquad \text{Equation 4.5}$$

where the restitution of a barge for circular shaped piers can be expressed as:

$$e = 0.0574 + 0.0725\,\alpha - (0.1244 + 0.0164\,\alpha)\ln E_i \quad \text{for} \quad E_i > 0.105 \qquad \text{Equation 4.6}$$

$$e = 0.2913 - 0.0035\,\alpha - (0.00239 + 0.0285\,\alpha)\,ln\,E_i \quad \text{for} \quad E_i > 0.105 \qquad \text{Equation 4.7}$$

4.1.3 Pier Size and Shape

Bridge piers are often designed with a predominately square or circular cross section. The size and shape of a pier are crucial design considerations for bridge design

and protective structures for piers. The Woodrow Wilson Memorial Bridge in Washington, D.C., reconstructed in 2008 with large V-shaped piers and square cross sections. At the bascule span there are large protective structures on the water so that the pier cannot be struck by a passing vessel. On the other hand, the replacement for the Sunshine Skyway Bridge in Florida included round piers and protective structures around the tower piers (Figure 4.8). Consolazio (2003) and Yuan (2008) have reported significant differences in barge-pier impact forces due to geometry. However, the AASHTO Specification does not recognize impact force design to be dependent on pier geometry.

Figure 4.9 displays the time histories for barge crush depth and impact force. In these cases a fully loaded barge traveling at 1.8 m/s (3.5 knots) impact a rigid square pier. This is the velocity that Yuan (2008) uses to draw conclusions about his barge model. The only variable is the pier size, where the pier to barge width ratio, α, is changed. It is clear from the figure that the peak impact force is highly dependent on α. With larger pier widths, higher peak forces should be expected, but also decreased crush depths and impact times were observed. Larger piers produce larger contact surfaces, which contribute to larger contact forces. The larger contact surface engages more internal trusses in the contact. The flat contact surface, normal to the direction of motion, requires that all the trusses engaged in the collision resist the force simultaneously.

A summary of the time histories from the previous figure is outlined in Table 4.5. The parameters chosen are those that Yuan (2008) employed for the numerical analysis, where P_{max} is the maximum impact force, $\overline{P}_{1/2}$ is the average impact force for the first quarter of the impact duration (t_d), and $\overline{P}$ is the average impact force. The barge model

in this research typically results in a greater impact force for complementary simulations in Yuan et al. (2008). Additionally, the duration of the impact and barge crush depth results are about half of Yuan et al. (2008). However, the trends between the different α are similar.

The behavior of circular piers is also investigated. Figure 4.10 and Figure 4.11 show the time histories of fully loaded barges impacting rigid circular piers at two different impact velocities, 1.54 m/s (3.0 knots) and 2.57 m/s (5.0 knots), respectively. The behavior of the barge does not follow the trends of the Yuan et al. (2008) findings, however there is evident that the impact force behavior more closely follows the results from the other literature (Consolazio & Cowan, 2003). In their report, they describe the impact forces to "gradually and monotonically increase with corresponding increases in crush depth" in circular pier simulations. This behavior can also be concluded through the impact force time history plots. Table 4.6 and Table 4.7 summarize these time histories like previously done with square piers.

As previously mentioned, the AASHTO Specifications specifies design impact loads independent of the pier geometry. However the results show that the size and shape of the pier can be highly influential on the impact force. The simulations used to populate the restitution tables are used to compare the initial kinetic energy of the barge and the barge crush depth (Figure 4.12). The formulation in the AASHTO Specifications was also included. AASHTO formulation bounds all the simulation results. However, it can highly over predict the crush depth for many of the square piers. The peak $\left(P_{max}\right)$ and average $\left(\overline{P}\right)$ forces for the 1.8 m/s barge impacting square piers as well as the 1.54 m/s and 2.57 m/s barge impacting circular piers are plotted along with the predicted

AASHTO design force for each case, 7.12 MN, 6.8 MN, and 8.11 MN, respectively (Figure 4.13 through Figure 4.15).

4.2 Pier Impact Simulations

Up to this point, a detailed model of a simply supported beam impacted by a rigid impactor was studied with the primary focus on assessing the material models and structural response. On the other hand, an extensive investigation on the impactor, i.e., a jumbo hopper barge, was conducted to simulate the expected demand through impacts into rigid target columns. In an actual impact however both the reinforced concrete pier and the barge can behave nonlinearly. Now that both have been assessed and calibrated separately, a set of barge collision simulations are performed.

Piers support valuable structures that form an obstruction in the waterway. Not only are highway bridges safely carrying motorists, but they also act as main arteries for the freight economy. In most cases, bridges over navigable waterways have substructures that must impede the waterway. Reinforced concrete piers can carry the massive dead and live loads that are transferred through the bridge superstructure. Piers, as with any other obstruction, are susceptible to impact by passing vessels. Damage of the substructure from vessel impact will undoubtedly lead to closure of the bridge. In the worst case of a catastrophic failure of a pier, adjacent spans can no longer be supported and fall, as in the Oklahoma case reported in the introduction of this thesis.

To understand the performance of bridge piers over waterways against the barge collision, five different pier geometries will be examined in this section. For each pier geometry, five models alternating superstructure mass and barge velocity are considered. The three tributary superstructure masses considered are 150, 300, and 600 metric tons.

The superstructure mass can be reflective of the size of the bridge or the length of the mid-span that a pier may have to support. All piers are assessed under an impact induced by a fully loaded (1723.7 metric tons) barge with an impact velocity of 2 m/s (3.88 knots), however the 300 ton pier is also investigated with a fully loaded barge traveling at 1 m/s (1.94 knots) and 4 m/s (7.78 knots). As the concentrated mass induced by the superstructure increases, the ratio of the column mass/superstructure mass decreases, making the structural system similar to a typical SDOF structure. Different impact velocity initiates different initial kinetic energy, which is one of the large contributors to the impact force induced from an object. In all simulations the top of each pier contains no boundary conditions. The pier has also been pre-loaded for self-weight using multi-phase dynamic relaxation discussed in a previous section.

In this section two cross sectional geometries are considered, square and circular, elsewise the piers are similar. The piers are fixed in all degrees of freedom at the base nodes. For both the square and circular section, the results will be presented with an in-depth discussion of the baseline condition. That is the fully loaded barge travelling at 2 m/s impacting a pier with the supported mass of 300 tons. After the baseline has been discussed, the results from the other cases will be summarized and conclusions will be made between the several cases.

4.2.1 Materials

The concrete in the pier is assumed to be normal weight, 40 MPa concrete with maximum aggregate size of 10 mm. The CSCM model was assumed for all the concrete used in the model. The top one meter in each model is used to assign superstructure mass,

therefore the density of this section is not of that of normal weight concrete. In addition, the concrete erosion criterion is not applied.

Steel Reinforcement is modeled with a bilinear stress strain curve similar to the beam models in a prior section. Strain rate effects are included into the material model using the tabulated DIFs derived by the Malvar/CEB formulation. In simulations where piles are included, the piles are assigned the same material model used for the barge bow.

4.2.2 Geometry

For this study a square pier will be analyzed only for the fixed base condition. However, the circular pier has 4 different geometric iterations. This section will discuss the details of these various piers.

4.2.2.1 Fixed Square Pier

A pier with a square cross section, partially adopted from the geometry presented by Sha and Hao (2012), measures 3.2 m in its cross section, with a cover of 100 mm on all sides (Figure 4.16). D30 (Ø = 30 mm) longitudinal reinforcement bars span continuously through the top mass, the pier column, and the foundation, while D20 (Ø = 20 mm) are used for the transverse reinforcement. Longitudinal bars are spaced at 30 mm on all four sides and the transvers reinforcements are spaced at 20 mm through the length of the column. The section's ratio of longitudinal reinforcement to the gross section (A_s/A_g) is 0.00276. The mesh is defined such that beam and solid elements share common nodes. This modeling strategy assumes perfectly bonded condition between the concrete and reinforcement steel. At the base, there is a 3.0 m thick mat foundation measuring 9.8×9.8 m^2. Half a meter from the base there is a mesh of mat reinforcement with D40 bars. In total the square pier is comprised of about 28,500 elements.

Additional views of the meshed pier with a square cross section can be seen in Figure 4.17. With a 3.2 m cross sectional dimension of the pier, the pier to barge with ratio, α, is 0.3.

4.2.2.2 Fixed Circular Pier

In a similar fashion, a 3.2 m diameter circular pier is introduced with a cover of 100 mm (Figure 4.18). The longitudinal rebar arrangement was selected to maintain the same approximate spacing as well as the same steel ratio. As a result, 32 D30 (Ø = 30 mm) longitudinal bars are evenly spaced. Hoops are D20 bars (Ø = 20 mm) spaced at 20 mm through the length of the column. The longitudinal reinforcement arrangement provides a steel ratio (A_s/A_g) of 0.00281. The D30 longitudinal bars span continuously through the top mass, the pier column, and the foundation. The mesh is defined such that beam and solid elements share common nodes. At the base, there is a 3.0 m thick mat foundation measuring 10.0 × 10.0 m^2. Half a meter from the base there is a mesh of mat reinforcement with D40 bars. In total the square pier is comprised of about 27,600 elements. Additional views of the meshed pier with a circular cross section can be seen in Figure 4.19. With a 3.2 m cross sectional dimension of the pier, the pier to barge with ratio (α) is 0.3.

The circular pier is used to investigate different pier structures. Additional complexities are addressed in the following geometries. The effect of the foundation boundary condition is investigated. All other geometry and material properties, previously discussed, remain the same in the progression of the following geometries. The next series of models includes an array of 9 piles on the previously described circular pier. The piles are 8 m in length and are equally spaced on the mat of the foundation.

Steel pipe piles are assumed to have an outer diameter of 16 in and a wall thickness of 1 in. The piles are modeled with beam elements and relaxed when the piles are fixed at the base. After the pier has relaxed under self-weight, discrete (spring) elements are implemented every 0.5 m along the depth of each pier and are oriented along the X and Y axes. The pile configuration is shown in Figure 4.20.

American Petroleum Institute (API) load-displacement curves for sand are used to define the nonlinear, compression-only springs along the depth of the pile, for laterally loaded sand (API, 2007). The *p-y* curves were determined assuming a pile tip depth of one meter. The soil is assumed to be very stiff sand, with an internal friction angle, ϕ', of 40 and an effective unit weight, γ', 40 kN/m^3. For a specified depth, the ultimate lateral capacity of the soil (p_u) is determined as the least of either:

$$p_{us} = (C_1 H + C_2 D)\gamma' H \qquad \text{Equation 4.8}$$

$$p_{ud} = C_3 D \gamma' H \qquad \text{Equation 4.9}$$

where p_{us} and p_{ud} are the shallow and deep ultimate lateral bearing capacities (kN/m), respectively, γ' is the effective soil weight (kN/m^3), H is the soil spring depth (m), D is the average pile diameter from surface to depth (m), and the C_1, C_2, and C_3 are the coefficients determined from API (2007). The nonlinear *p-y* curve at each depth location is determined from:

$$P = A p_u \tanh\left(\frac{kH}{A p_u} y\right) \times L \qquad \text{Equation 4.10}$$

where A is a coefficient that accounts for variation between cyclic and static loading condition, p_u is the ultimate bearing capacity at depth, H, (kN/m), k is the initial

modulus of subgrade reaction (kN/m^3), y is the lateral deflection (m), and L_s is the tributary spring length.

A pier with a cap beam will also be analyzed (Figure 4.22). The bent beam is not designed to support a particular loading state. Rather, it allows the assumed superstructure mass to be distributed away from the column's axis. The bent beam is 1 m in thickness and extends 10 m in length and 4 m in width. Two layers of reinforcement are included with 0.25 m cover on the top and the bottom of the beam. The impact is situated so that the beam overhangs above the impacting vessel. The roadway deck, supported by the pier, would traverse perpendicular to the impact direction. The last model is a double column pier with a bent beam. The model was developed by essentially copying and transposing the previous model 8 m (Figure 4.23). There are 15 piles for the pier in this case and the mass on top of the pier is double so that the mass supported by an individual column is approximately the same as the previous models.

A fully loaded barge is placed to induce a head-on collision with the face of the pier visualized in Figure 4.24, where M_S is the superstructure mass and V_B is the velocity of the barge. The under-keel clearance of the barge is set to 1.0 m, assuming the top of the mat foundation is approximately at the same level as the location of the waterway bed. The center of the initial impact area is about 4.2 meters from the top of the foundation.

4.2.3 Assessment of Impact Results

Each impact case is analyzed with several different measures. Visually, the propagation of damage can be observed from the progressive flow of force as well as initiation of failure in the pier's FE model. System energy is crucial to ensure the validity

of simulation results. For this purpose, the time history of total energy of the system consisting of the potential, kinetic, and hourglass energies has been monitored throughout the analysis time frame. A time-history of the impact force between the hull plate of the barge and the column is recorded. The internal forces in the pier and foundation highlight the distribution and propagation of the energy as the impact is taking place. The temporal and spatial variations of the shear forces, bending moments, and displacements are also examined to measure the performance of the pier under different impact scenarios. For this purpose, horizontal sections are defined every meter along the height of the pier so that shear, moment and displacement diagrams can be developed.

In the initial stages of the impact there is a propagation of forces through the concrete pier. In Figure 4.25 the first 5.5 ms of the impact is shown with a constant fringe level for von Mises stress in the elements. The wave form of stress is apparent as the pier is introduced to the impact by the barge (not shown in the figure). Likewise, snapshots of the barge bow without the pier can be seen in Figure 4.26. The force propagation from the contact plane through the hull to the barge hopper is evident. Formation of the fringe contours clearly shows the influence of the barge internal structure on the dissipation of the forces through the rest of the structure.

4.2.3.1 Energy

Considering the pier-barge model as a closed system with no additional mechanical energy introduced, the total energy must remain constant throughout the simulation. The kinetic energy in the system is introduced through bodily motions. The pier, after dynamic relaxation, has internal stress; however, it is at a state of rest. The

kinetic energy in the model is due to the motion of the barge, which can, initially, be calculated by the following formula:

$$E_{kin} = \frac{1}{2} m V^2 \qquad \text{Equation 4.11}$$

where m and V are the mass and velocity of the barge, respectively. In the case of impact, kinetic energy may not be conserved, but the momentum of the system must be conserved. Although the pier is fixed in space, motion is still permitted in the pier. In addition, the material models used for the pier allow permanent deformations and failure. Similarly, the barge is also deformable. The conservation of energy is not violated, but rather energy has been transformed. In the case that kinetic energy is conserved the collision is assumed to be perfectly elastic.

Internal energy, as measured in LS-DYNA, includes both the elastic strain energy and the work done in permanent deformations. This is an incremental calculation based on the six components of stress and strain. The following calculation is made for each element and summed to get the total internal energy in the model.

$$e_{\text{int}}^{n+1} = e_{\text{int}}^{n} + V_{ele} \sum \left(\sigma \times \Delta \varepsilon \right) \qquad \text{Equation 4.12}$$

The sliding energy is the energy lost due to friction in contact. Hourglass energy reports the dissipated energy due to the induced internal forces resisting the divergent modes. External work represents the work done by applied forces, pressures, and the work done by the velocity, displacement or acceleration boundary conditions. The total energy is a sum of the reported energies by the program. In total it is defined as:

$$E_{total} = E_{kin} + E_{int} + E_{slide} + E_{rw} + E_{damp} + E_{hg} \qquad \text{Equation 4.13}$$

where

$E_{total} = total \quad energy$
$E_{kin} = kinetic \quad energy$
$E_{int} = internal \quad energy$
$E_{slide} = sliding \quad energy$
$E_{rw} = rigidwall \quad energy$
$E_{damp} = damping \quad energy$
$E_{hg} = hourglass \quad energy$

A perfect energy balance is defined when the initial total energy and the external work, W_{ext}, sum to the total energy. That is:

$$E_{total} = E_{kin}^{0} + E_{int}^{0} + W_{ext} \qquad \text{Equation 4.14}$$

The system energy is reported in Figure 4.27 for the baseline case. The kinetic energy drops through the simulation time, where at the end of the simulation is approximately zero. Some kinetic energy is still present due to the movement of the mass in the pier elements. Simulation end time occurs when no contact force exists between the barge and the pier. Some fluctuations in the total energy was observed, however energy balance is still persevered when considering the external work.

4.2.3.2 Impact Forces

The highly nonlinear nature of impact problems drives the complexity of their solutions. Simplifying the derivation of impact forces should be approached through basic physics principles. The work-energy principle relates the work done to the kinetic energy. In the theorem the net work can be define in the following manner:

$$W_{net} = \Delta E_{kin} = E_{kin}^{n+1} - E_{kin}^{n} \qquad \text{Equation 4.15}$$

where the work done or net work is a product of the work done to the barge and the pier:

$$W_{net} = W_{pier} + W_{barge} \quad \text{Equation 4.16}$$

Work can be expressed by the following expression:

$$W = Fd \quad \text{Equation 4.17}$$

where F is the force and d is the displacement. If the moving body is at rest after the impact, the impact force can be expressed as:

$$F_{impact} = \frac{1}{2}\frac{mV^2}{d} \quad \text{Equation 4.18}$$

In modeling the contact behavior, a surface is defined where one body cannot penetrate another. To idealize the contact forces, Figure 4.28 depicts two bodies in contact. The faded part represents the body before contact forces, f_{ni}, are applied to prevent penetration of the second body. In this particular case, nodal forces are applied until penetration no longer exists. Work can be determined for each applied force. The sum of all forces would result in the total impact force.

The impact force time history for the square baseline simulation can be seen in Figure 4.29. Almost instantaneously, a peak force of 21.76 MN is reached. The force quickly drops to around 12 MN in approximately 8 ms. The immediate spike in force is one of the characteristics of square pier impacts as noted in the previous section. A steady decrease was observed until about 0.2 seconds. In the period between 0.2 and 0.3 seconds, significant plastic strain is developed in the pier as well as elements in the mat foundation adjacent to the column. The impact force gradually dissipates until no contact force exists at about 0.7 s.

4.2.3.3 Shear, Moment and Displacement Diagrams

Section forces show the behavior and flow of forces through the pier. Examining the performance of the pier with shear, moment and displacement diagrams is critical in evaluating the vulnerability of bridges. Additionally, this data can be used to graphically visualize the behavior of the materials and structural components. Horizontal sections are selected prior to analyzing a simulation every meter along the height of the pier. Shear forces are defined as the forces acting in the direction of the applied force. Hence, assuming the barge velocity is in the x-axis direction, the shear force is the x-force component. The force contributions in the other directions are found relatively minimal. Reported bending moments are about the y-axis to correspond to the previously described shear forces. Lastly, the displacement is determined by the x-location of the centroid. Using this assumption with erodible solid elements can lead to abnormalities in the centroid location. When a row of elements delete due to erosion, the centroid will also shift, often resulting in an intuitively unexpected displacement value. The shear and bending moment diagrams for the initial onset of the impact are shown in Figure 4.30. Initially a wave of shear forces is formed and propagates through the length of the pier on either side of the impact location. On the top portion, there is a distinct wave amplitude that can be traced in each time step flowing toward the top of the pier.

4.2.3.4 Barge Crush Depth

The AASHTO Specifications uses the damage of the bow to empirically prescribe a static design force. The barge crush depth is recorded for each simulation to further compare to the AASHTO Specifications. Barge crush depth gradually increases through the simulation. Just over halfway through the simulation, the crush depth decreases

which shows the rebounding elastic properties of the steel barge. Figure 4.31 shows the time history of the barge crush depth for the baseline simulation. Damage is recorded as the crush depth at the end of the simulation time as no force is applied to the barge at this point in the simulation.

4.2.4 Comparison of Results

Results have been collected from 25 different simulations; five simulations for each of the geometries detailed earlier. Each of the impact scenarios have been assigned a title where they can be differentiated from one another. For example, the impact case where a barge is traveling with the velocity of 2 m/s into a pier column supporting 300 tons is designated as "v2m300" where 'v' stands for the velocity and 'm' indicates the superstructure mass.

4.2.4.1 Fixed Square Pier

A summary of several different performance metrics are observed and reported in Figure 4.32 through Figure 4.35. The impact force time histories have the characteristics of the impact force plots found in the previous section for the barge impact to the rigid square pier. The similarity in the plots is predictable given that the stiffness of the pier and concrete is much higher than the barge model. Upon decreasing velocity, the peak impact force also decreases while the duration of the impact increases proportionally. For the cases where the velocity is the same and a variation of the mass supported by the column is considered, similar plots are obtained. These plots are virtually the same for the first 0.15 s. After that, the impact force transferred into the column as shear force can interact with the top mass, which generates the inertial forces resisting the movement.

The investigation of the five cases demonstrates that the crush depth is dependent, not only on the kinetic energy of the barge, but also on the boundary condition of the top of the pier (Figure 4.33). First observing the cases where the mass is set to 300 tons, there appears to be a linear trend between the three points. The velocity of the barge is expected to have a great impact on the crush depth of the barge bow. The trend between the three cases where the velocity was the same and the top mass was changed could be particularly interesting. This highlights a relationship between the crush depth and the mass on top of the pier. This can be explained by the pier resistance to the movement and deformation. When a larger mass is placed on top of the pier, the mass is more resistant to move. As a result, the energy that would be used to displace the pier is transferred to damage in the barge bow.

The maximum shear and moment, reported in Figure 4.34, should be approximately related to the impact force trend discussed earlier. Additionally, as the shear and the moment in the pier are correlated the trend between the cases for the shear should be approximately the same as the trend for the bending moment. The last metric that is observed is displacement of the top of the pier (Figure 4.35). It first appears that there is never a case where the pier returns back to its initial location. This is primarily due to the termination criteria set for the simulations. A simulation is set to end when there is no longer a force between the barge and the pier. This plot can represent the cases when the velocity or kinetic energy of a barge is so great that the pier fails, as is the case for the v4m300 simulation. However, in other cases, it is some delicate balance of the elasticity of the impact, the crushing of the barge and the motion of the pier. For

cases with a velocity of 2 m/s, there is a sense that that the pier should begin to return back near its initial state based on the apparent downward trend in displacement.

4.2.4.2 Fixed Circular Pier

The impact force time histories for the circular piers also tend to follow the trends observed in the barge impacting rigid circular piers (Figure 4.36). In general, the greater the velocity the more monotonic increase is observed. In these cases, however, the duration of the impact was dependent on the impact conditions. In the v2m150 and v4m200 cases, the durations of the impact are much greater than the others. This behavior is due to damage and deformation in the pier. The two cases where this occurs are the fastest velocity and the pier that is the least resistant to inertia. Finally, the peak impact forces observed were much less than those observed with impacts involving square piers. This is attributed to the area of the contact surface, where this area grows during the impact for circular piers.

As observed in past simulations, the barge damage depth is closely associated with the velocity or kinetic energy of the barge (Figure 4.37). However for the case of circular piers it appears that there is virtually no effect from the mass at the top of the pier. Since the applied impact forces are less than the square pier case, it is expected to see this trend for shear forces and bending moments. In the two cases mentioned above, they are also associated with particularly lower moments than that would be expected (Figure 4.38). This may be due to the larger deformations that occur in those cases. The v4m300 case fails and the v2m150 has a large deformation although it is still able to recover from the displacement experienced (Figure 4.39).

4.2.4.3 Circular Pier with Piles and Cap Beam

The next set of figures is for the cases where deep piles are add to a circular pier model. Instead of observing the impact force time histories for each impact, a summary is included where the maximum and average force is plotted with the impact duration (Figure 4.40). There is essentially no difference in the impact force between the cases with or without the pile foundation. However the duration of the forces is somehow different, where they are approximately the same when impact cases are compared to each other for geometries that include the piles. The crush depth has not changed significantly either (Figure 4.41). It is clear that the pattern is similar to the pattern observed for the maximum impact force plot just discussed. There has been some decrease in the damage depth of the bow. Piles are relatively close to the impact location and where springs can quickly engage and absorb some of the energy that previously resulted in greater damage in the bow.

The shear and moment trend is similar to that of the fixed foundation case, but less pronounced (Figure 4.42). The forces can distribute through the 9 piles and soil springs that make up the foundation. An increased displacement was recorded at the top of the pier. However, since the piles additionally contribute to the structural system, the entire pier displaces as well as a rotation or bending of the pier due to the force (Figure 4.43). The case of circular pier with piles and cap beam show an almost identical response to the figures discussed for the circular pier without the cap beam.

4.2.4.4 Double Circular Pier with Piles and Cap Beam

The last set of this series is the double column pier with piles and cap beam. This structure is the most different from all the others previously observed. The first column

is more resistant to damage because of the additional support that the second column provides to the structure. Furthermore, the mass was defined as the mass supported by each column. Hence, in addition to the increased mass of the concrete, due to a larger structure, the mass on top is doubled as well. Despite the stiffer structure, the maximum impact forces are almost identical to the impact forces seen in the previous cases (Figure 4.48). The barge damage depth is approximately the same as was seen in earlier simulations (Figure 4.49). The double column structure has induced more damage to the barge, with approximately a 5 mm increase in damage. This could be due to the additional stiffness and resistance of the structure. The shear and moments observed are comparable to the other simulations (Figure 4.50). Once again the two cases that stand out are the same as observed in earlier simulations. These cases also show a quicker rebound of the top of the pier to its original position (Figure 4.51). Because the structure is stiffer and more massive, all the curves indicate that the piers are beginning to move back toward their original positions.

4.3 Goldstar Memorial Bridge

The final part of this research will investigate the performance of a pier on the Goldstar Memorial Bridge. The Goldstar Memorial Bridge connects New London and Groton Connecticut, via Interstate 95 over the Thames River (Figure 4.52). The bridge is a set of twin bridges carrying the south bound lanes (1) and the north bound lanes (2). There is also a rail bridge, the Groton Amtrak Bridge (3). What is now the northbound span began construction just before WWII and was completed in 1943 (Figure 4.53). The bridge was named to commemorate the veterans whose lives were sacrificed in WWII.

The southbound bridge was finally completed in 1972. The Goldstar Bridge is the longest spanning bridge in the state, spanning 6000 feet with 11 spans.

Piers 22and 23 of the southbound bridge are the focus of this case study. Despite being constructed before the idea of the AASHTO code was conceived, visually the exposed pier (Pier 22/23) was designed more robustly than its adjacent pier on the northbound bridge (Figure 4.54). It is possible that engineers were attempting to accommodate for the threat of some possible vessel impact. Despite this precaution, the bridge should still be inspected and examined to meet the current standards. It will not be the goal of the current study to specifically determine if the pier meets the current requirements of the design codes. Rather to provide a simulation of an impact with the predicted measures for evaluating a pier and the forces imposed onto the pier.

Construction drawings were used to develop a detailed model of the pier (Figure 4.55), where Piers 22 and 23 are virtually identical. In summary, the pier is a two-column bent with cap beam. At the base of the column there is a foundation with a rounded edge that extends to the river bed where additional concrete caps the steel deep pile foundation. Because there are about 200 piles that make up the deep foundation, it was determined that a fixed foundation would be appropriate at the base of the concrete. There are 5 different sections with different reinforcing protocols identified throughout the bent that were detailed in the model (Figure 4.56). The concrete strength is 2.5 ksi, whereas the yield strength of the reinforcing steel is 60 ksi. Similar to the previous pier studies, the superstructure tributary mass (~30,000 tons) was added to the top of the pier and stresses were induced due to the self-weight prior to the impact simulation.

At the location of the bridge, the largest passing vessel is not a jumbo hopper barge. Rather it has been identified as a specific vessel. The ATB Freeport, built by the U.S. Shipping Corp., is a chemical transporter. Shown in Figure 4.57, the highlighted portion is still recognized as a barge, holding chemicals in the hull, being pushed by a tugboat. The vessel transports a full load north on the Thames River and returns with an emptied cargo south. Naval architecture and construction is often proprietary and very difficult to access. The image from the previous figure and some basic dimensions on the manufacturer's website was used to develop a model of the vessel as can be seen in Figure 4.58. Because the structure of the ATB Freeport is not known, the model was assumed to be rigid. This assumption is conservative as the pier can only experience plastic deformations and no loss of energy through the damage in the vessel.

The impact was set up so that the ATB Freeport impacts the pier head-on with a velocity of 2 m/s. According to the manufacturer's website, the net registered tonnage is 9726 tons with a draft of 28 ft. The initial state of the simulation can be seen in Figure 4.59. A global damping of 2% was also assigned to the model to damp out body motions slowly. At the end of the simulation the plastic strain and erosion in the pier can be inspected to determine to predicted damage in the pier (Figure 4.60). A high level of plasticity in the concrete is seen at the impact site. The plastic damage continues under the column nearest to the impact, possibly compromising the column. Additionally there are small levels of straining that may occur at the joints between the columns and the cap beam. The impact force time history has an initial spike soon damping to minimal force. The first 0.5 seconds of the force time history is shown in Figure 4.61 where the maximum recorded force is 56.35 MN. With focus on the columns of the structure, the

maximum shear and moment at the base of the column nearest to the impact was recorded as 4.65 MN and 14.41 MN-m, respectively. Additionally, there was a maximum displacement of 3.1 mm recorded on the top of the pier. Based on the FE simulations conducted on the 3D model of the piers for the mid-span of the Goldstar Memorial Bridge, the details of the damage developed at the contact face can be captured. Additionally, the forces recorded from the sections can be used to assess the structural response and vulnerability of the entire bridge under a specific impact condition.

Table 4.1 Structural steel sections used to develop bow truss sections

Section	L5×3×5/16	L6×3 1/2×5/16	L3 1/2 × 3 1/2×5/16
D1 [in (mm)]	3.00 (76.20)	3.50 (88.90)	3.50 (88.90)
D2 [in (mm)]	0.50 (12.70)	0.31 (7.94)	0.31 (7.94)
D3 [in (mm)]	5.00 (127.00)	6.00 (152.40)	3.50 (88.90)
D4 [in (mm)]	0.50 (12.70)	0.31 (7.94)	0.31 (7.94)
A_c [in^2 (mm^2)]	3.75 (2419.35)	2.87 (1852.31)	2.09 (1348.28)
A_{st} [in^2 (mm^2)]	15.00 (9677.40)	21.00 (13548.40)	12.25 (7903.21)
R_A	0.25	0.14	0.17

Section	L5×5×5/16	L6×4×1/2
D1 [in (mm)]	5.00 (127.00)	4.00 (101.60)
D2 [in (mm)]	0.31 (7.94)	0.50 (12.70)
D3 [in (mm)]	5.00 (127.00)	6.00 (152.40)
D4 [in (mm)]	0.31 (7.94)	0.50 (12.70)
A_c [in^2 (mm^2)]	3.03 (1953.12)	4.75 (3064.51)
A_{st} [in^2 (mm^2)]	25.00 (16129.00)	24.00 (15483.80)
R_A	0.12	0.20

Section	C12×20.7	C 10 × 15.5
D1 [in (mm)]	3.00 (76.20)	2.62 (66.67)
D2 [in (mm)]	0.50 (12.70)	0.44 (11.11)
D3 [in (mm)]	12.00 (304.80)	10.00 (254.00)
D4 [in (mm)]	0.31 (7.94)	0.25 (6.35)
A_c [in^2 (mm^2)]	6.44 (4153.22)	4.58 (2953.62)
A_{st} [in^2 (mm^2)]	36.00 (23225.80)	26.25 (16935.50)
R_A	0.18	0.17

Table 4.2 Hopper mass definitions for given barge loading conditions

Loading Condition	Barge Mass short ton (metric ton)	Hopper Density [kg/m^3]	Added Mass [kg]
Fully Loaded	1900 (1723.7)	3227	270
Half Loaded	1050 (952.6)	1744	703
Quarter Loaded	625 (567.0)	1004	89
Emply Barge	200 (181.4)	262.9	48

Table 4.3 Coefficient of restitution for a single barge impacting square piers

m_B short ton (metric ton)	V_B m/s	Coefficient of Restitution e					
		α = 0.1	α = 0.3	α = 0.5	α = 0.7	α = 0.9	α = 1.0
1900 (1723.7)	0.5	0.354	0.460	0.466	0.631	0.773	0.803
	1	0.246	0.280	0.302	0.341	0.387	0.419
	2	0.199	0.195	0.175	0.173	0.184	0.233
	3	0.184	0.164	0.149	0.165	0.143	0.161
	4	0.156	0.148	0.152	0.156	0.140	0.143
1050 (952.6)	0.5	0.470	0.541	0.693	0.915	0.891	0.916
	1	0.265	0.335	0.362	0.528	0.453	0.541
	2	0.202	0.206	0.212	0.221	0.255	0.304
	3	0.201	0.184	0.182	0.197	0.151	0.217
	4	0.182	0.166	0.138	0.166	0.142	0.157
625 (567.0)	0.5	0.576	0.622	0.817	0.915	0.931	0.920
	1	0.330	0.398	0.456	0.528	0.638	0.776
	2	0.225	0.245	0.257	0.287	0.308	0.327
	3	0.211	0.169	0.173	0.197	0.214	0.281
	4	0.197	0.179	0.178	0.166	0.146	0.202
200 (181.4)	0.5	0.754	0.918	0.751	0.866	0.822	0.836
	1	0.523	0.504	0.832	0.827	0.839	0.833
	2	0.288	0.334	0.347	0.410	0.528	0.732
	3	0.234	0.264	0.264	0.284	0.278	0.409
	4	0.231	0.198	0.214	0.214	0.265	0.253

Table 4.4 Coefficient of restitution for a single barge impacting circular piers

m_B short ton (metric ton)	V_B m/s	Coefficient of Restitution e					
		α = 0.1	α = 0.3	α = 0.5	α = 0.7	α = 0.9	α = 1.0
1900 (1723.7)	0.5	0.331	0.365	0.371	0.375	0.377	0.378
	1	0.291	0.282	0.280	0.281	0.288	0.287
	2	0.263	0.245	0.238	0.225	0.220	0.220
	3	0.252	0.240	0.216	0.206	0.204	0.202
	4	0.197	0.205	0.197	0.195	0.181	0.180
1050 (952.6)	0.5	0.354	0.382	0.424	0.444	0.453	0.455
	1	0.300	0.304	0.301	0.304	0.306	0.306
	2	0.283	0.269	0.261	0.255	0.252	0.248
	3	0.263	0.245	0.234	0.229	0.214	0.209
	4	0.251	0.239	0.217	0.204	0.205	0.202
625 (567)	0.5	0.405	0.415	0.440	0.475	0.501	0.501
	1	0.319	0.337	0.339	0.339	0.340	0.341
	2	0.290	0.277	0.272	0.275	0.271	0.270
	3	0.272	0.257	0.243	0.240	0.244	0.234
	4	0.261	0.244	0.234	0.223	0.211	0.208
200 (181.4)	0.5	0.527	0.582	0.598	0.628	0.657	0.649
	1	0.362	0.387	0.417	0.440	0.453	0.461
	2	0.302	0.308	0.312	0.313	0.318	0.319
	3	0.281	0.275	0.274	0.272	0.275	0.275
	4	0.283	0.272	0.264	0.260	0.252	0.254

Table 4.5 Summary of impact simulations of fully loaded barges into square piers with a velocity of 1.8 m/s (3.5 knots)

Ratio α	Impact Force (MN)			Coefficient of Restitution e	Duration t_d (s)	Damage Depth a_B (m)
	P_{max}	$\overline{P}_{1/2} / P_{max}$	$\overline{P} / P_{max}$			
0.1	10.70	0.669	0.581	0.199	0.622	0.378
0.2	15.57	0.650	0.474	0.204	0.533	0.266
0.3	19.77	0.652	0.445	0.189	0.437	0.233
0.4	27.05	0.554	0.382	0.195	0.375	0.181
0.5	32.66	0.568	0.375	0.183	0.312	0.147
0.6	38.73	0.574	0.376	0.184	0.264	0.123
0.7	43.59	0.589	0.385	0.188	0.230	0.106
0.8	48.95	0.584	0.362	0.169	0.214	0.094
0.9	52.83	0.569	0.383	0.207	0.193	0.086
1.0	63.63	0.614	0.393	0.251	0.161	0.059

Table 4.6 Summary of impact simulations of fully loaded barges into circular piers with a velocity of 1.54 m/s (3.0 knots)

Ratio α	Impact Force (MN)			Coefficient of Restitution e	Duration t_d (s)	Damage Depth a_B (m)
	P_{max}	$\overline{P}_{1/2} / P_{max}$	$\overline{P} / P_{max}$			
0.1	7.85	0.608	0.616	0.189	0.700	0.357
0.2	8.14	0.640	0.614	0.184	0.672	0.341
0.3	8.80	0.618	0.587	0.181	0.647	0.327
0.4	9.19	0.608	0.578	0.177	0.627	0.319
0.5	8.93	0.653	0.596	0.174	0.624	0.307
0.6	9.17	0.668	0.592	0.172	0.610	0.295
0.7	9.35	0.687	0.592	0.171	0.599	0.286
0.8	9.31	0.721	0.604	0.171	0.590	0.278
0.9	9.38	0.737	0.611	0.171	0.577	0.271
1.0	9.86	0.724	0.592	0.169	0.565	0.266

Table 4.7 Summary of impact simulations of fully loaded barges into circular piers with a velocity of 2.57 m/s (5.0 knots)

Ratio α	Impact Force (MN)			Coefficient of Restitution e	Duration t_d (s)	Damage Depth a_B (m)
	P_{max}	$\overline{P}_{1/2} / P_{max}$	$\overline{P} / P_{max}$			
0.1	8.74	0.749	0.673	0.256	0.935	0.809
0.2	9.58	0.728	0.639	0.247	0.895	0.772
0.3	12.04	0.617	0.551	0.265	0.826	0.684
0.4	13.26	0.574	0.542	0.274	0.759	0.636
0.5	13.96	0.564	0.545	0.256	0.717	0.611
0.6	14.12	0.570	0.572	0.249	0.673	0.587
0.7	15.10	0.547	0.554	0.252	0.649	0.567
0.8	15.32	0.547	0.570	0.249	0.621	0.549
0.9	15.19	0.560	0.600	0.252	0.596	0.537
1.0	15.48	0.562	0.611	0.249	0.573	0.527

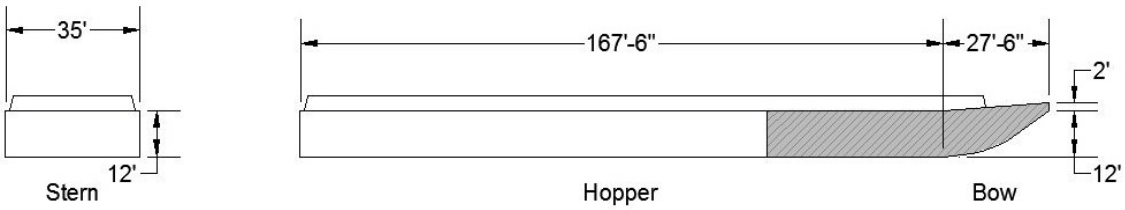

Figure 4.1 Simplified schematic view of Jumbo Hopper barge

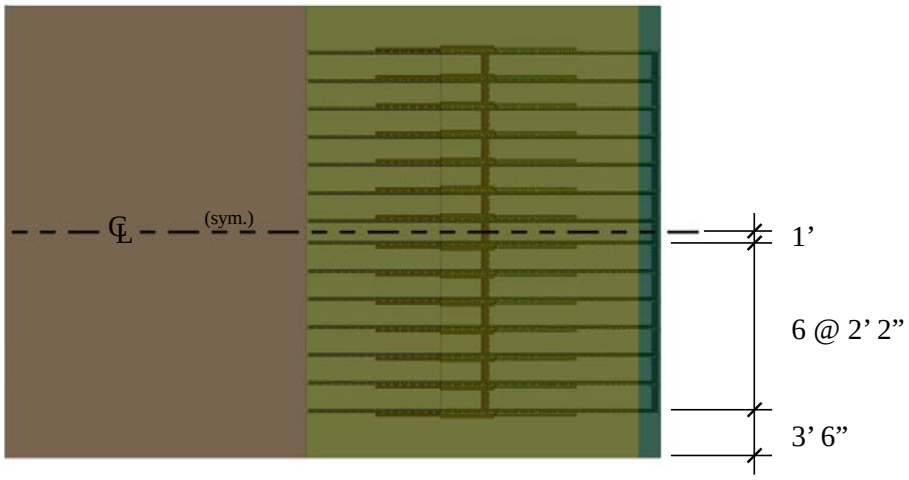

Figure 4.2 Layout of bow truss

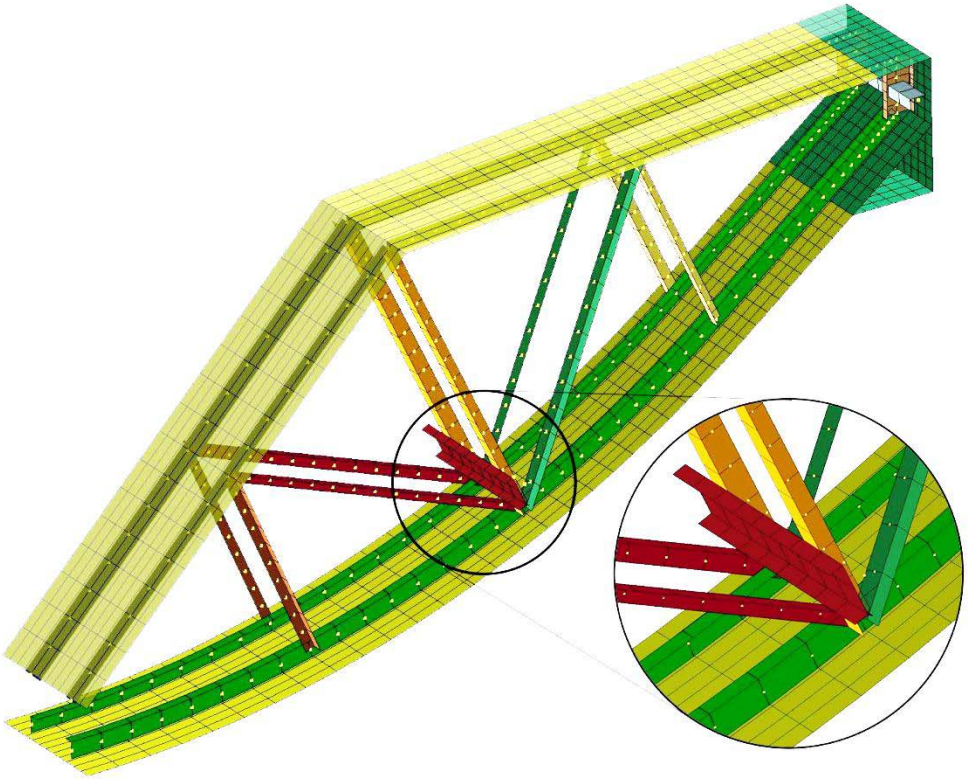

Figure 4.3 Isolated center trusses displaying the orientation of structural members

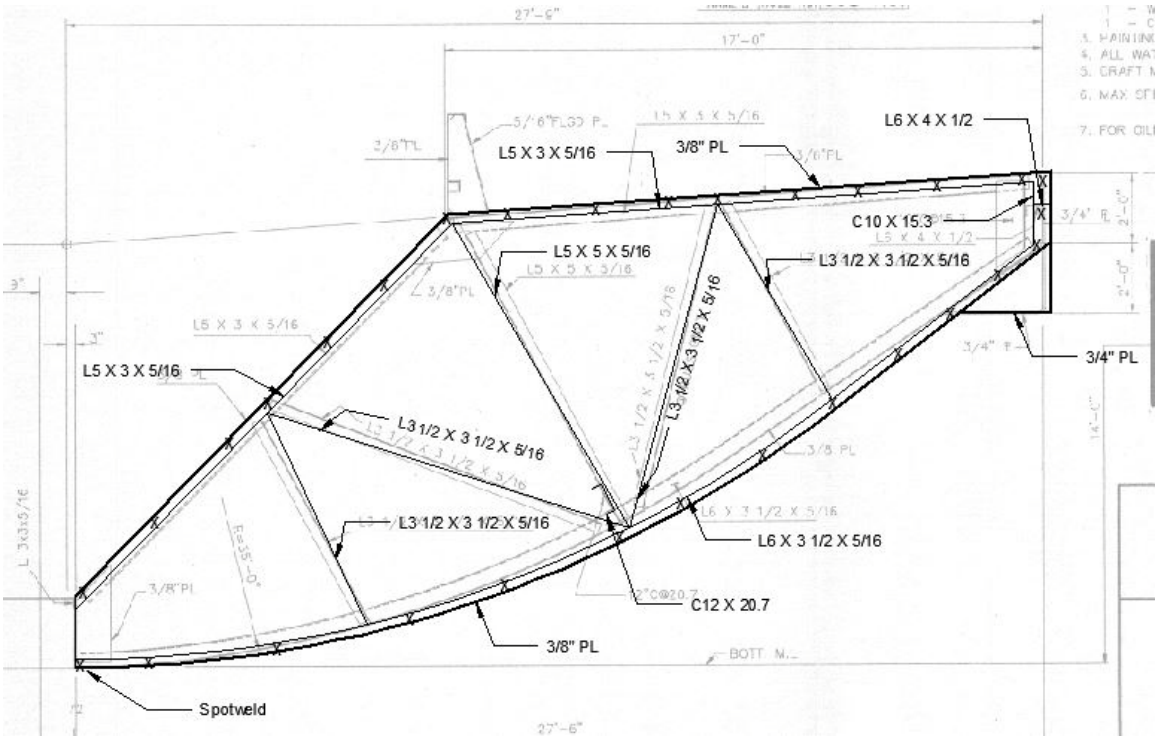

Figure 4.4 Bow truss structure construction drawing with model geometry overlay

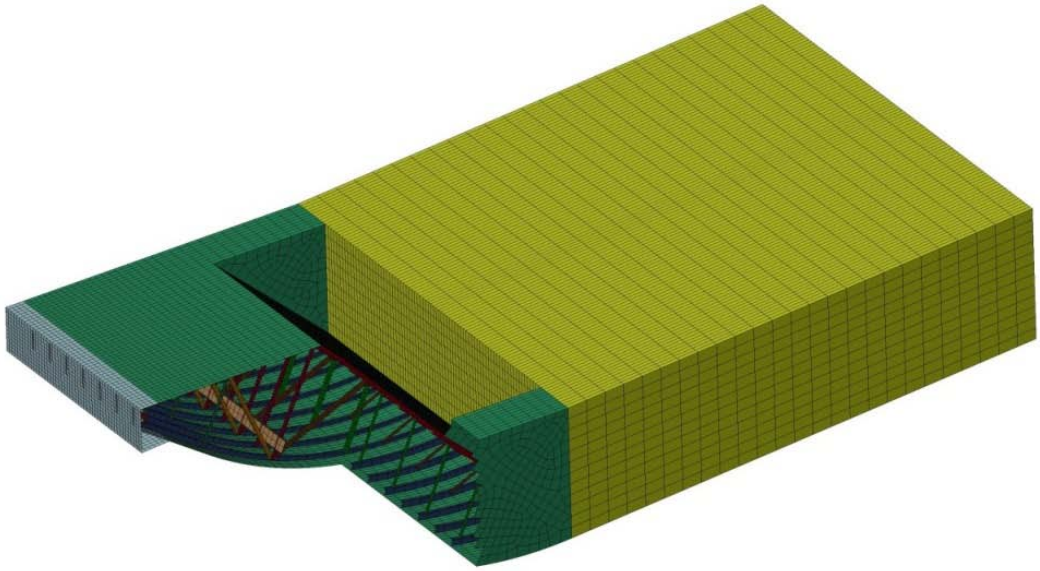

Figure 4.5 Barge model elements with bow cut-out displaying beam cross-sections

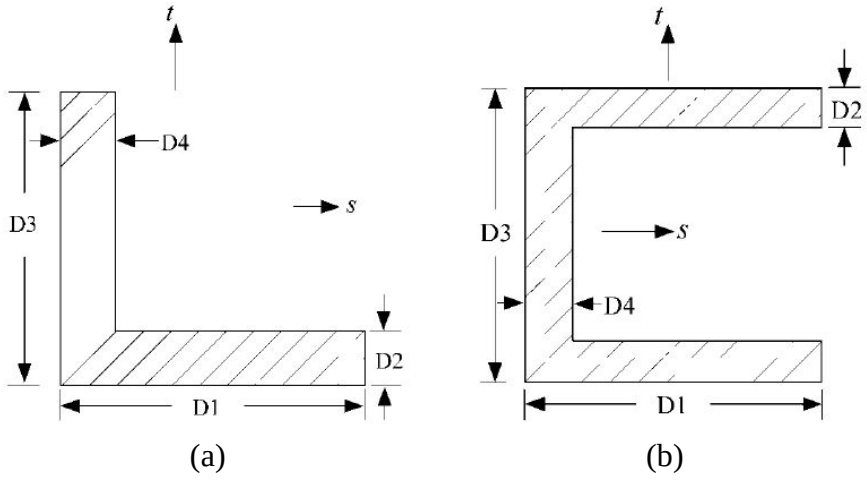

Figure 4.6 LS-DYNA beam integration section dimension definitions for angles and channels

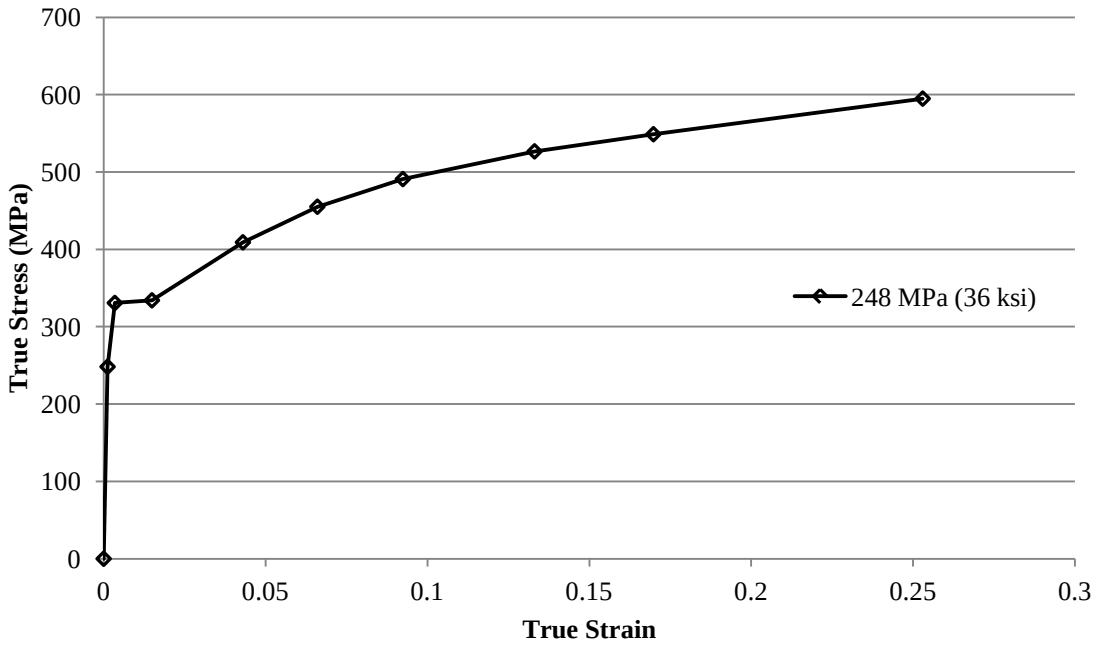

Figure 4.7 Nonlinear steel model used for barge bow displayed as true stress and true strain

Figure 4.8 Old Sunshine Skyway Bridge (front) with replacement (back)

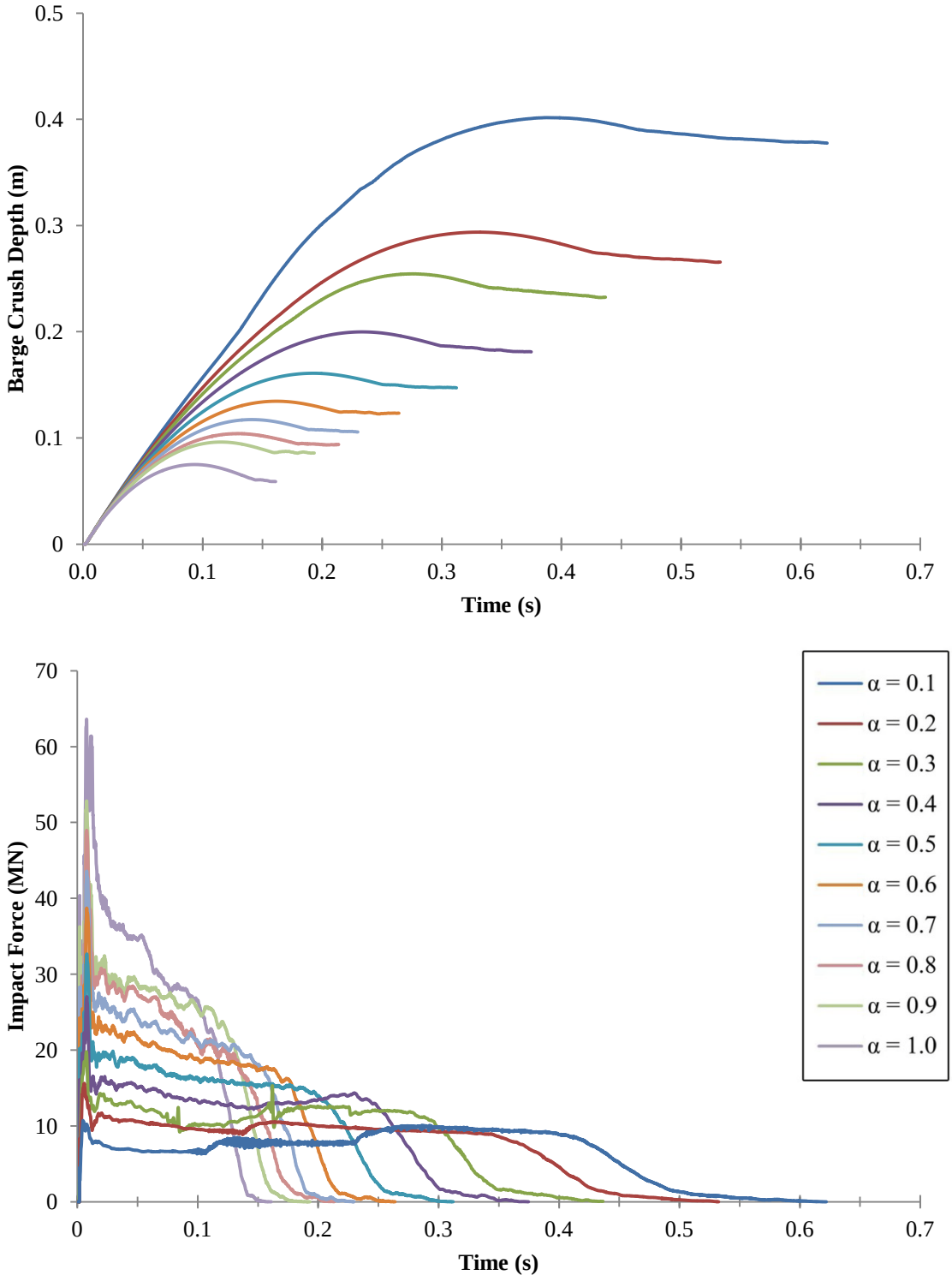

Figure 4.9 Barge crush depth (above) and impact force (below) of a fully loaded barge impacting square piers at 1.8 m/s (3.5 knots)

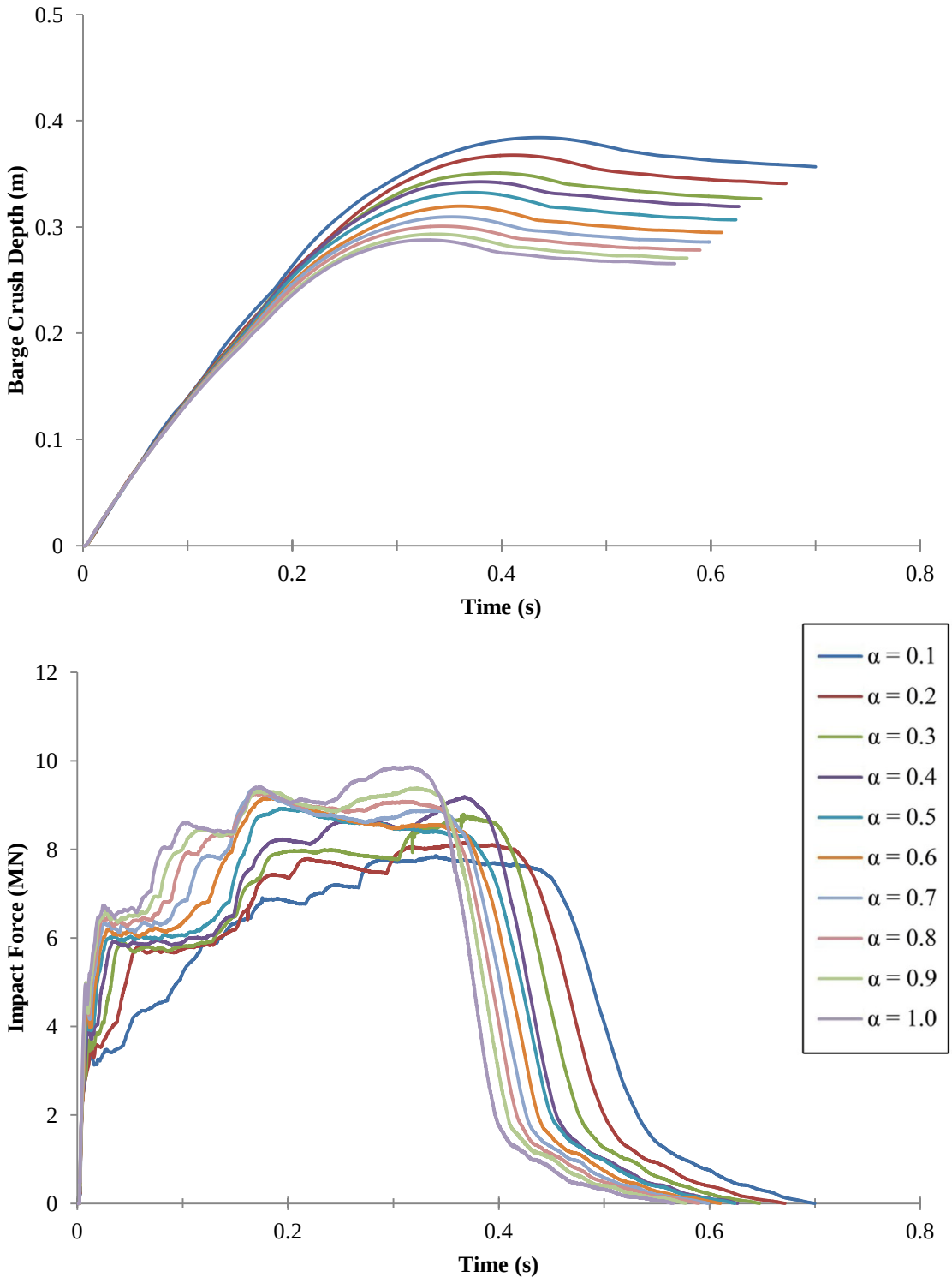

Figure 4.10 Barge crush depth (above) and impact force (below) of a fully loaded barge impacting circular piers at 1.54 m/s (3.0 knots)

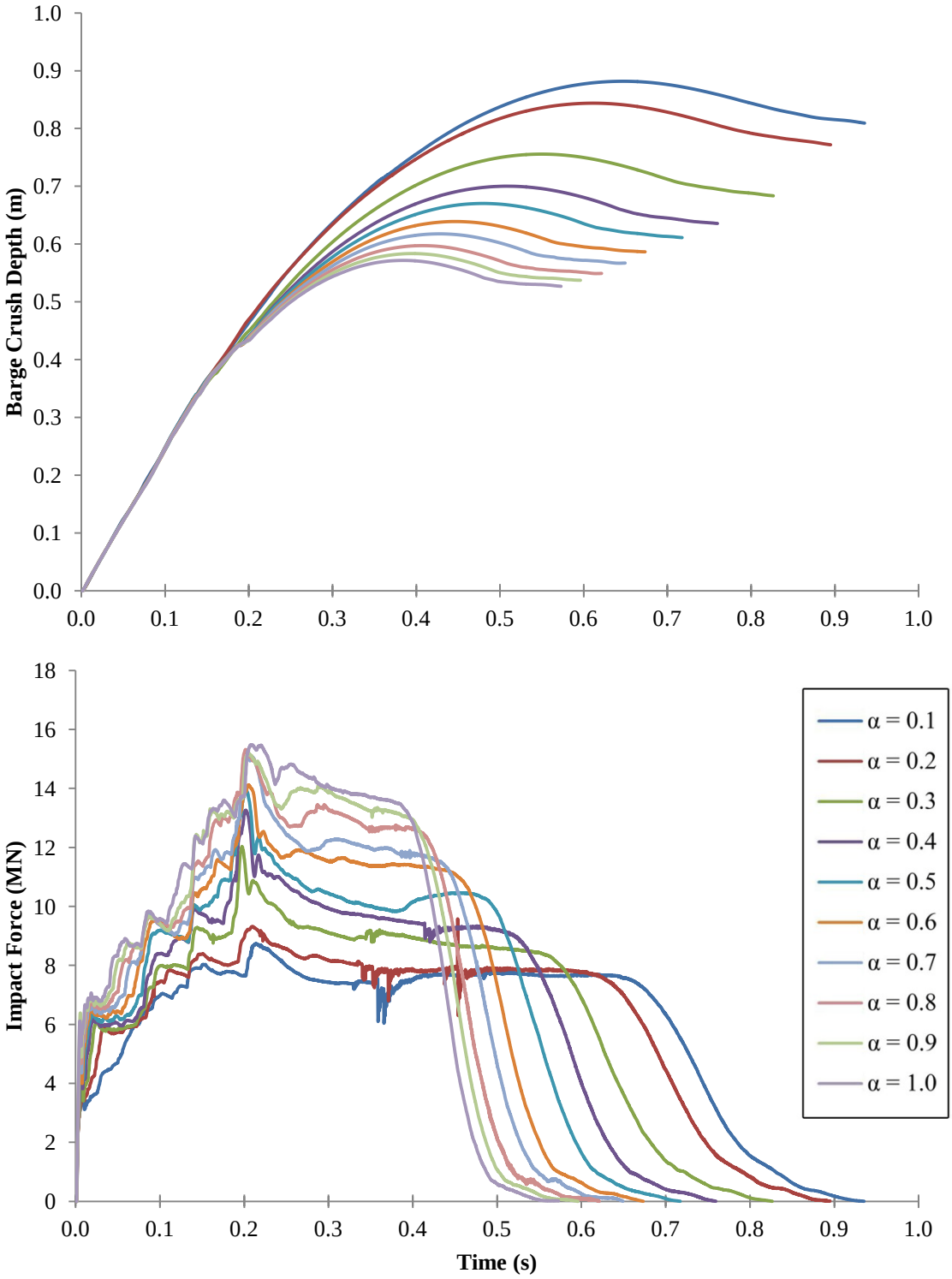

Figure 4.11 Barge crush depth (above) and impact force (below) of a fully loaded barge impacting circular piers at 2.57 m/s (5.0 knots)

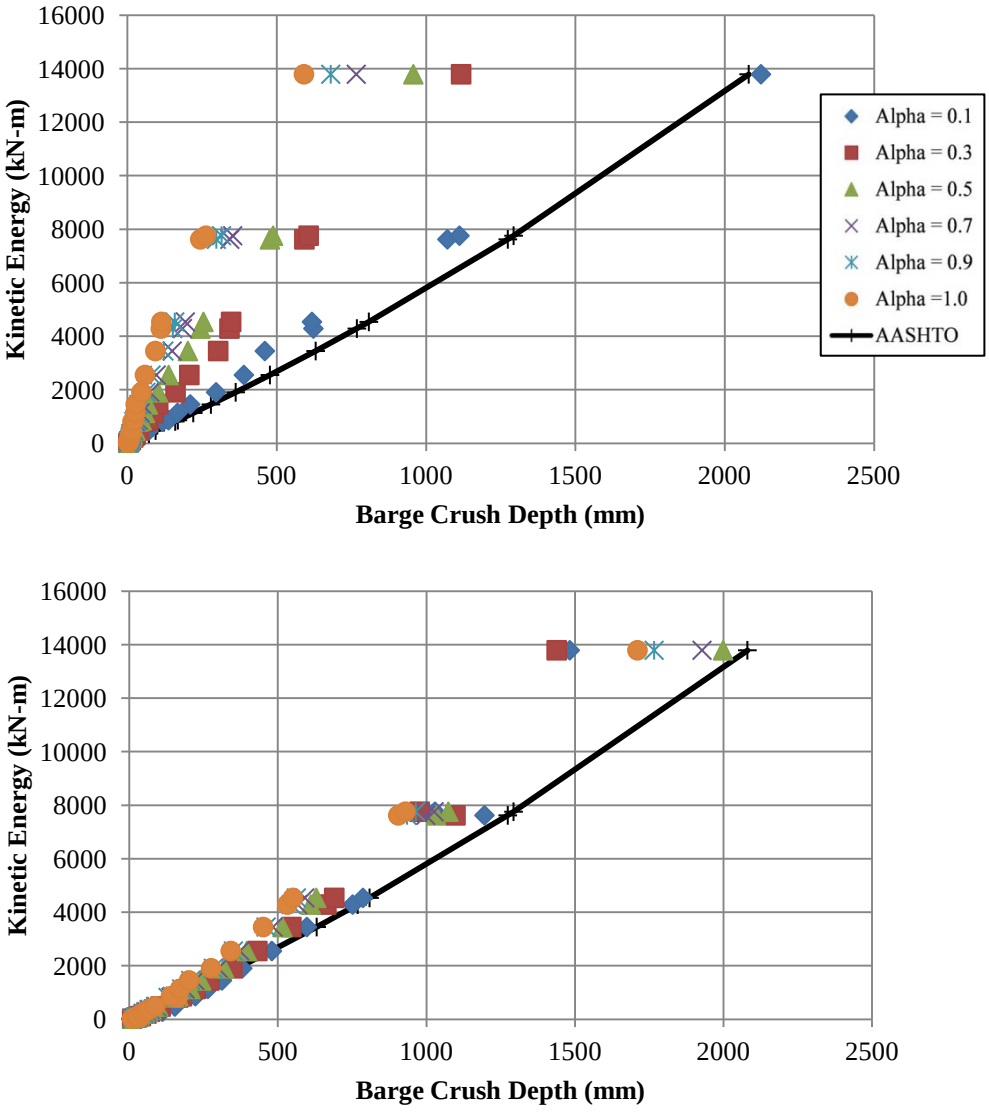

Figure 4.12 Barge crush depth versus kinetic energy for impacts on rigid square (above) and circular (below) piers.

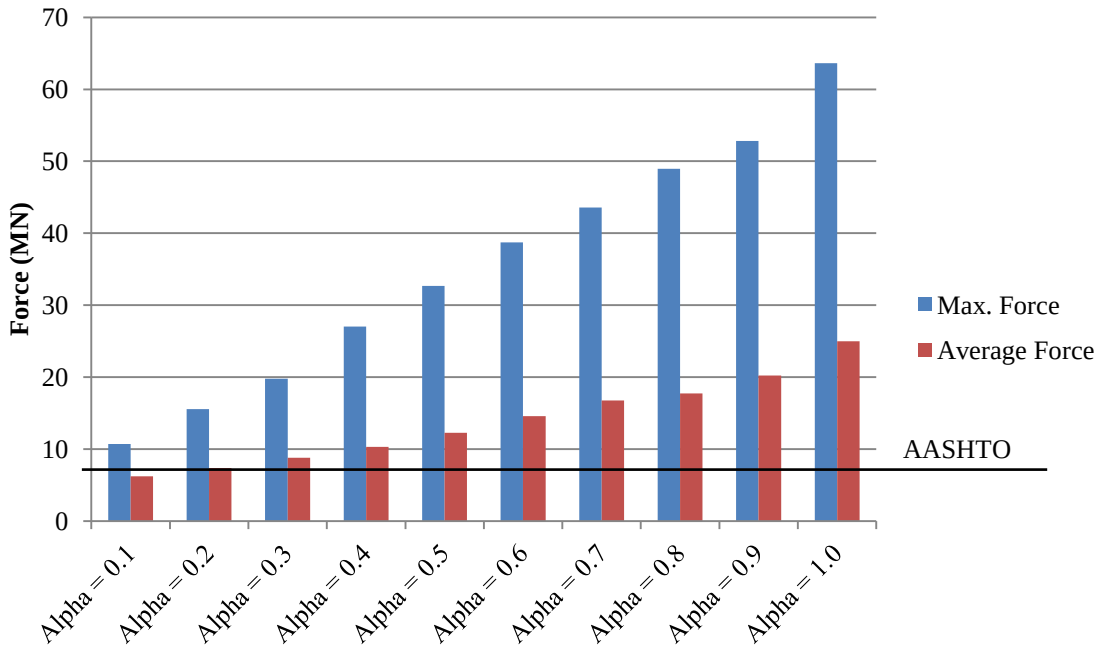

Figure 4.13 Maximum and average impact force compared to AASHTO design load for fully loaded barge impacting square piers at 1.8 m/s

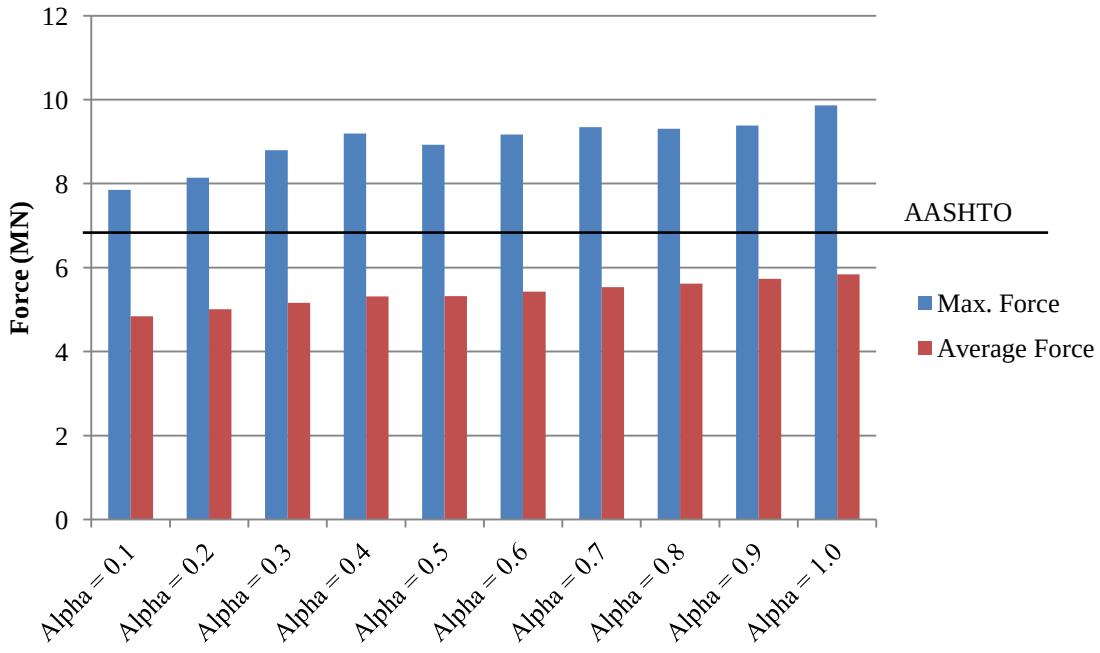

Figure 4.14 Maximum and average impact force compared to AASHTO design load for fully loaded barge impacting circular piers at 1.54 m/s

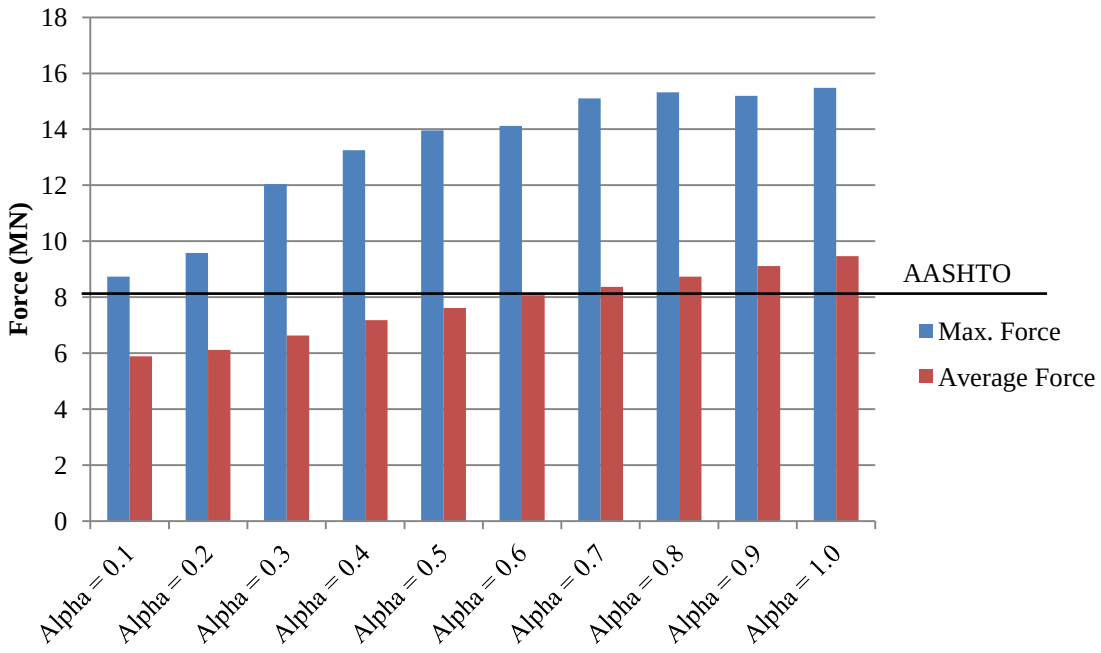

Figure 4.15 Maximum and average impact force compared to AASHTO design load for fully loaded barge impacting circular piers at 2.57 m/s

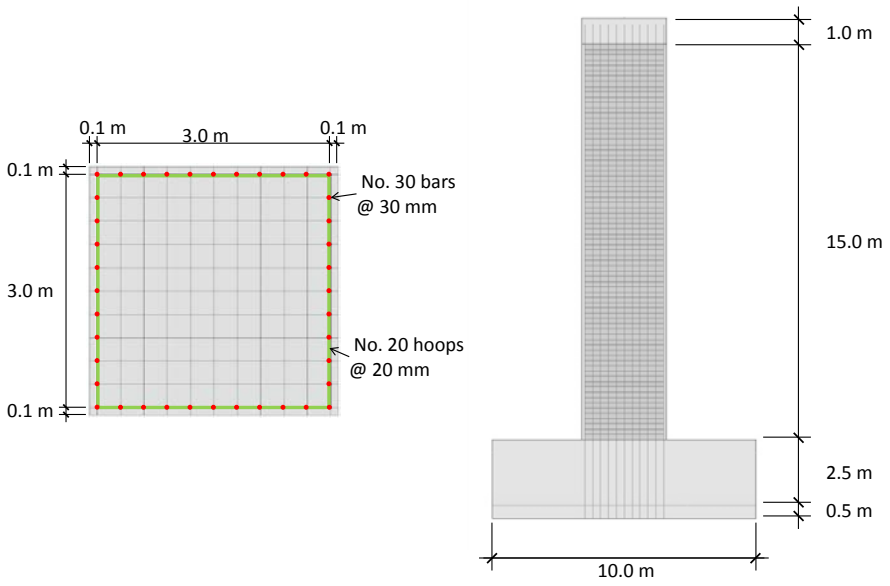

Figure 4.16 Square pier geometry and dimensions

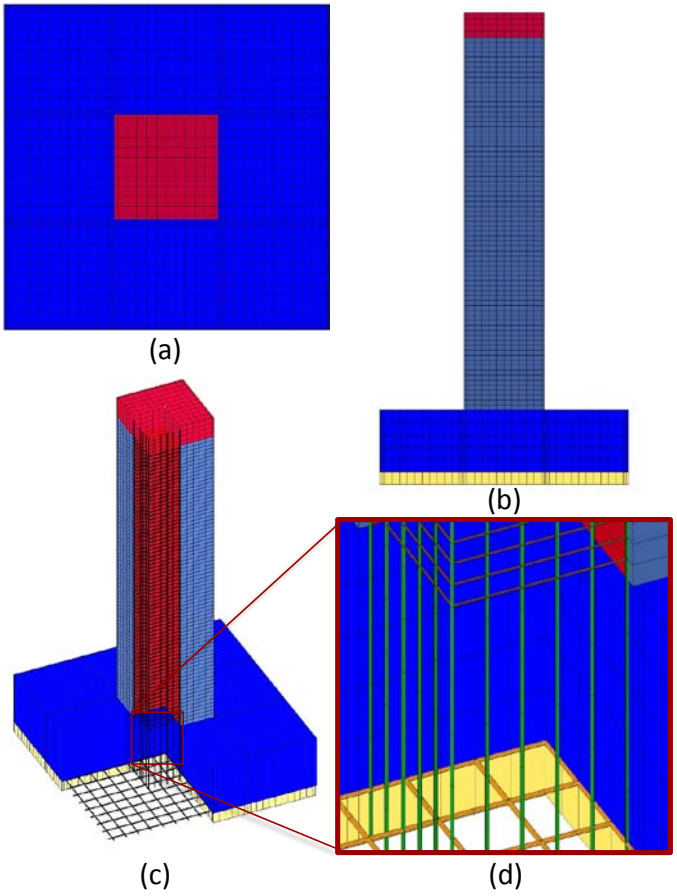

Figure 4.17 Plan (a), elevation (b), isometric cut-through (c), and reinforcement detail (d) of square pier.

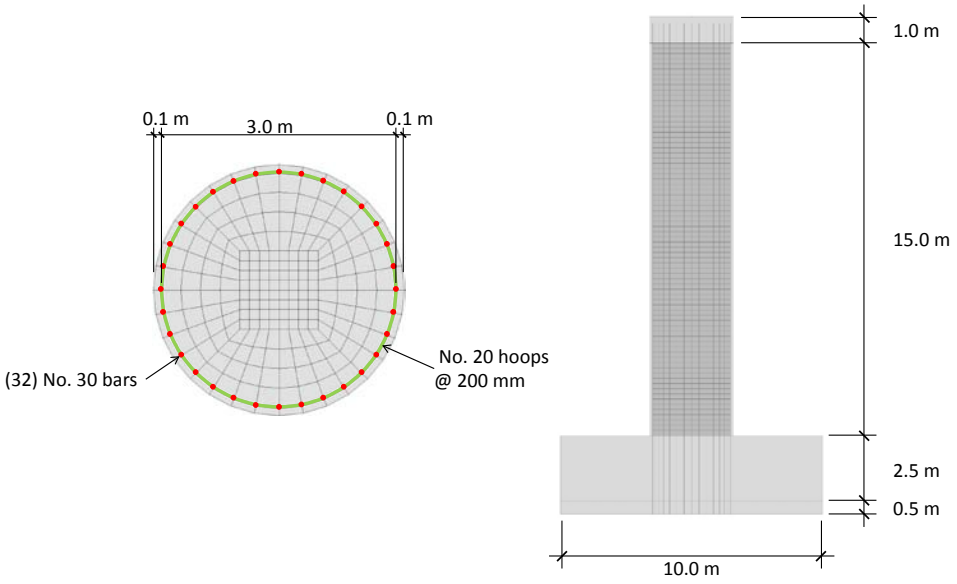

Figure 4.18 Circular pier geometry and dimensions

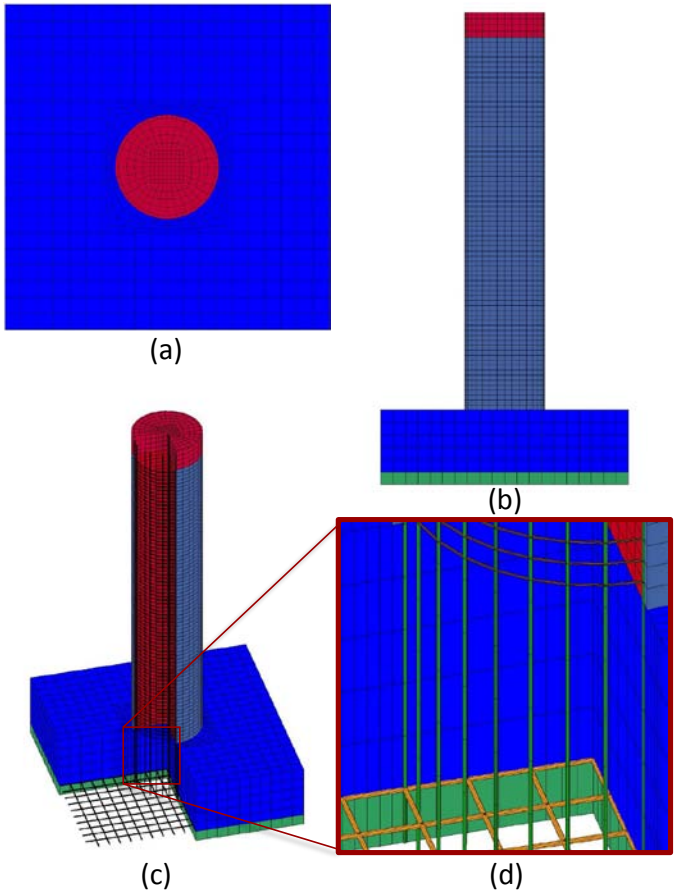

Figure 4.19 Plan (a), elevation (b), isometric cut-through (c), and reinforcement detail (d) of circular pier.

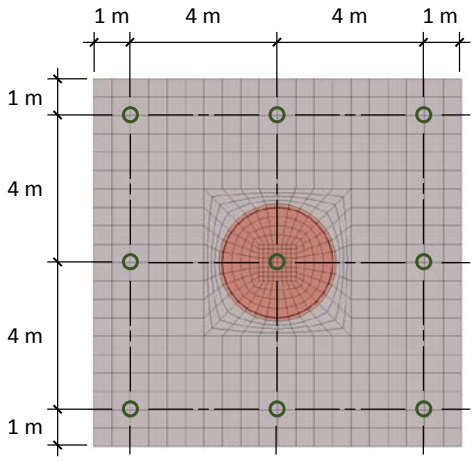

Figure 4.20 Pipe piles locations

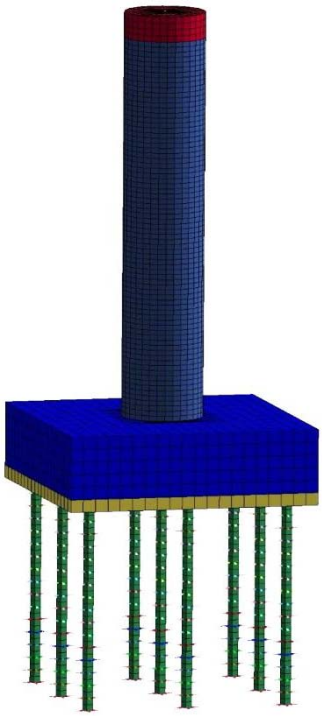

Figure 4.21 Single circular pier with 8 m long pipe piles and soil springs

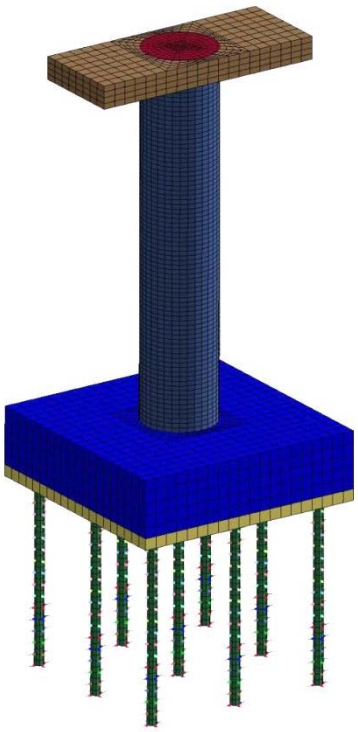

Figure 4.22 Single circular pier with cap beam, 8 m long pipe piles and soil springs

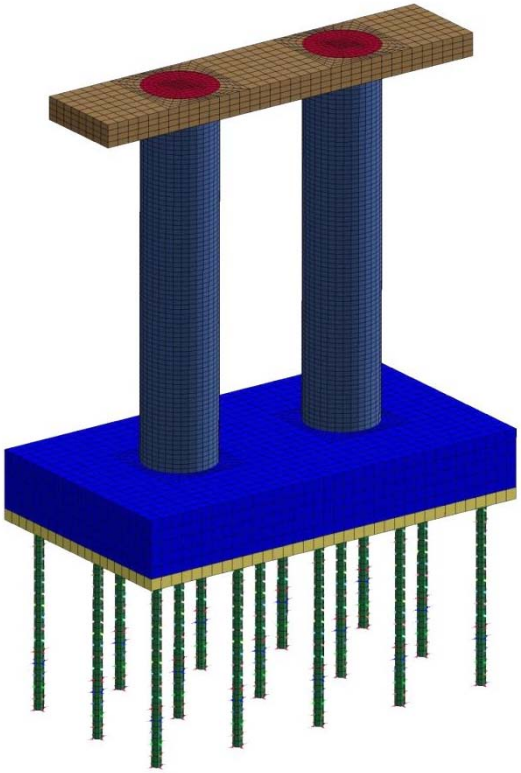

Figure 4.23 Double circular pier with cap beam, 8 m long pipe piles and soil springs

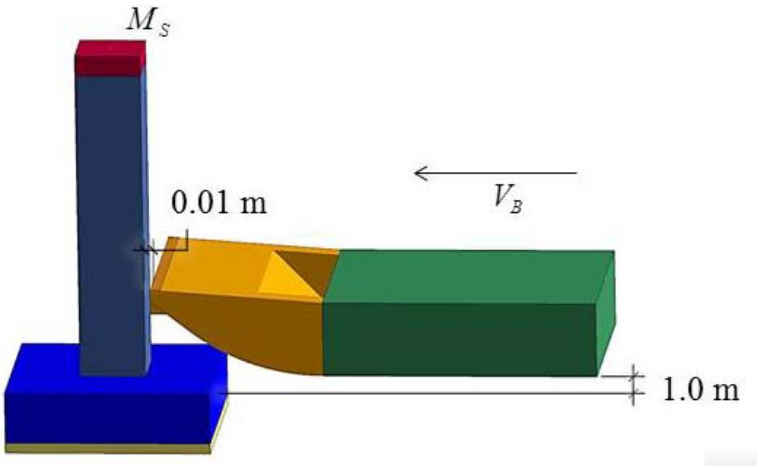

Figure 4.24 Initial setup for all barge pier simulations

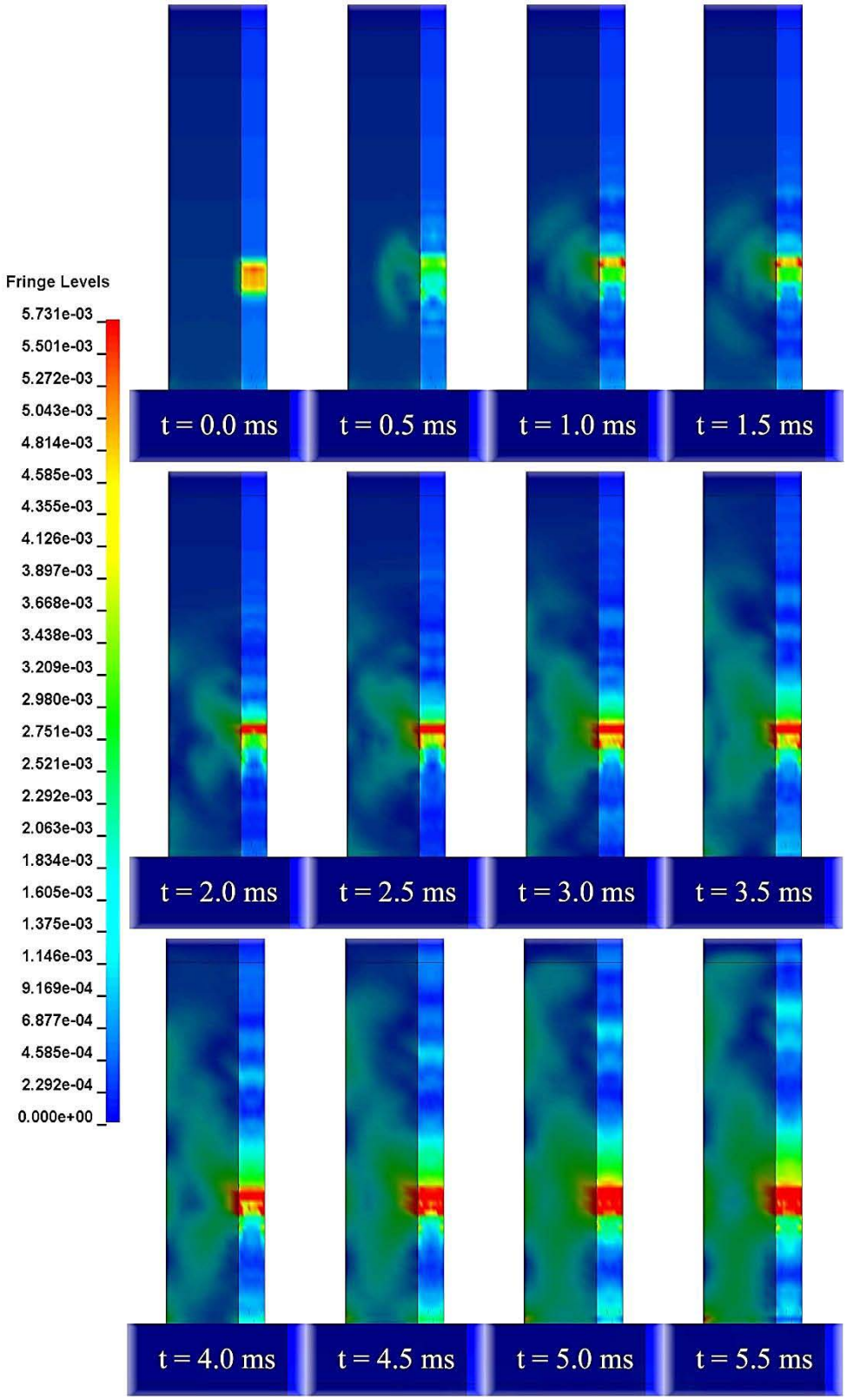

Figure 4.25 Von Mises Stress propagation in first 5.5 ms of impact thorough a square pier

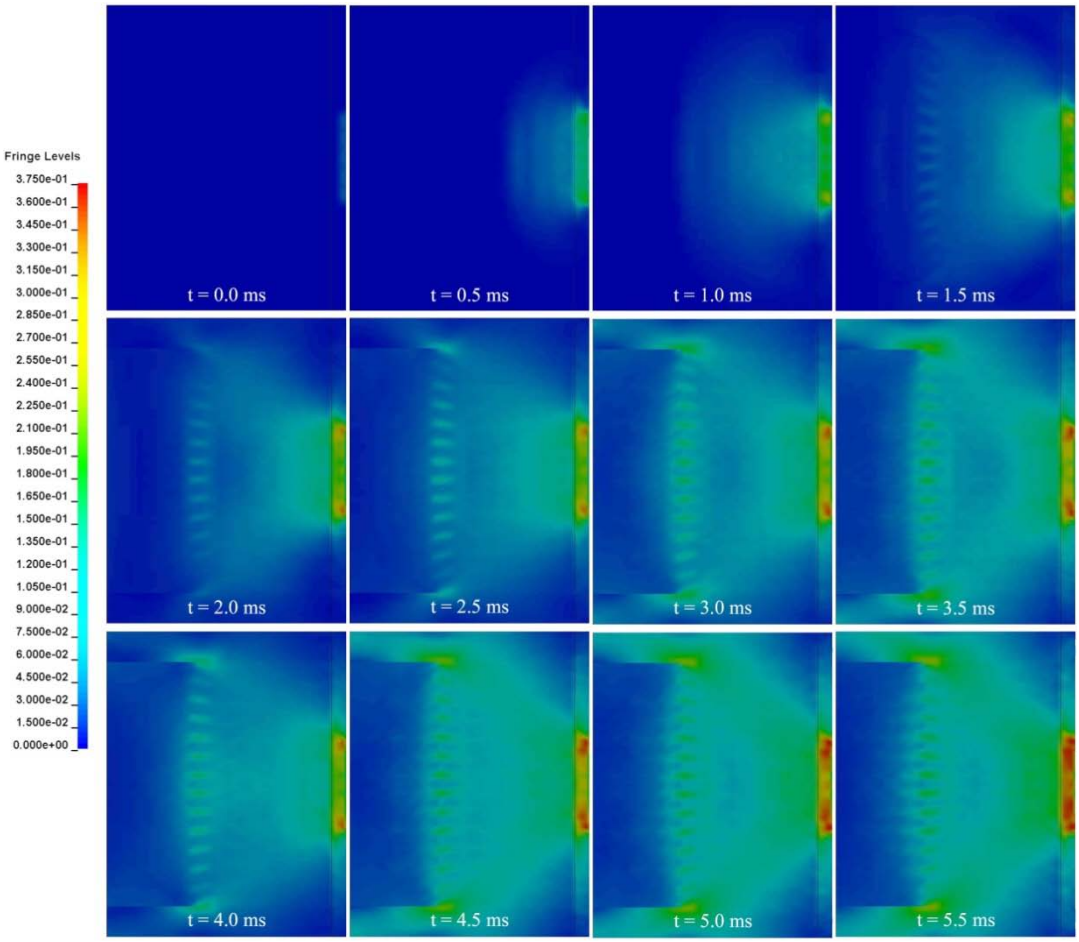

Figure 4.26 Von Mises Stress propagation through barge bow in first 5.5 ms of impact

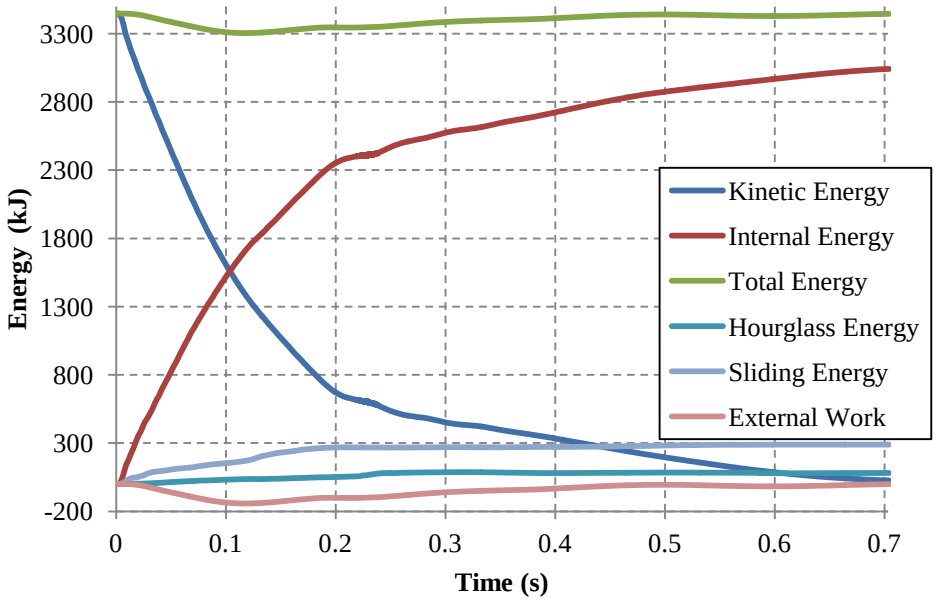

Figure 4.27 Recorded model energy through the duration of simulation

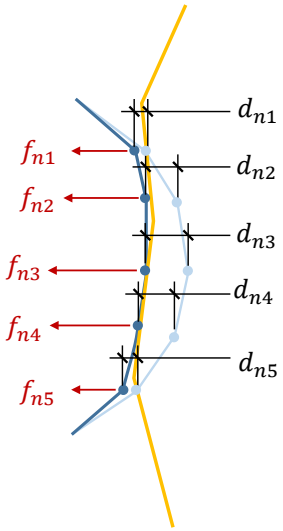

Figure 4.28 Schematic of two bodies in contact illustrating how forces are applied

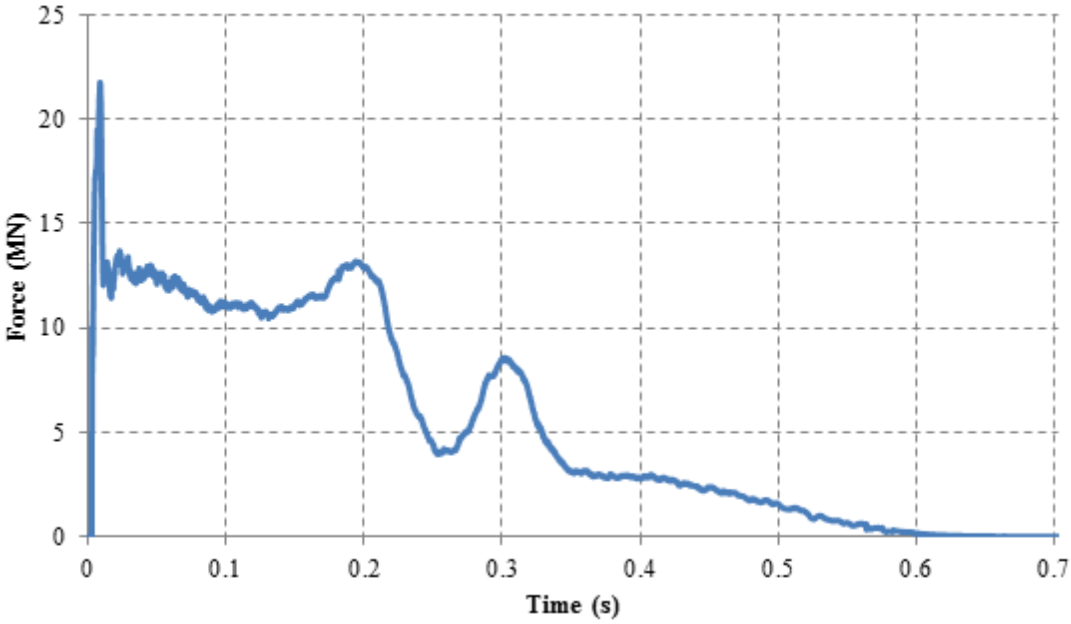

Figure 4.29 Impact force time history of a fully loaded barge traveling at 2 m/s colliding into a square pier supporting a 300 ton mass

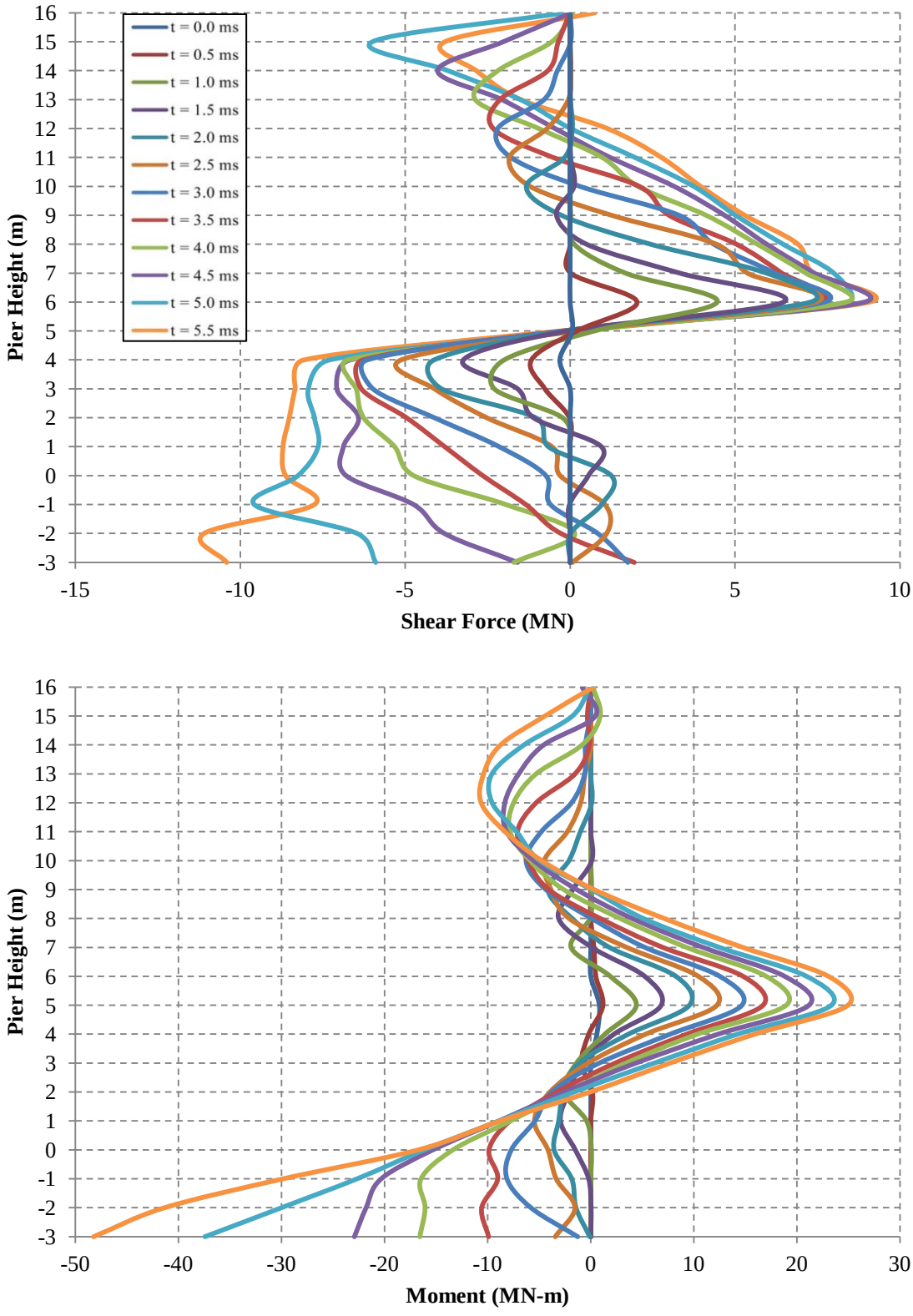

Figure 4.30 Shear and moment diagrams of a square pier supporting a 300 ton mass impacted by a fully loaded barge traveling at 2 m/s

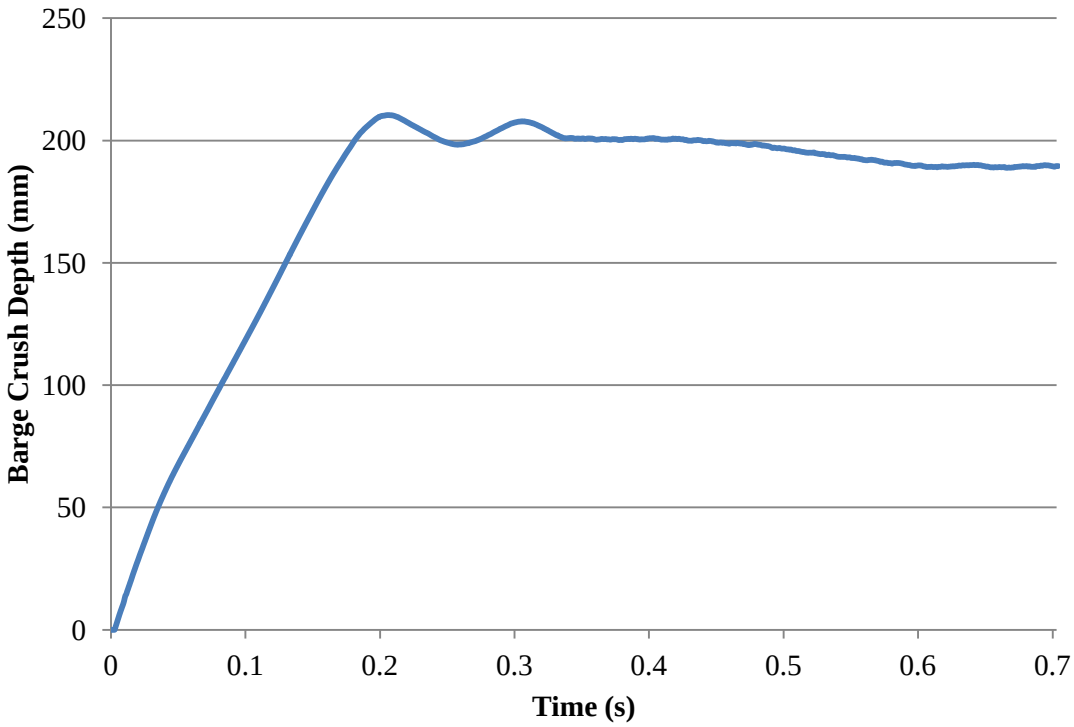

Figure 4.31 Barge bow crush depth of a fully loaded barge traveling at 2 m/s colliding into a fixed square pier supporting a 300 ton mass

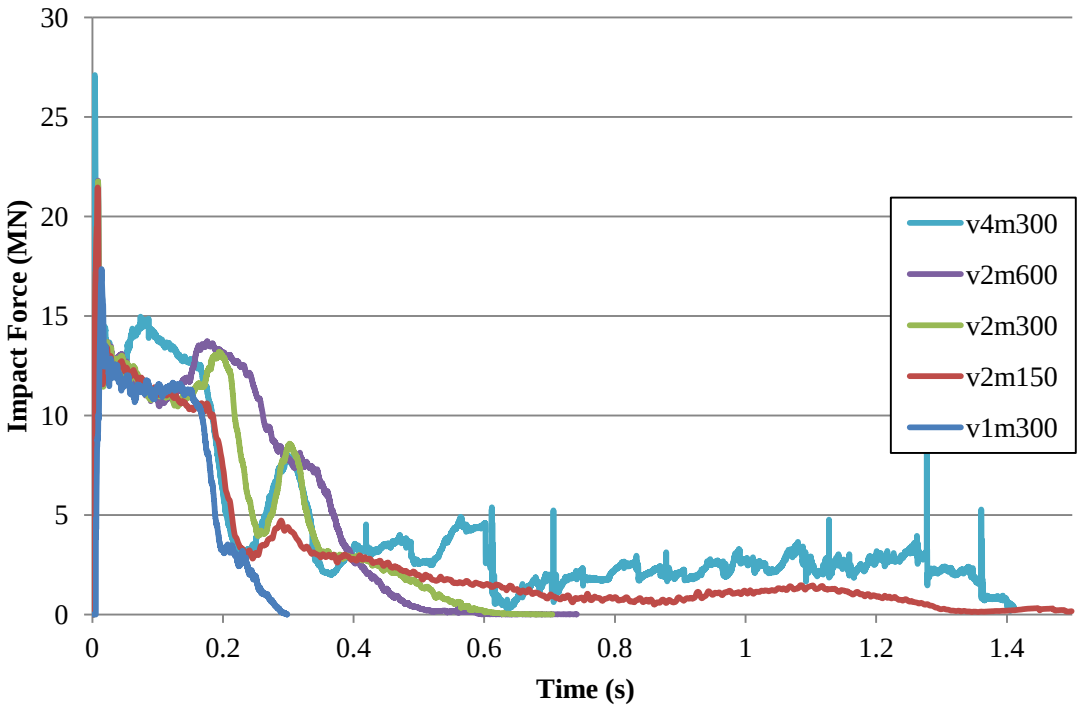

Figure 4.32 Impact force time histories of a fully loaded barge impacting fixed square RC piers

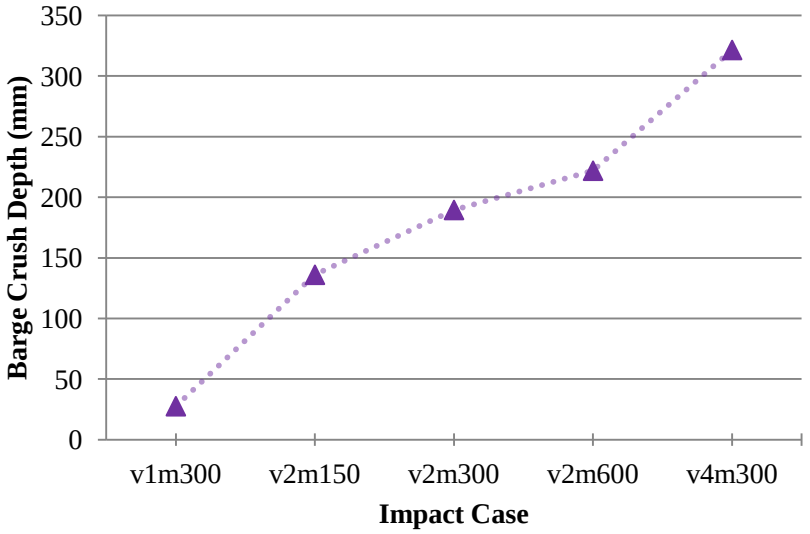

Figure 4.33 Summary of barge crush depth for five impact cases with fixed a square pier

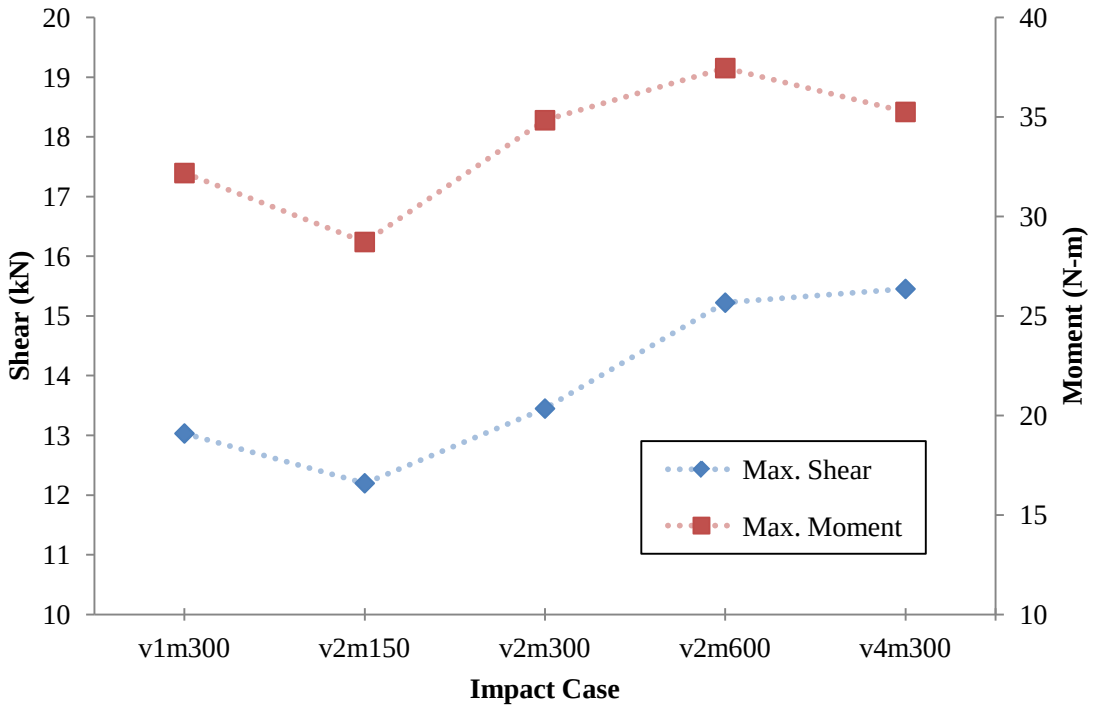

Figure 4.34 Summary of maximum shear and moment in a fixed square pier for five impact cases

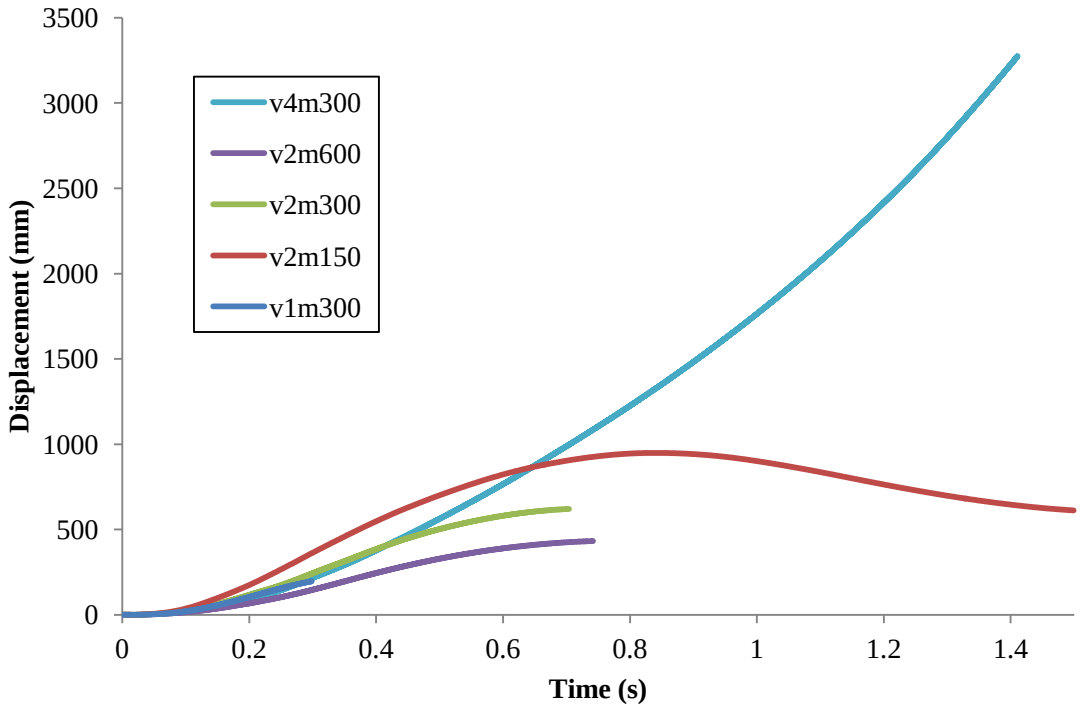

Figure 4.35 Displacement time histories of the top of the pier with a square cross-section and a fixed foundation for five different impact cases

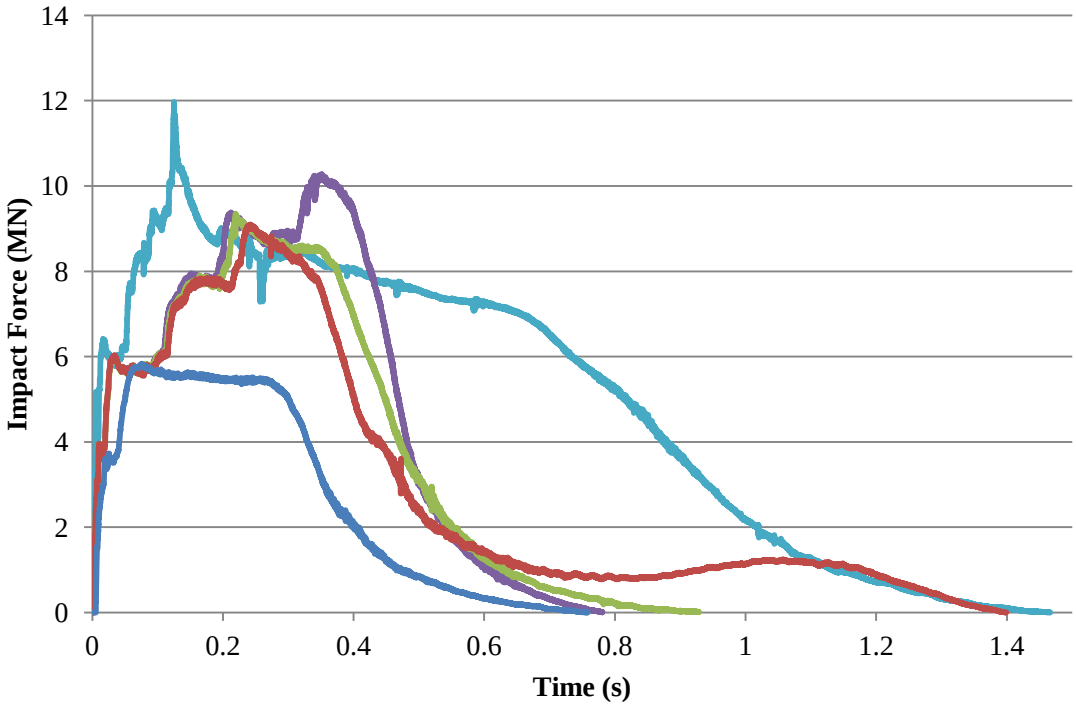

Figure 4.36 Impact force time-histories of a fully loaded barge impacting fixed circular RC piers

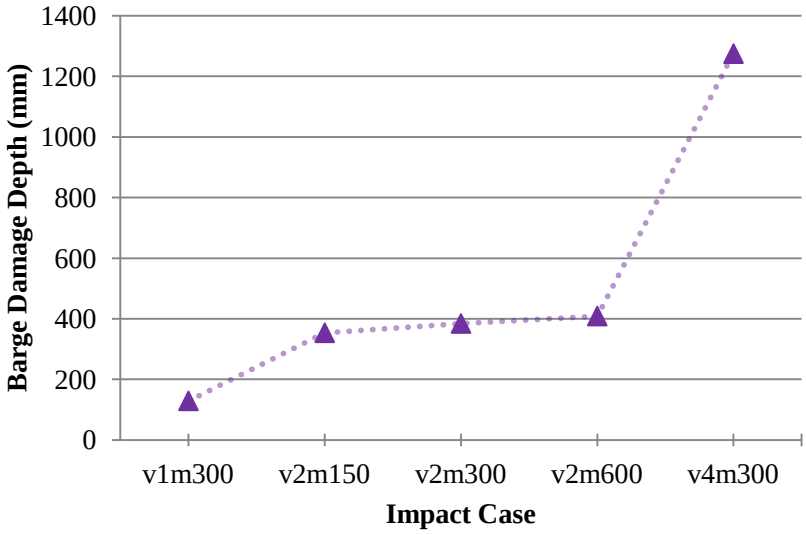

Figure 4.37 Summary of barge crush depth for five impact cases with a fixed circular pier

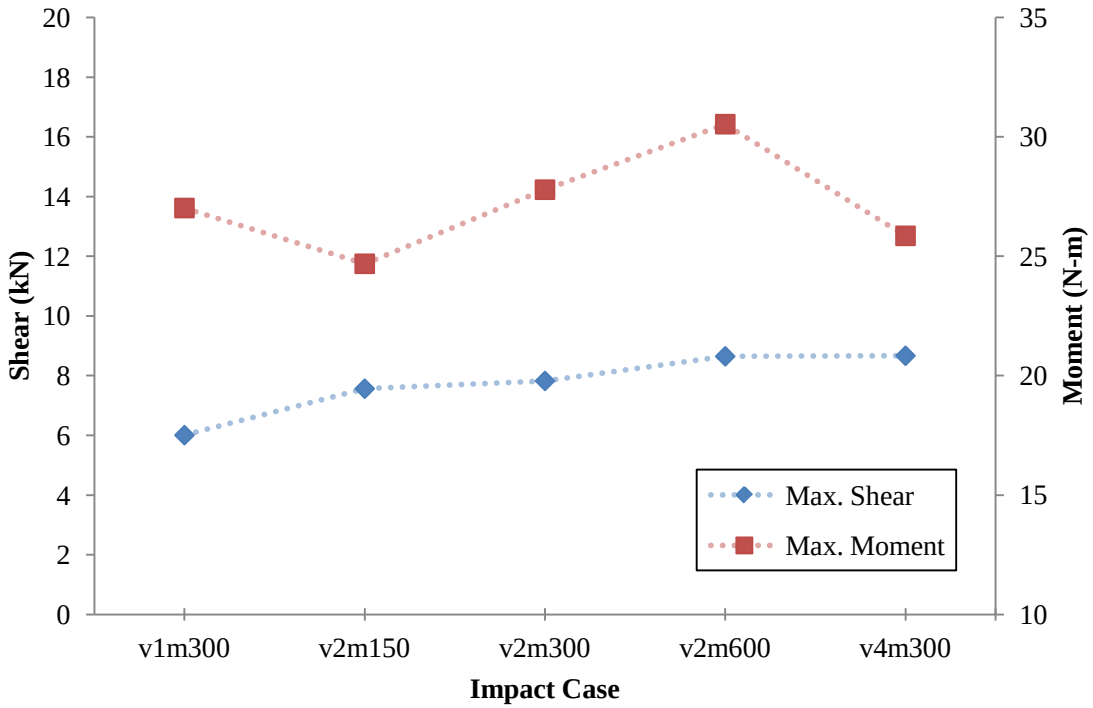

Figure 4.38 Summary of maximum shear and moment in a fixed circular pier for five impact cases

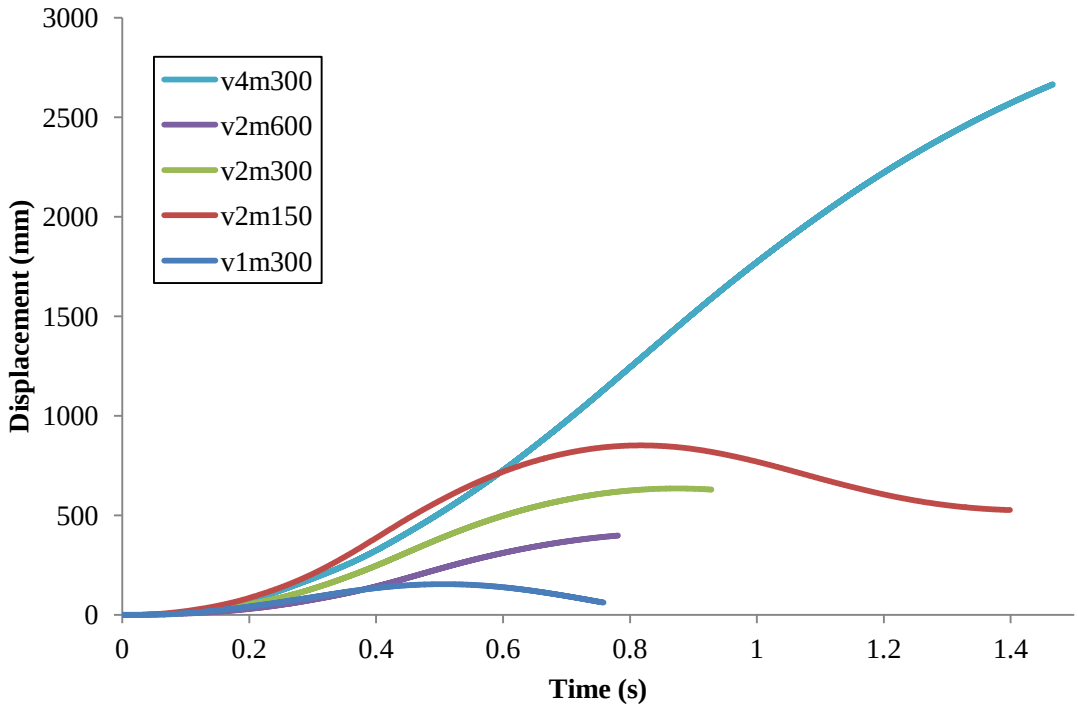

Figure 4.39 Displacement time histories of the top of the pier for five different impact cases with a fixed circular pier

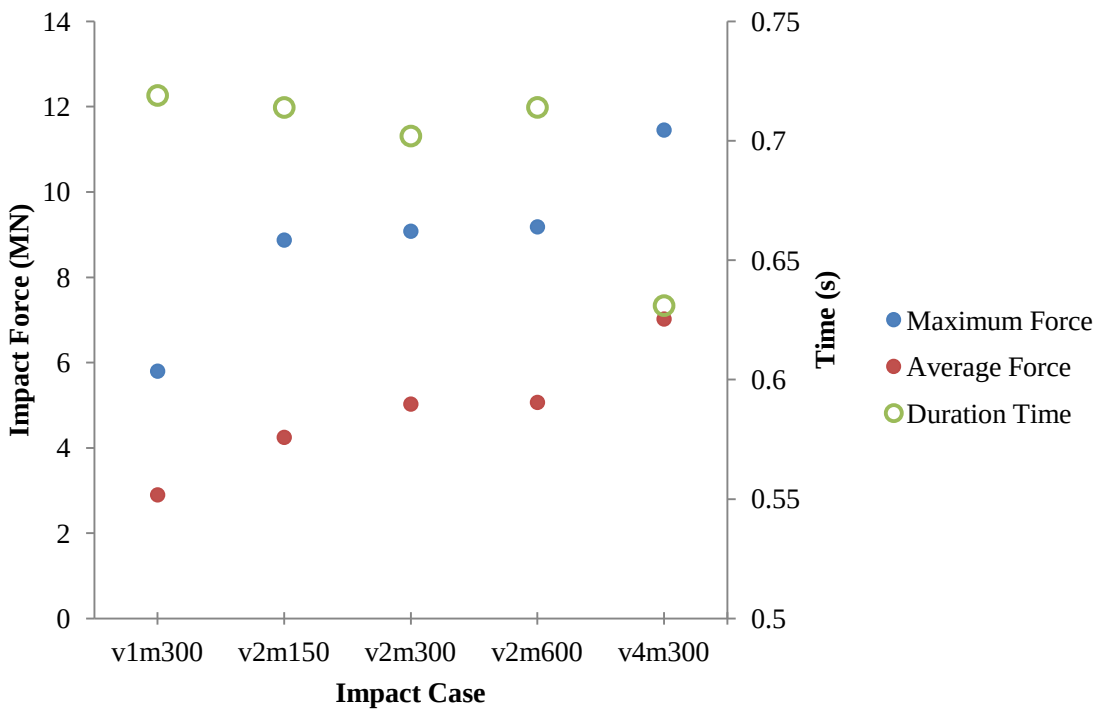

Figure 4.40 Summary of the impact force time histories of five impact cases with a pile supported circular pier

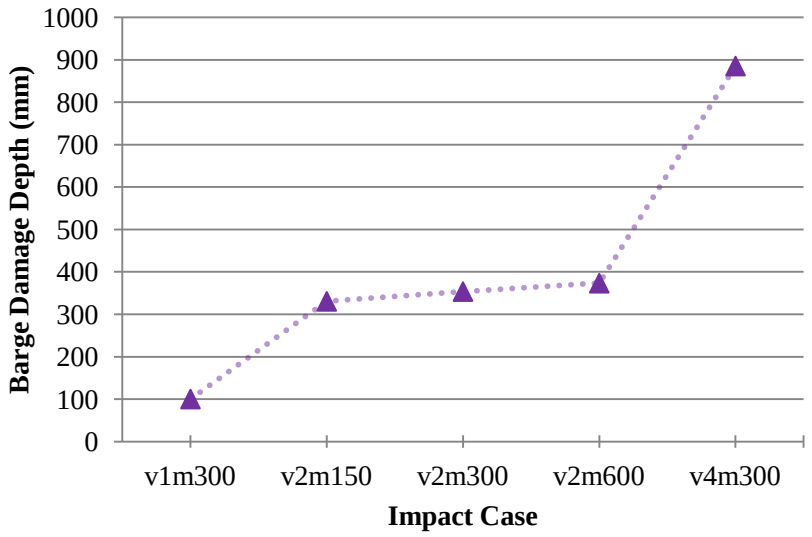

Figure 4.41 Summary of barge crush depth for five impact cases with pile supported circular pier

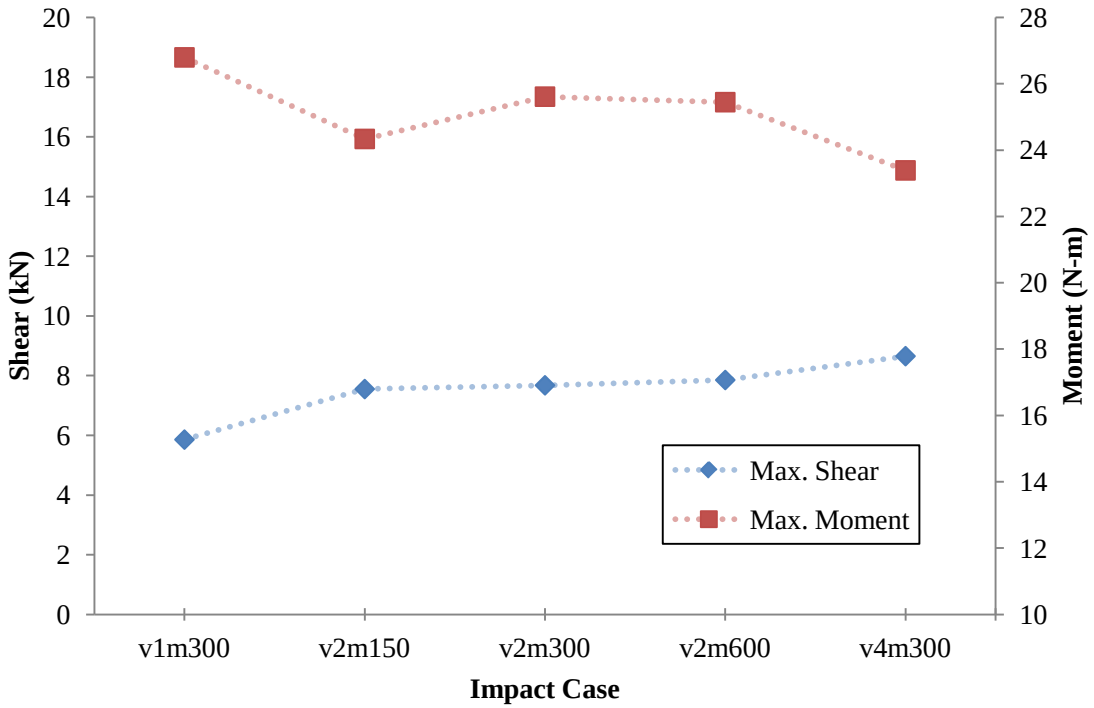

Figure 4.42 Summary of maximum shear and moment in a pile supported circular pier for five impact cases

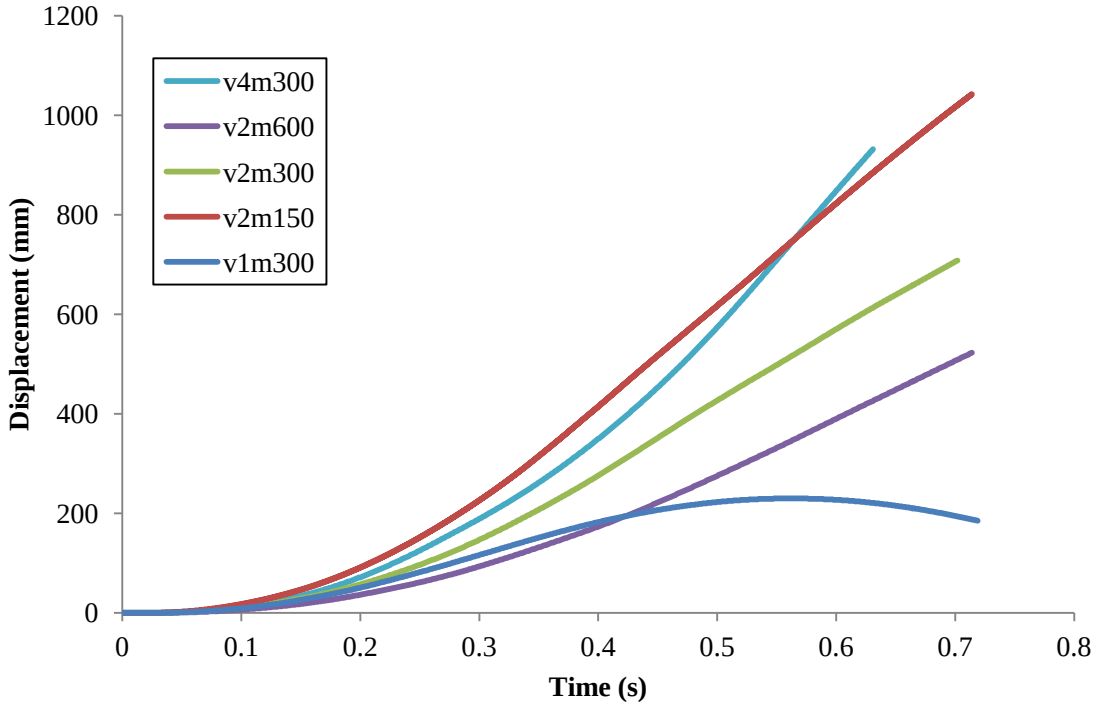

Figure 4.43 Displacement time histories of the top of the pier for five different impact cases with a circular pier supported by piles

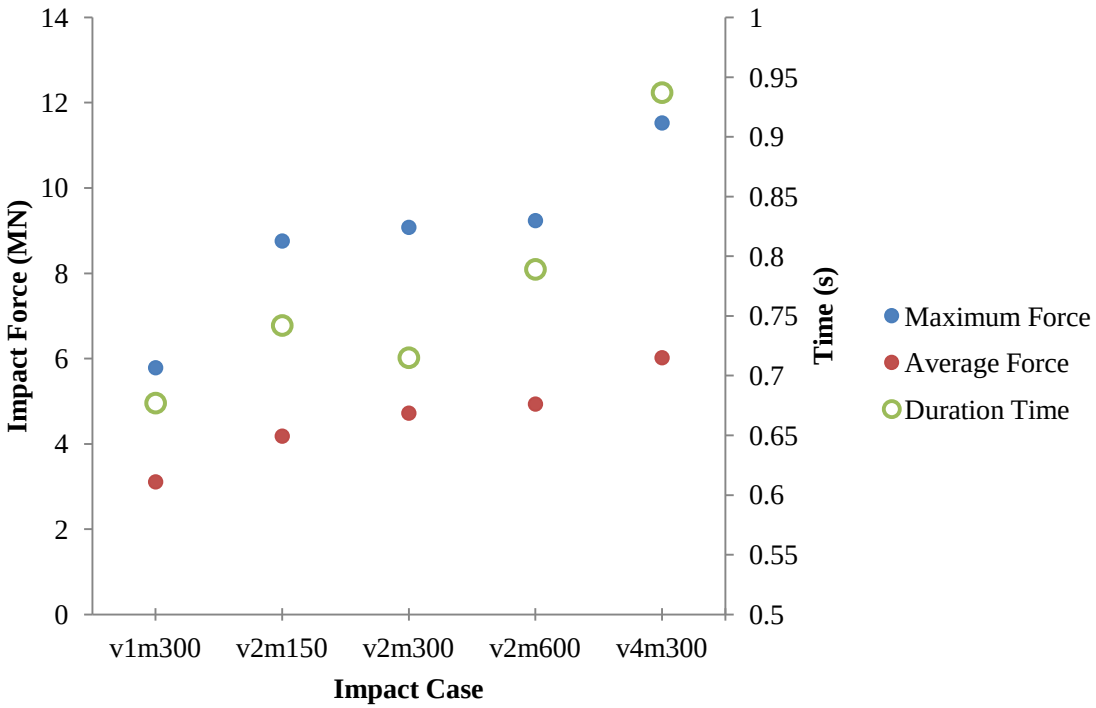

Figure 4.44 Summary of the impact force time-histories of five impact cases with a pile supported circular pier with cap beam

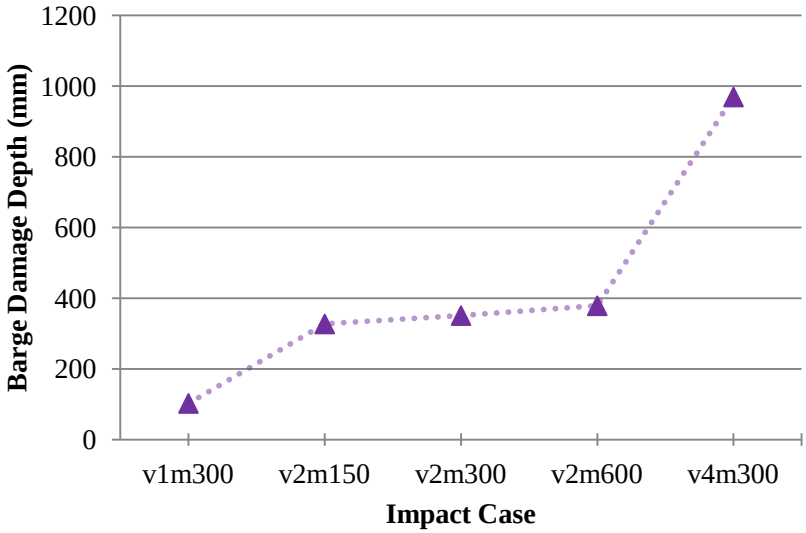

Figure 4.45 Summary of barge crush depth for five impact cases with pile supported circular pier with cap beam

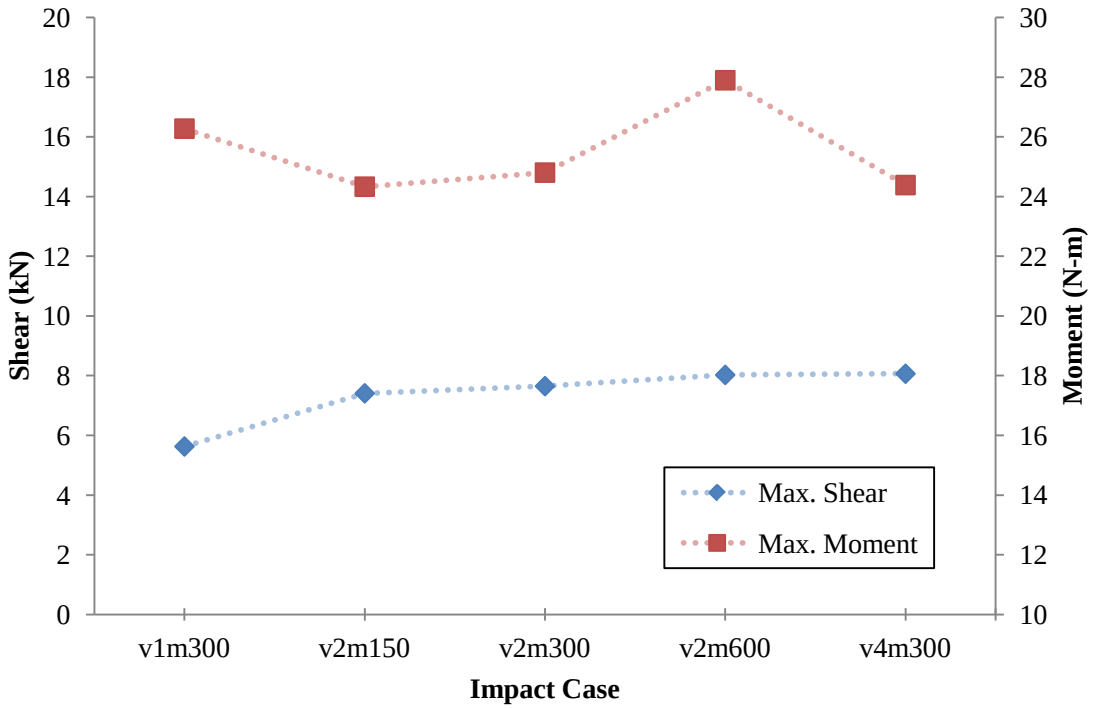

Figure 4.46 Summary of maximum shear and moment in a pile supported circular pier with cap beam for five impact cases

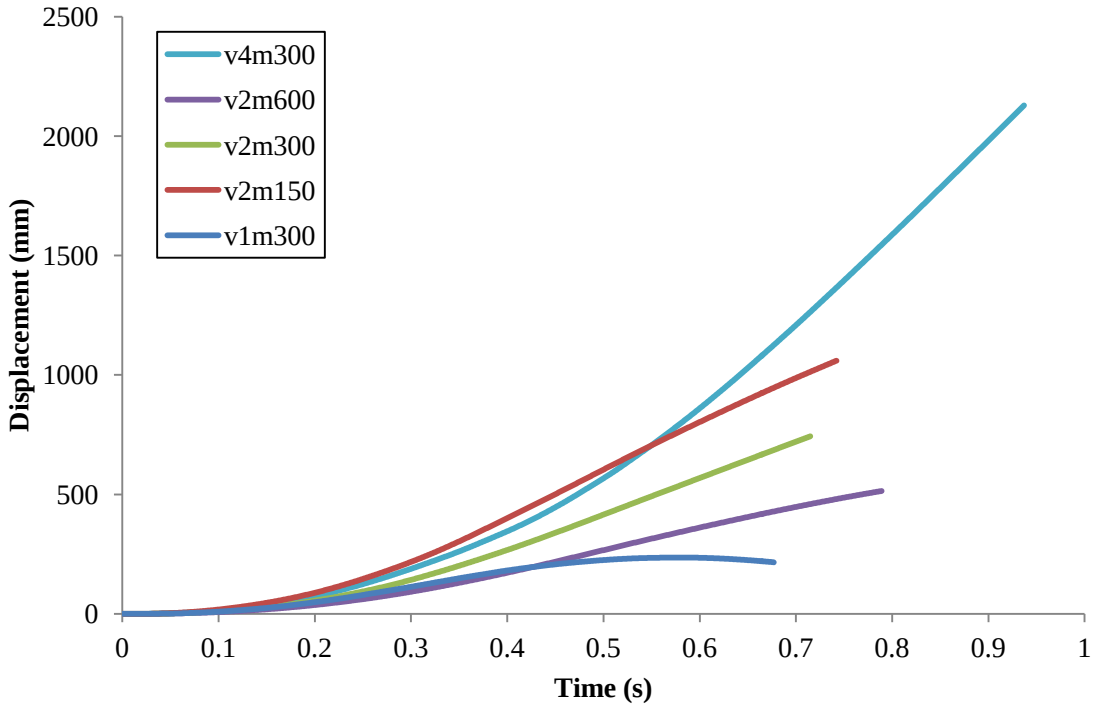

Figure 4.47 Displacement time histories of the top of the pier for five different impact cases with a circular pier with cap beam supported by piles

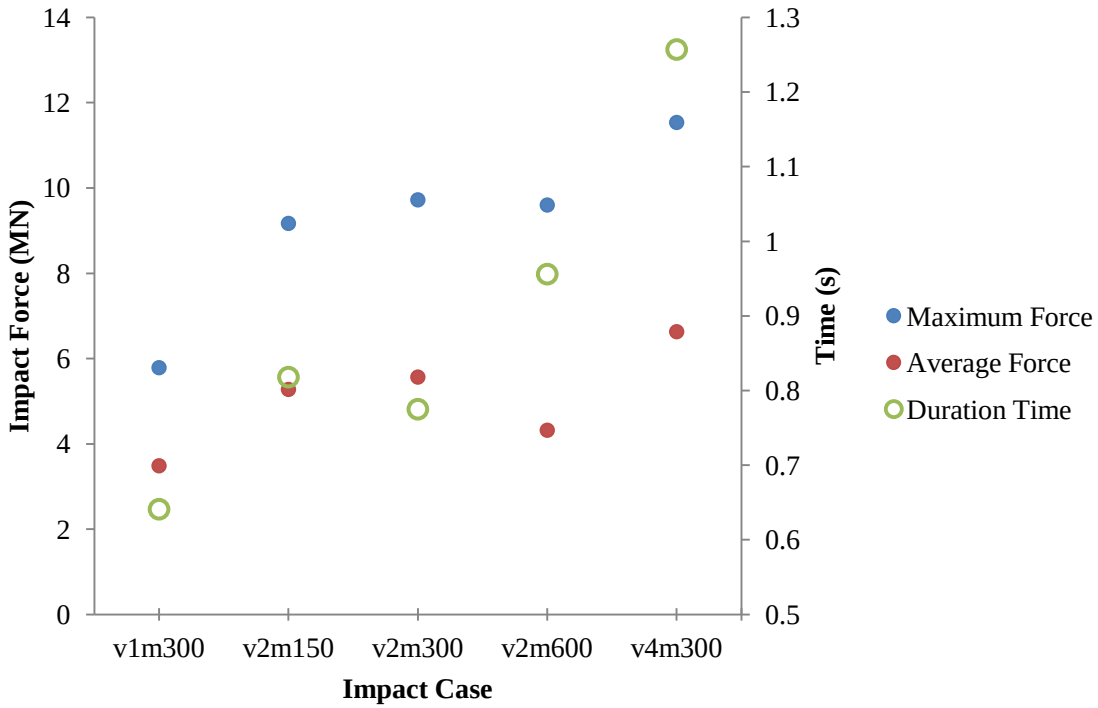

Figure 4.48 Summary of the impact force time histories of five impact cases with a circular double column pier supported by a pile foundation

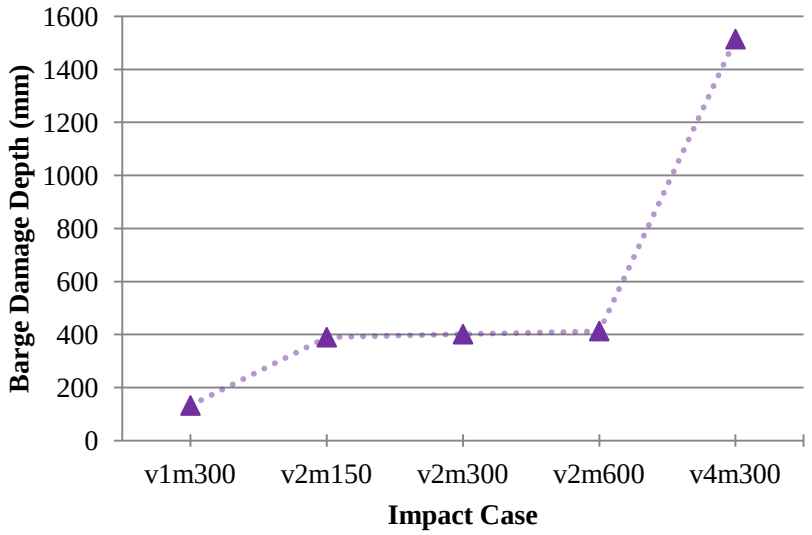

Figure 4.49 Summary of barge crush depth for five impact cases with a circular double column pier supported by a pile foundation

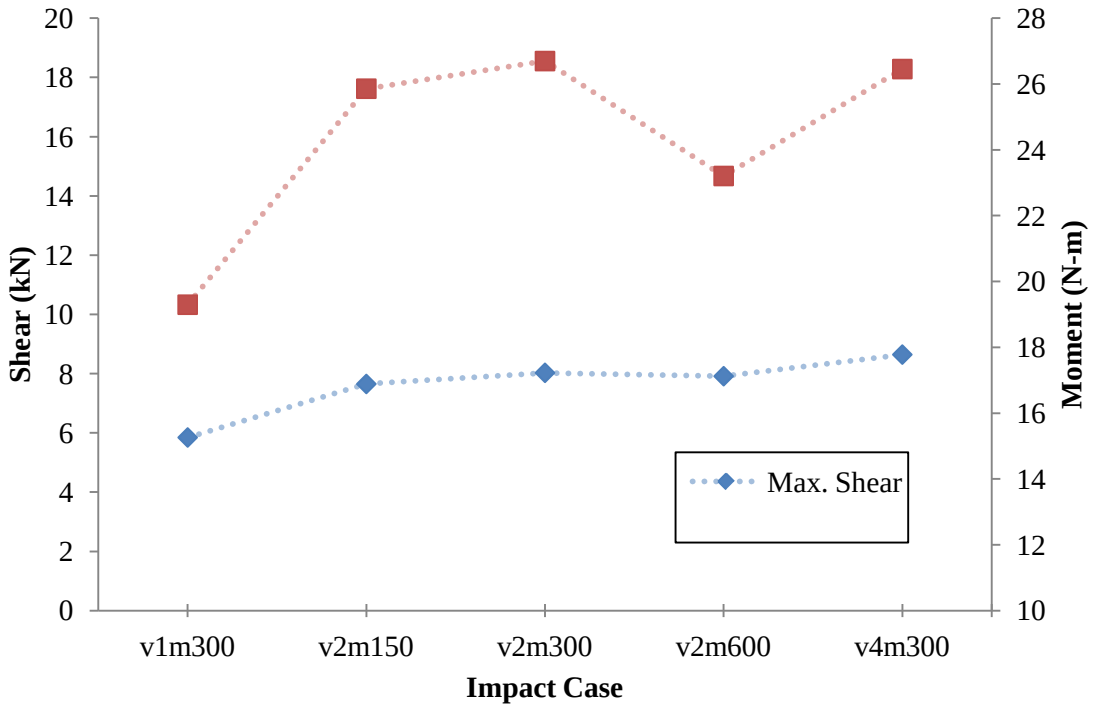

Figure 4.50 Summary of maximum shear and moment in a circular double column pier with a pile foundation for five impact cases

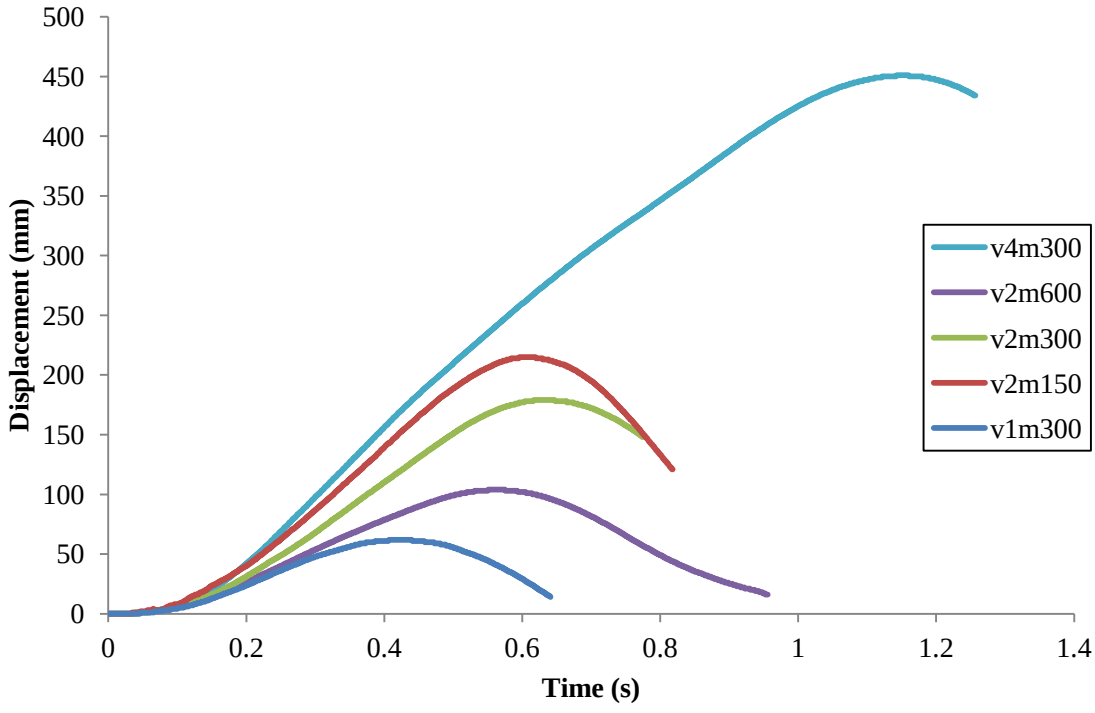

Figure 4.51 Displacement time histories of the top of the pier for five different impact cases of a circular double column pier with a pile foundation

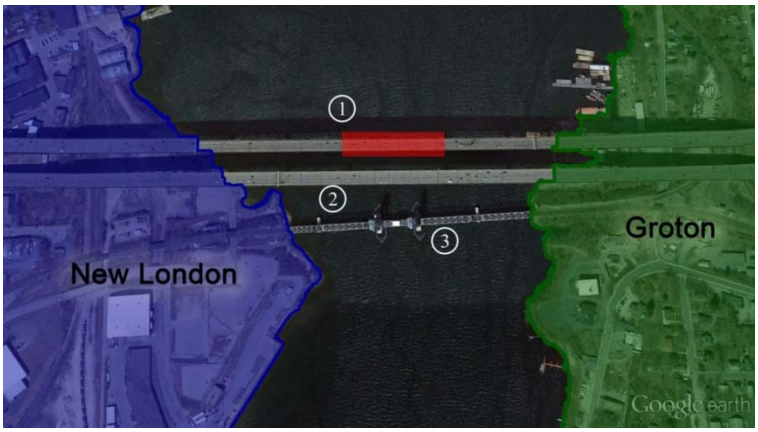

Figure 4.52 Location of the Goldstar Memorial Bridge in Connecticut

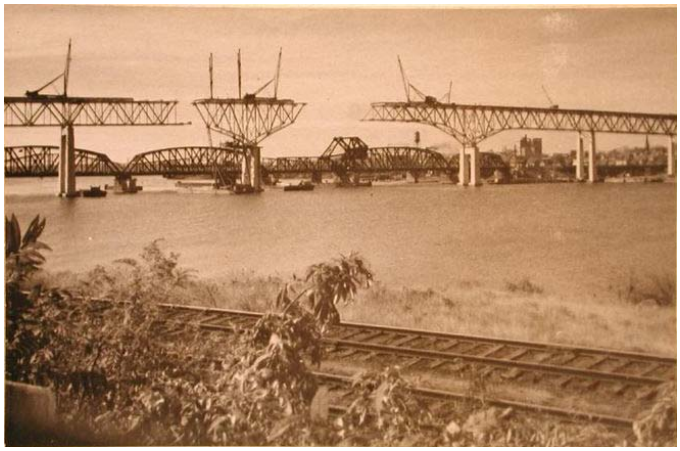

Figure 4.53 Historical photograph of the construction of the first bridge currently the northbound lane (http://emuseum.chs.org/emuseum/media)

Figure 4.54 Mid-span piers of both bridges, with Pier 22/23 supporting roadway on right (http://www.panoramio.com)

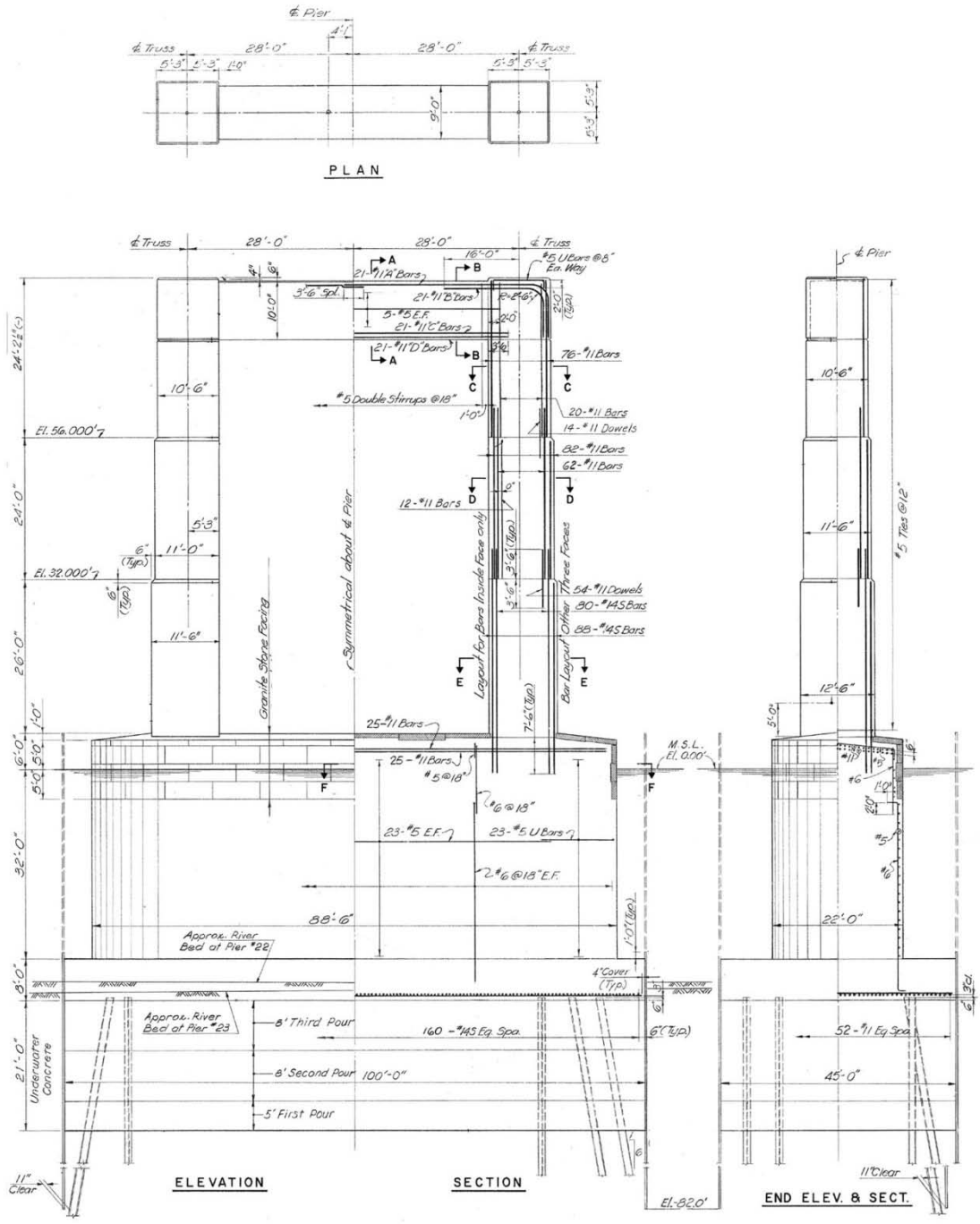

Figure 4.55 Selected construction drawings showing general dimensions and specifications of Pier 22/23

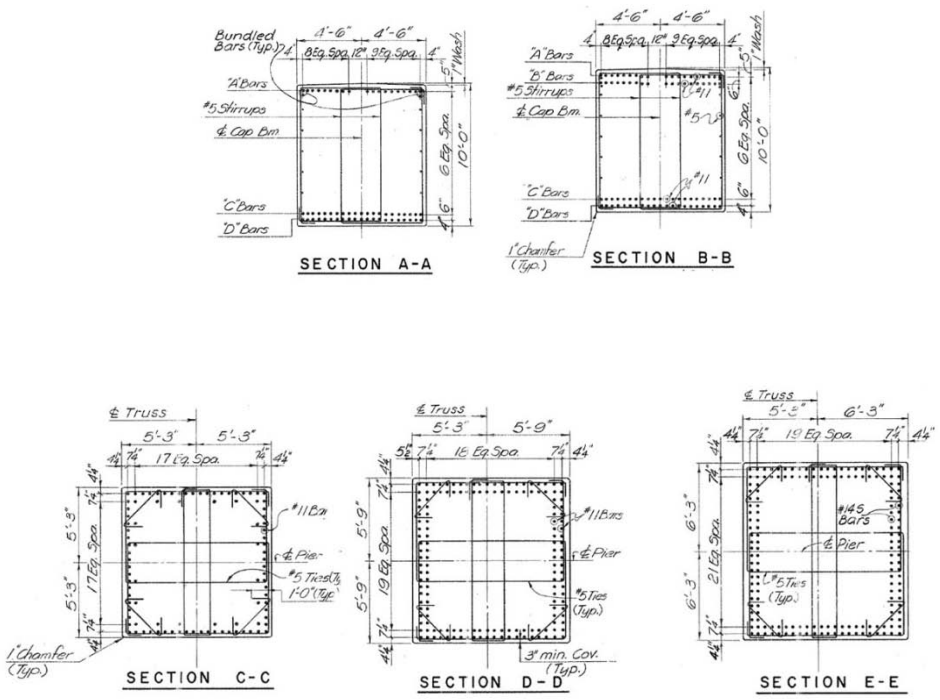

Figure 4.56 Sections of Pier 22/23 form construction drawings

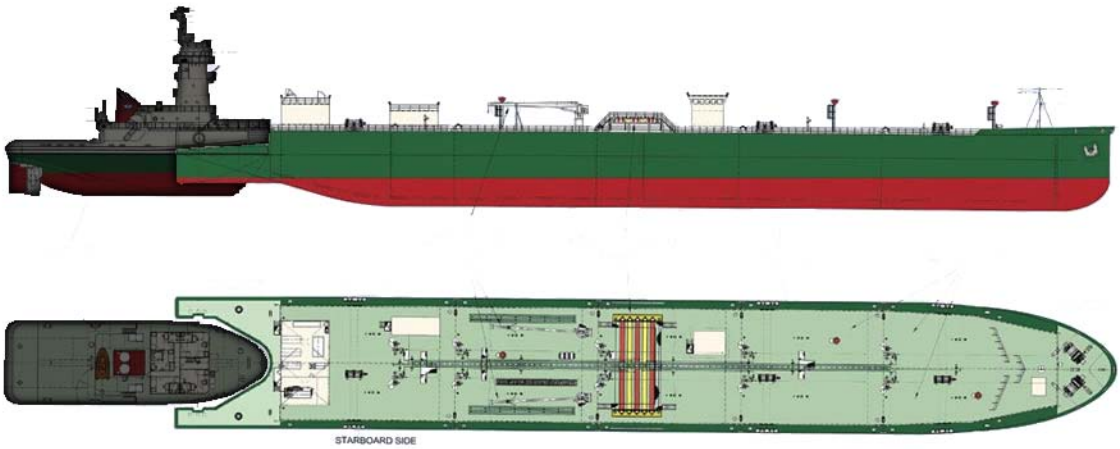

Figure 4.57 Diagram of the ATB Freeport from the U.S. Shipping Corp.

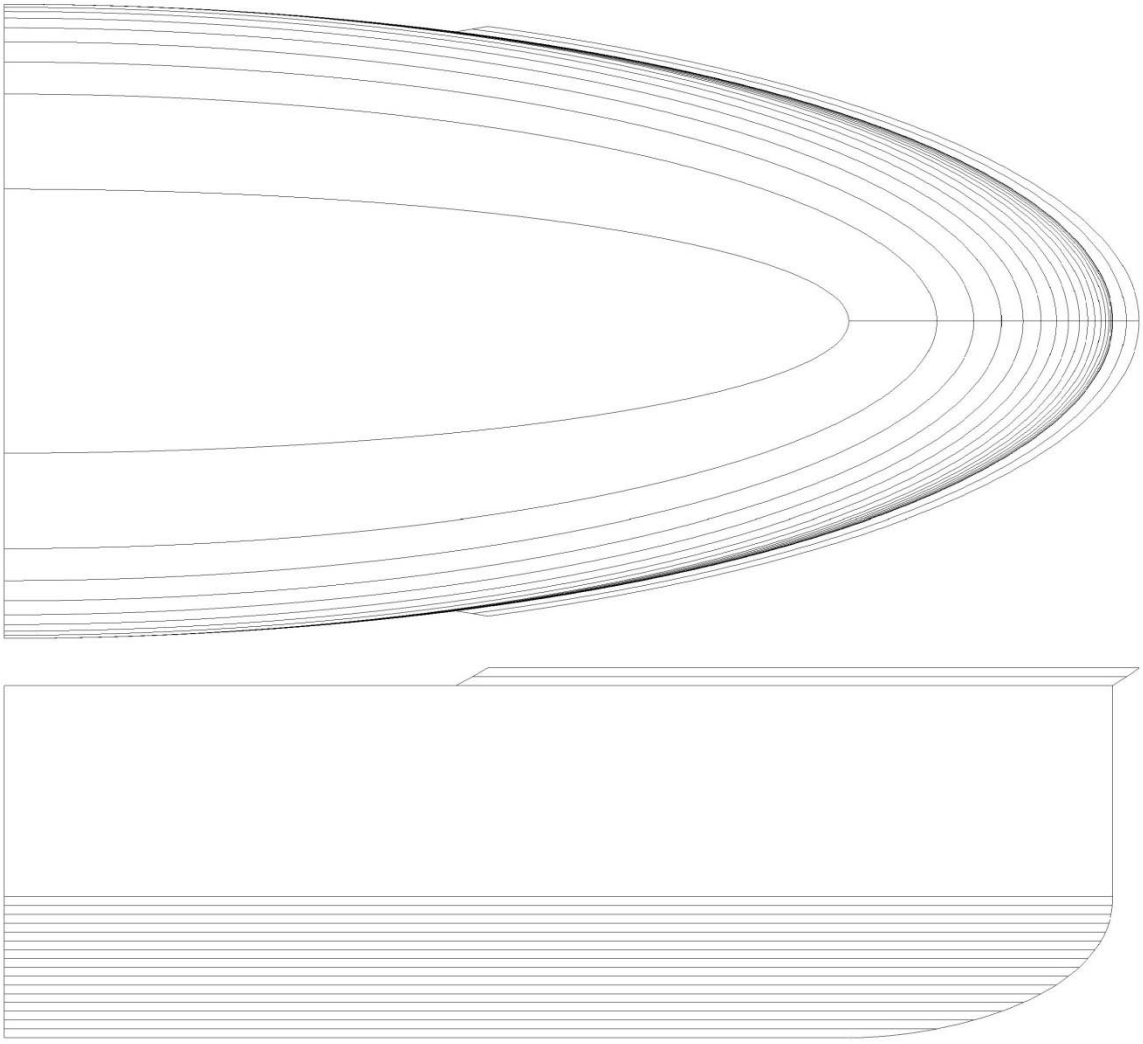

Figure 4.58 Elliptical isolines shown in plan (top) and elevation (bottom) used to compose the shape of the hull of ATB Freeport barge

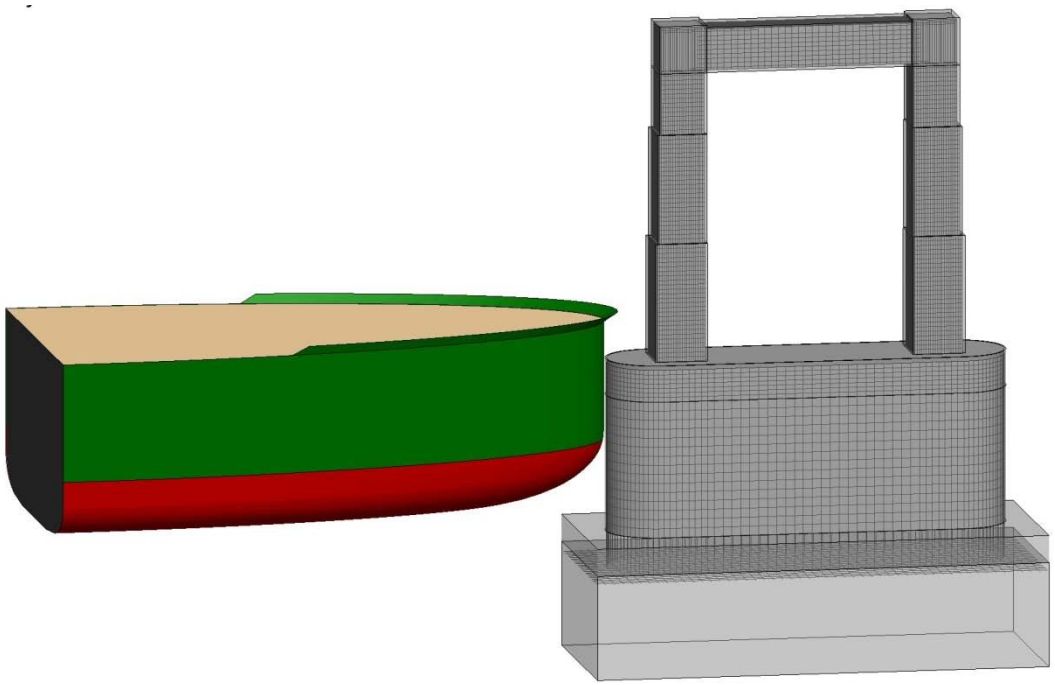

Figure 4.59 Model setup with rigid barge impactor and detailed RC model of Pier 22/23

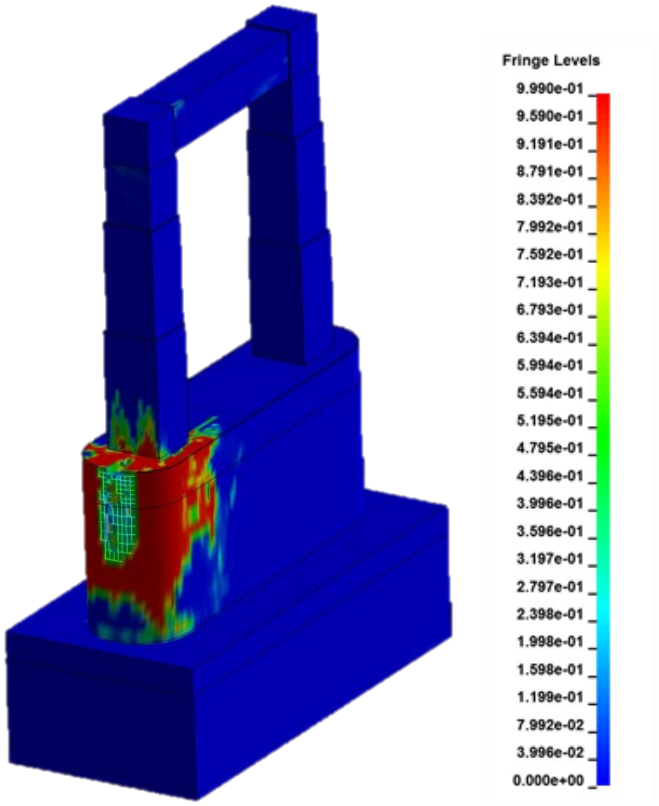

Figure 4.60 Plastic strain fringe predicting damage levels on the contact face at the end of the simulation

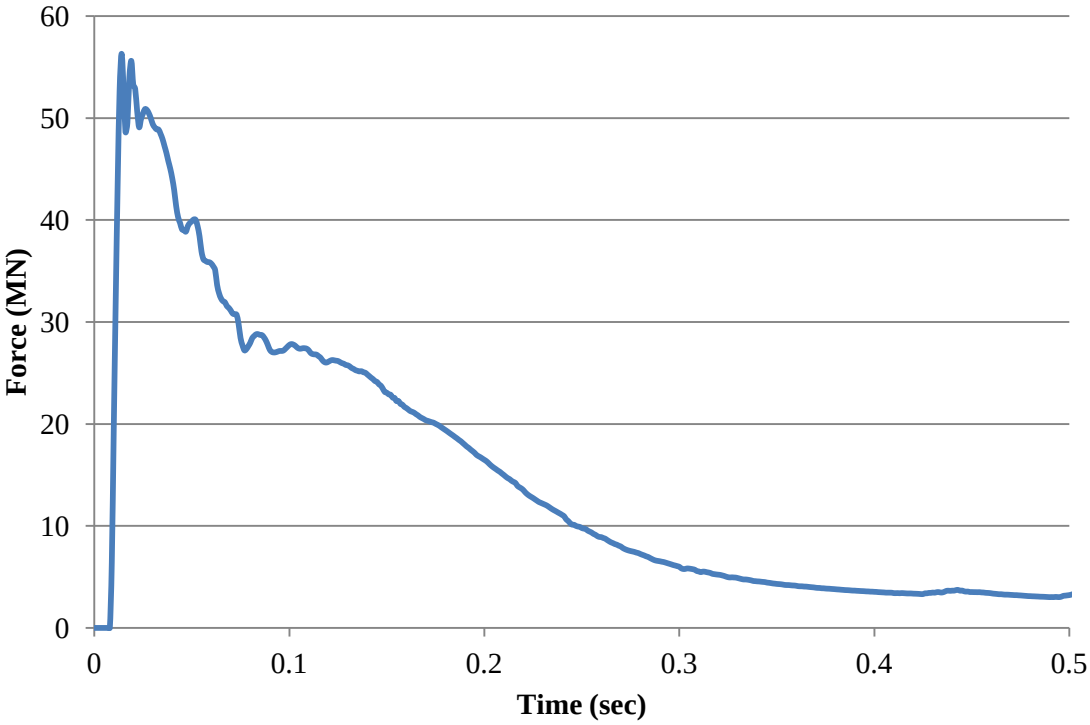

Figure 4.61 Force time history of rigid Freeport barge impacting Pier 22/23

CHAPTER 6

CONCLUSIONS

The previous research efforts on barge impact have drawn attention to the shortcomings of the current AASHTO design specifications, which prescribe barge impact forces. The specifications assign conservative design forces in the form of static loads, which does not allow for the dynamic interaction of the barge and a bridge column. Such a static simplification cannot appropriately capture the highly dynamic nature of an impact that can be critical to the design.

In the present study, the impact of a jumbo hopper barge into concrete piers is investigated. The finite element analysis solver, LS-DYNA, was used to perform the 3D simulations. An investigation of the CSCM concrete model has been performed in a drop hammer impact study of a doubly reinforced concrete beam. This material model was originally developed for roadside safety structures and has been noted by the developers to be able to handle impact loading scenarios. In addition, KC concrete has been examined in this study.

The CSCM concrete material model developed the appropriate forces expected in the drop hammer tests. Parameters were tested to investigate their influence on the overall outcome on the impact force and deformation curves. Hourglass was determined to be an influential parameter to fine tune the results. If too much hourglass was applied to the material, instability and unexpected damage would occur in the concrete. Overall, this material model was capable of carrying out the impact cases with confidence and was chosen for the second stage of this work.

The KC concrete model was also studied for parametric influences. This material model has a built-in model based on a select number of parameters. The sensitivity study showed that parameters such as Poisson's ratio and density result in unsubstantial differences in forces or deformations. KC concrete is capable of producing approximate results when compared to the expected results.

The second part of the study examined, more particularly the collision event between a barge and a reinforced concrete pier. The section covered the detail of the jumbo hopper barge model that was used for the RC pier impacts. Before exploring the response of RC piers, the barge model was evaluated by conducting several impacts into rigid piers. Through this study, the impact force induced onto the pier was greatly affected by the shape and sized of the pier section. Square piers resulted in an impact force time history that was characteristically different than that from an impact into circular piers. The square piers resulted in a sharp rise to the peak impact force followed by a significantly reduced force that tampered until the end of the simulation. Whereas circular piers had a monotonic increase of the impact force that quickly drops to the end of the impact. Overall, the impact forces developed by circular piers were significantly less than those introduced by impacts with the square piers. The barge bow damage was also very much influenced by pier the barge impacted. It was seen that the barge crush depth changed depending on the pier size for square piers. However, this was not as distinctly prominent for impact into circular piers.

The barge was then placed to impact RC piers head-on. A square and equivalent circular RC pier was selected as the base models used for the impact. For all the pier geometries in this study, a selected combination of different barge velocities and masses

supported by the pier were examined. The series of investigations begins by looking at the case where the foundations are fixed for both the square and circular piers. Comparing to the impacts of the barge into the rigid piers, similar characteristic impact forces were observed for each barge shape. Assessing the vulnerability of bridge piers included several metrics, such as the impact force, shear, moment, displacement of the top of the pier, and the bow damage depth. The final part of the thesis discussed the simulation of an impact to a mid-span pier of the Goldstar Memorial Bridge in Connecticut. In this case, the structural vulnerability of a selected bridge pier was investigated under an impact by the chemical transporter that travels up and down the waterway that the bridge spans.

REFERENCES

AASHTO. (2009). *Guidel specifications and commentary for vessel collision design of highway bridges.* American Association of State Highway and Transportation Officials.

ACI Committee 318. (2008). *Building code requirements for structural concrete (ACI 318-11) and commentary.* Farmington Hills, MI: American Concrete Institute.

Adhikary, S. D., Li, B., & Fujikake, K. (2012). Dynamic behavior of reinforced concrete beams under varying rates of concentrated loading. *International Journal of Impact Engineering, 47,* 24-38.

Adhikary, S. D., Li, B., & Fujikake, K. (2013). Strength and behavior in shear of reinforces concrete deep beams under dynamic loading. *Nuclear Engineering and Design, 259,* 14-28.

Arroyo, J. R., & Ebeling, R. M. (2005). *Barge train maximum impact forces using limit states for the lashings between barges.* Washington, DC: U.S. Army Engineer Research and Development Center.

Bischoff, P. H., & Perry, S. H. (1995). Impcat Behavior of plain concrete loaded in uniaxial compression. *Journal od Engineering Mechanics*, 685-693.

Consolazio, G. R., Cook, R. A., & Lehr, G. B. (2002). *Barge impact testing of the St. George Island causeway bridge; Phase I: Feasibility study.* Gainsville, FL: University of Florida.

Consolazio, G. R., Cook, R. A., & McVay, M. C. (2006). *Barge impact testing of the St. George Island causeway bridge; Phase III: Physical testing and data interpretation.* Gainsville, FL: University of Florida.

Consolazio, G. R., Cook, R. A., Biggs, A. E., & Cowan, D. R. (2003). *Barge impact testing of the St. George Island causeway bridge; Pase II: Design of instrumantation systems.* Gainsville, FL: University of Florida.

Consolazio, G. R., Davidson, M. T., & Getter, D. J. (2010). Dynamic amplification of pier column internal forces due to barge-bridge collision. *Transportation Research Record 2172; Transportation Research Board*, 11-22.

Consolazio, G. R., McVay, M. C., Davidson, M. T., & Getter, D. J. (2008). Development of improved bridge design provisions for barge impact loading. *BD545 29; Florida DOT.*

Consolazio, G., & Cowan, D. (2003). Nonlinear analysis of barge crush beahvior and its relationship to impact resistant bridge design. *Computers & Structures, 81,* 547-557.

Crawford, J. E., & et al. (2012). *Use and validation of the release III K&C concrete material model in LS-DYNA.* Glendale, CA: Karagozian & Case. Technical Report TR-11-36.5.

Fan, W., Yuan, W., Yang, Z., & Fan, Q. (2011). Dynamic demand of bridge structure subjected to vessel impact using simplified interaction model. *Journal of Bridge Engineering, 16*(1).

Fujikake, K., Li, B., & Soeun, S. (2009). Impact response of reinfoced concrete beam and its analytical evaluation. *ASCE Journal of Structural Engineering, 135*(8), 938-950.

Haehnel, R. B., & Daly, S. F. (2002). *Maximum impact force of woody debris on floodplain structures.* Technical Report. ERDC/CRREL TR-02-2. US Army Corps of Engineers.

Haehnel, R. B., & Daly, S. F. (2004). Maximum impact force on woody debris on floodplain structures. *ASCE Journal of Hydraulic Engineering, 130*(2), 112-120.

Jaing, H., Wang, X., & He, S. (2012). Numerical simulationof impact tests on reinforced concrete beams. *Materials and Design, 39*, 111-120.

LSTC. (2013). *LS-DYNA. Keyword user's manual. Version R7.0.* Livermore Software Technology Corporation.

Lui, C., & Wang, T.-L. (2001). Statewide vessel collision for bridges. *Journal of Bridge Engineering; ASCE, 6*(3), 213-219.

Luperi, F. J., & Pinto, F. (2013). Determination of impact force history during multicolumn barge flotilla collisions against bridge piers. *ASCE Journal of Bridge Engineering*, 04013011.

Madurapperuma, M., & Wijeyewickrema, A. (2013). Response of reinforced concret columns imacted by tsunami dispersed 20' and 40' shipping containers. *Engineering Structures, 56*, 1631-1644.

Malvar, L. J., & Crawford, J. E. (1998). Dynamic increase factors for concrete. *28th Department of Defense Explosive Safety board Seminar*.

Malvar, L. J., & Crawford, J. E. (1998). Dynamic increase factors for steel reinforcing bars. *28th Department of Defense Explosive Safety Board Seminar*.

Matsutomi, H. (2009). Method for estimating collision force of driftwood accompanying tsunami inundation flow. *Journal of Disaster Research, 4*(6), 435-440.

Meier-Dörnberg, K. E. (1983). Schiffskollisionen, Sicherheitszonen und Lastannahmen für Bauwerke der Binnenwasserstraßen (Ship Collisions, Saftey Zones, and Loading Assumptions for Structures in Inland Waterways). *VDI-Berichte*, *496 in Ge*, 1–9.

Murray, Y. D. (2007). Users manual for LS-DYNA concrete material model 159. *Report No. FHWA-HRT-05-062, Federal Highway Administration*.

Murray, Y. D., Abu-Odeh, A., & Bligh, R. (2007). *Evaluation of LS-DYNA concrete material model 159.* Federal Highway Administration.

Piran Aghl, P., Naito, C. J., & Riggs, H. R. (2014). Full-scale experemental study of impact demands results from high mass, low velocity debris. *ASCE Journal of Structural Engineering*, 04014006.

Riggs, H. R., & et al. (2013). Water-driven debris impact forces on stuctures: Experemental and theoretical program. *Proc., ASME 2013/32nd Int. Conf. on Ocean, Offshore and Artic Engineering, OMAE2013-11128*, ASME.

Sha, Y., & Hao, H. (2012). Nonlinear finite element analysis of barge collision with a singel bridg pier. *Engineering Structures, 41*, 63-76.

Sha, Y., & Hao, H. (2013, January). Laboratory tests and numerical simulations of barge impact on circualr reinforced concrete piers. *Engineering Structures, 46*, 593-605.

Simo, J. C., Ju, J., Pister, K. S., & Taylor, R. L. (1988). Assessment of Cap Model: Consistent Return Algorithms and Rate Dependent Extension. *Journal of Engineering Mechanics, 114*(2), 191–218. doi:10.1061/(ASCE)0733-9399(1988)114:2(191).

Yuan, P., & Harik, I. E. (2008). One-dimensional model for multi-barge flotillas impacting bridge piers. *Computer-Aided Civil and Infrastructure Engineering, 23*, 437-447.

Yuan, P., & Harik, I. E. (2010). Equivalent barge and flotilla impact forces on bridge piers. *ASCE Journal of Bridge Engineering, 15*(5), 523-532.